

**Fully Simultaneous Coupling of the
Full Potential Equation and the
Integral Boundary Layer Equations in
Three Dimensions**

by
Brian Allen Nishida

B.S., University of California at Davis (1987)
M.S., Stanford University (1988)

SUBMITTED TO THE DEPARTMENT OF
AERONAUTICS AND ASTRONAUTICS
IN PARTIAL FULFILLMENT OF THE REQUIREMENTS
FOR THE DEGREE OF

Doctor of Philosophy
at the
Massachusetts Institute of Technology

February 1996

©1996 Massachusetts Institute of Technology
All rights reserved

Signature of Author _____
Department of Aeronautics and Astronautics
September 7, 1995

Certified by _____
Professor Mark Drela
Thesis Supervisor, Department of Aeronautics and Astronautics

Certified by _____
Professor Kenneth S. Breuer
Department of Aeronautics and Astronautics

Certified by _____
Professor Ain A. Sonin
Department of Mechanical Engineering

Accepted by _____
MASSACHUSETTS INSTITUTE
OF TECHNOLOGY
Professor Harold Y. Wachman
Chairman, Department Graduate Committee

FEB 21 1996

ARCHIVES

LIBRARIES

**Fully Simultaneous Coupling of the Full Potential Equation
and the Integral Boundary Layer Equations in
Three Dimensions**

by
Brian Allen Nishida

Submitted to the Department of Aeronautics and Astronautics
on September 7, 1995
in partial fulfillment of the requirements for the degree of
Doctor of Philosophy in Aeronautics and Astronautics

A Fully Simultaneous viscous/inviscid coupling method for three-dimensional flows has been developed. The inviscid outer flow is modeled by the Full Potential equation, the viscous inner flow is modeled by a set of three-dimensional integral boundary layer equations, and viscous/inviscid interaction is achieved using a wall transpiration boundary condition and an edge velocity formula. The viscous and inviscid equations are discretized using finite elements and solved by the Newton method. At each iteration the solution to a large, sparse, linear system is computed with a pre-conditioned Generalized Minimal Residual Method (GMRES). Test cases are presented for several wings. The algorithm performs well for small to moderate three-dimensional effects.

Thesis Supervisor: **Mark Drela,**
Associate Professor of Aeronautics and Astronautics

Acknowledgments

First and foremost, I wish to thank my advisor and friend Prof. Mark Drela who gave me the opportunity to study at MIT. His physical intuition and mathematical dexterity provided me with a world-class aeronautical engineering education.

I would also like to thank the other members of my thesis committee for their recommendations and insightful questions: Prof. Kenneth Breuer and Prof. Ain Sonin. I owe a special thanks to Prof. Jaime Peraire for taking the time to discuss finite element concepts and for being a reader of my thesis. In addition, I would like to thank the other readers of my thesis for their useful suggestions: Prof. Eugene Covert and Dr. J. Douglas McLean. Several other people offered their valuable advice during the course of my research and I thank them: Dave Darmofal, Josh Elliot, Bilal Mughal, Phil Poll, Tom Sorensen, and the TRANAIR group at Boeing. And I wish to thank Steve Ellis and Bob Haimes for keeping me computationally afloat.

Next I wish to thank all of my previous officemates for always being considerate and for diplomatically humoring my ranting and raving: Dave M., Eric, Pam, and Ray. And I thank everyone in CFDL, CASL/SPPL, and Chico's Bail Bonds for their comraderie in and out of the lab. There are too many to name here (≈ 50), and I would surely leave someone out, but you know who you are! I also wish to thank some people outside of the lab for their friendship: Matt, Yildiz, Ashanthi.

Finally, I wish to thank my parents who have selflessly given me everything that I need to live and thrive.

This research was sponsored by the Boeing Airplane Company under the supervision of Dr. Wen-Huei Jou.

Contents

Abstract	3
Acknowledgments	5
List of Figures	12
Nomenclature	14
1 Introduction	16
1.1 Viscous/Inviscid Interaction	16
1.2 Coupling Methods	17
1.3 3-D Boundary Layer Equations	20
1.4 Contents of Thesis	22
2 Full Potential Equation	23
2.1 Definition	23
2.2 Finite Element Discretization	26
2.2.1 Residual Equation	26
2.2.2 Artificial Viscosity	27
2.3 Boundary Conditions	28
2.3.1 Dirichlet Condition	28
2.3.2 Neumann Condition	29
2.3.3 Wake Boundary Conditions	29

2.4	Global Variables	30
2.4.1	α -Specified	30
2.4.2	C_L -Specified	31
2.5	Vacuum Speed Clamp	31
3	Integral Boundary Layer Equations for Three-Dimensional Flows	33
3.1	Definitions	33
3.2	Boundary Layer Domain	34
3.3	Nodal Variables	35
3.3.1	Primary Boundary Layer Variables	36
3.3.2	Edge Velocity Definitions	36
3.4	Finite Element Discretization	37
3.5	Boundary Conditions	40
3.5.1	Attachment Line	40
3.5.2	Transition Line	41
3.5.3	Natural Boundary Conditions	42
3.5.4	A Word on Characteristic Boundary Conditions	42
4	Fully Simultaneous Coupling	46
4.1	Wall Transpiration	46
4.2	Edge Velocity Components	47
4.3	Source/Sink Subgrid Model	48
4.3.1	The Problem	48
4.3.2	A Remedy	51
4.4	Coupling Method	54

5 Solution Process	56
5.1 Newton Method	56
5.2 Assembling the Jacobian system	56
5.2.1 Global Equation Numbers	58
5.2.2 Matrix Mapping	58
5.2.3 Column Format	60
5.2.4 Assembly Process	61
5.3 Linear System Solution	61
5.4 Practical Issues	62
5.4.1 Debugging the Newton Method	63
6 Results	65
6.1 Infinite Swept Wing	65
6.2 RAE 2822 Airfoil	68
6.3 RAE 101 45-degree Swept Wing	69
6.4 MBB-AVA Wing	75
6.5 Boeing 747 Wing	80
6.6 H_k Difficulties	84
6.7 Performance of the Code	85
7 Conclusions	86
7.1 FS Coupling for 3-D Flows	86
7.2 FEM Discretization of the 3-D Integral BL Equations	87
7.3 Newton Method Solution	87
7.4 Recommendations for Future Work	88

7.4.1	Improvements in 3-D Boundary Layer Modeling	88
7.4.2	Examination of Farfield Drag Formula	88
7.4.3	Newton Method Speedup	88
7.4.4	Viscous Design Work	89
Bibliography		90
A Finite Element Method for the Full Potential Equation		95
A.1	FEM Details	95
A.1.1	Isoparametric Trilinear Elements	95
A.1.2	Shape Function Gradients	96
A.1.3	Surface Gradients	97
A.2	Full Potential Equation Sensitivities	99
A.2.1	Velocity Vector	99
A.2.2	Velocity Squared	99
A.2.3	Mach Number	99
A.2.4	Upwinding Factor	100
A.2.5	Density	100
A.2.6	Upwinded Density	100
A.2.7	Full Potential Residual	101
A.2.8	Wake B.C.	102
B Closure for Three-Dimensional Boundary Layer Equations		103
B.1	1-2 Coordinate Definitions	103
B.2	$x-z$ Coordinate Definitions	104
B.3	Crossflow Model	104

B.4	Derived Thicknesses	105
B.5	Empirical Closure Relations	106
C	Wall Transpiration	112
C.1	Real Viscous Flow	113
C.2	Equivalent Inviscid Flow	113
C.3	Wall Transpiration for Drag Calculations	114
C.3.1	3-D Integral Momentum Equations	114
C.3.2	Vector Product Rule and Combining	115
C.3.3	Differencing Coordinate Vectors	115
D	Drag Calculation	117
D.1	Preliminaries	119
D.1.1	Small Perturbation Pressure and Density	119
D.1.2	∇_s , Operator	120
D.1.3	Continuity Result	120
D.2	Integral Momentum Theorem	122
D.3	Farfield Fluxes and Pressure	122
D.4	Surface Fluxes ar Pressure	123
D.5	Interior Momentum Sources	124
D.6	Total Drag	125

List of Figures

1.1	Viscous/Inviscid Domains	17
1.2	Direct Coupling Method	18
1.3	Semi-inverse Coupling Method	19
1.4	Fully Simultaneous Coupling Method	20
2.1	Wing/Body with Wake	25
2.2	Mass Conservation Wake Boundary Condition	30
2.3	Density Function	32
3.1	Physical Boundary Layer Domain	35
3.2	2-D BL coordinate system	37
3.3	BL element weighting function	40
3.4	Leading Edge Region of an Airfoil	41
3.5	External velocity vectors for testing boundary conditions	43
3.6	Contours of H_k for BC type 1	44
3.7	Contours of H_k for BC type 2	44
3.8	Contours of H_k for modified BC type 3	45
4.1	Sawtooth in δ^*	49
4.2	BL sensitivity in separating flow	51
4.3	Source Sink Subgrid Model	52
4.4	Source/Sink Parameters	53

6.1	van den Berg/Elsenaar Experiment	66
6.2	Convergence of θ_{11} for Infinite Swept Wing	66
6.3	Infinite Swept Wing Results	67
6.4	Infinite Swept Wing, Velocity Profiles	68
6.5	Computed C_p and H_k vs. Experiment	70
6.6	Convergence of Drag for RAE 2822	71
6.7	RAE 101 Wing, C_p profiles at experimental span stations	72
6.8	RAE 101 Wing, Upper surface BL quantities at $\eta = 0.50$ and $\eta = 0.80$	73
6.9	RAE 101 45-degree Swept Wing, C_L vs. α and C_L vs. C_D	74
6.10	MBB-AVA Wing, <i>attached case</i> , C_p at experimental span stations	76
6.11	MBB-AVA Wing, <i>separated case</i> , C_p at experimental span stations	77
6.12	C_p distributions at $\eta \approx 0.76$	78
6.13	MBB-AVA wing, separated case, τ_w direction vectors	79
6.14	MBB-AVA Wing, $M_\infty = 0.80$, C_L vs. α and C_L vs. C_D	79
6.15	B-747 Wing, <i>attached case</i> , C_p at experimental span stations	81
6.16	B-747 Wing, <i>separated case</i> , C_p at experimental span stations	82
6.17	B-747 wing, separated case, τ_w direction vectors	83
6.18	B-747 Wing, $M_\infty = 0.838$, C_L vs. α and C_L vs. C'_D	84
A.1	Hexahedral Elements	95
A.2	Construction of 2-D Coordinate System	98
C.1	Equivalent Inviscid Flow Calculation	112
D.1	Velocity Defect in RVF vs. EIF	118
D.2	Control Volume for Integral Momentum Theorem	119

Nomenclature

Roman Symbols

b	wing span
c	local airfoil chord
C_f	skin friction coefficient
C_L	lift coefficient
C_D	drag coefficient
C_M	moment coefficient
c_{mac}	mean aerodynamic chord
C_p	pressure coefficient
C_τ	turbulent shear stress coefficient
D	turbulent dissipation
H	shape parameter
H_k	kinematic shape parameter
K_c	empirical constant for lag equation
M	Mach number
N	FEM shape function
$\mathcal{O}()$	on the order of
p	pressure
q	speed
\vec{q}	velocity vector
Re	freestream Reynold's number
R_i	local residual vector for node i
\mathbf{R}	global residual vector
u, v, w	surface Cartesian velocity components
u_1, u_2	streamwise-crossflow BL edge velocity components
u_e, w_e	$z-z$ BL edge velocity components
U_i	local solution vector for node i
\mathbf{U}	global solution vector
V_w	wall transpiration velocity
W	weighting function
x_{tran}	transition point location

Greek Symbols

α	freestream angle-of-attack
----------	----------------------------

β_w	limiting streamline angle
δ	boundary layer thickness
δ_1^*	streamwise displacement thickness
δ_2^*	crossflow displacement thickness
δ_x^*, δ_z^*	x, z displacement thicknesses
$\delta_x^{**}, \delta_z^{**}$	x, z density thicknesses
η	span station
γ	ratio of specific heats
Γ	circulation
μ	artificial dissipation coefficient
ϕ	perturbation velocity potential
ρ	density
τ_{xw}, τ_{zw}	x, z wall shear stresses
θ_{11}	streamwise momentum thickness
θ_{xz}, θ_{zz}	x -momentum thicknesses
θ_{zx}, θ_{zz}	z -momentum thicknesses
θ_x^*, θ_z^*	x, z kinetic energy thicknesses

Superscripts and Subscripts

$(\)_1$	streamwise boundary layer quantity
$(\)_2$	crossflow boundary layer quantity
$(\)_{bl}$	boundary layer quantity
$(\)_e$	boundary layer edge quantity
$(\)_\infty$	freestream quantity

Acronyms

BC	Boundary Condition
BL	Boundary Layer
FEM	Finite Element Method
FP	Full Potential
FS	Fully Simultaneous
GMRES	Generalized Minimal RESidual Method
LU	Lower-Upper (matrix factorization)
VII	Viscous/Inviscid Interaction

Chapter 1

Introduction

The computation of three-dimensional, viscous, transonic flows is useful for the aerodynamic design of modern aircraft. For these problems, viscous/inviscid interaction (VII) methods are attractive because they can match experimental data as well as Navier-Stokes (N-S) solvers but at a lower cost. N-S solvers require more mesh points in order to resolve thin shear layers, and their convergence is hampered by the resulting fine-mesh time-step limits. On the downside, VII methods are not as general as N-S solvers and many VII methods break down in flows with separation. The lack of generality is due to the simplifications inherent in the models (e.g. an assumed triangular crossflow profile), but this is not an issue if VII methods are restricted to flows for which the approximations are accurate (e.g. wings and wing-bodies). This research addresses the second problem and presents a Fully Simultaneous (FS) coupling method which is numerically stable for flows with separation.

1.1 Viscous/Inviscid Interaction

In 1904 Prandtl introduced the important concept of the boundary layer [1]. For high Re flows, except in a thin boundary layer region, viscous effects are negligible. Then using order of magnitude evaluations of Navier-Stokes terms, the pressure is determined to be nearly constant though the thickness of the boundary layer and only the diffusion in the wall-normal direction is significant. These simplifications are a so-called first-order boundary layer theory yielding approximate, but extremely useful, solutions to the Navier-Stokes equations. These concepts were rigorously re-derived and extended using the method of matched asymptotic expansion [47]. One result of the mathematical analysis is a higher-order BL theory which allows for a finite pressure gradient through the thickness of the

boundary layer.

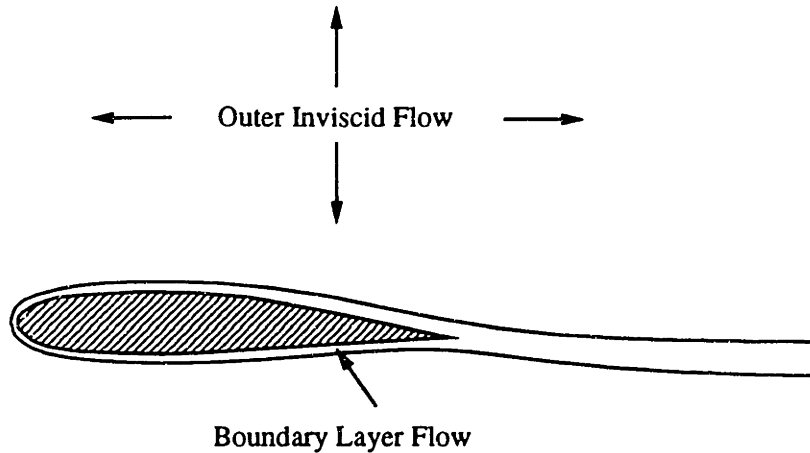


Figure 1.1: Viscous/Inviscid Domains

Using the boundary layer concept, the flowfield may be divided into two regions: an outer inviscid flow where viscous effects are negligible and an inner viscous flow which is approximated by the boundary layer equations. The inviscid flow feels the presence of the boundary layer through a displacement effect and the viscous flow senses the presence of the outer inviscid flow through the pressure field at the boundary layer edge. Both sets of equations must be solved using a coupling method.

1.2 Coupling Methods

Coupling methods include two main components: an inviscid solver and a viscous solver. The inviscid solver usually contains a wall transpiration (V_w) boundary condition to simulate the displacement effect of the boundary layer. A *direct* inviscid solver takes V_w , (or equivalently displacement thickness, δ^*) as its input and outputs edge velocity, q_e . An *inverse* inviscid solver has q_e as its input and V_w as its output. While a *direct* viscous solver uses q_e to compute δ^* , and an *inverse* viscous solver uses δ^* to compute q_e . Coupling methods are combinations of these solvers.

The available coupling methods are: direct, inverse, semi-inverse, quasi-simultaneous, and fully simultaneous. An excellent overview of these methods is given by Lock and Williams [34]. All of these have been used in 2-D with varying amounts of success—FS coupling being the most robust. For 3-D flows, the most popular coupling algorithms have been the direct and semi-inverse methods.

The direct method has been employed by Firmin [19], Lazareff [31], and McLean [35], and works well for attached flows. The method is a direct inviscid solver coupled to a direct viscous solver in an iteration loop. The iteration process continues until the inviscid

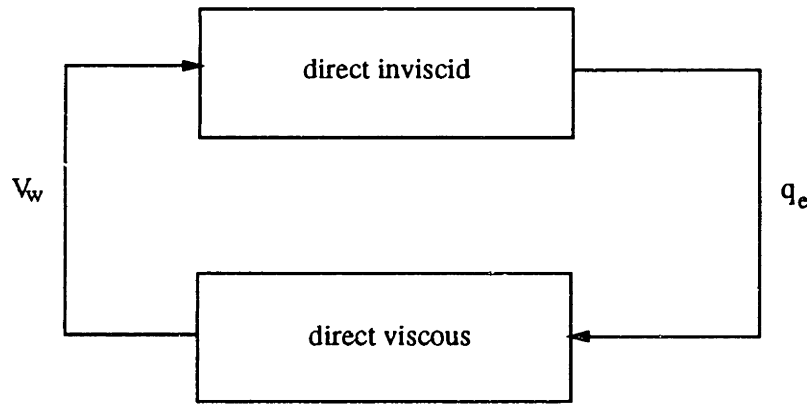


Figure 1.2: Direct Coupling Method

equations and the viscous equations are converged. A stability analysis demonstrates that this coupling scheme is unstable in 2-D separations where skin friction, C_f , approaches zero as analyzed by Wigton and Holt [64]; and an argument based on the theory of characteristics reveals that the direct viscous solvers are ill-posed in swept wing separations when the wall shear stress vector becomes perpendicular to the marching direction. The modified direct method of Yoshihara and Wai [65] uses the direct boundary layer equations cast in characteristic form to avoid an ill-posed marching direction and this allows the algorithm to compute mildly separated flows.

The semi-inverse method has been used by Cebeci [9], Kovalev [30], and Le Balleur [32]. Here, a direct inviscid solver is coupled with an inverse viscous solver. In one semi-inverse

form, a direct inviscid solver yields one calculation of edge velocity and an inverse viscous solver produces another calculation of edge velocity. The difference in edge velocities is used in an empirical formula to correct the specified δ^* . The iteration process continues

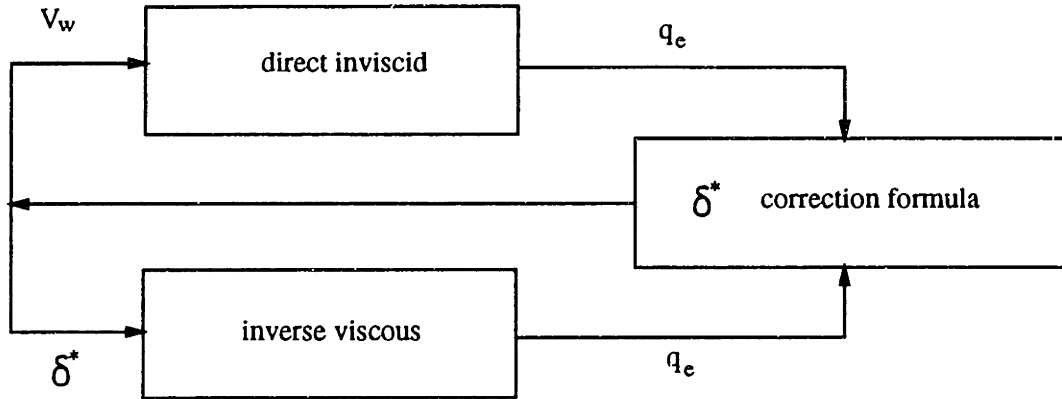


Figure 1.3: Semi-inverse Coupling Method

until the edge velocities computed from the inviscid equations match those from the viscous equations. In theory this method should work for any separated flow [34], but in practice the method breaks down in moderate separation regions [65]. It should be noted that the semi-inverse boundary layer formulation of Le Balleur was able to handle quite severe separations in two dimensions [32] but the same capability has not been demonstrated in three dimensions.

The direct, inverse, and semi-inverse methods use viscous and inviscid equation solvers which require V_w and q_e as fixed inputs. In addition, the viscous and inviscid equations are solved separately in a sequence. In contrast, the Fully Simultaneous coupling method solves both the viscous and inviscid equations simultaneously, and both V_w and q_e are allowed to float within the equations. The motivation is that viscous and inviscid equations together form a well-posed set of equations in attached and separated flows so that their simultaneous solution should be well-posed (and stable) for all flows.

The 2-D FS coupling method of Drela [15] is able to compute flows with large separations in 1-2 minutes on a workstation. The simultaneous solution of the 2-D Euler equations and

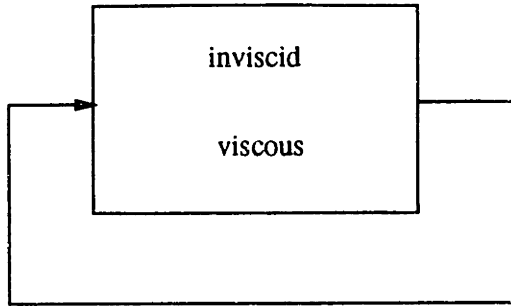


Figure 1.4: Fully Simultaneous Coupling Method

the integral BL equations is computed by the Newton method using an efficient banded matrix solver. However in 3-D, the Newton method matrices are too large to apply a banded solver and iterative techniques must be used. The solution of these linear systems pushes the limits of speed and memory on current workstations.

FS coupling has also been applied to a 3-D Full Potential solver with 2-D boundary layer strips by the TRANSAIR group at Boeing [8]. Their research addressed the solution to large, sparse, non-symmetric matrix systems [66]. However, the three-dimensional integral boundary layer equations are more complicated than their two-dimensional counterparts. Issues such as side boundary conditions, crossflow profiles, and transverse shear stresses now appear.

1.3 3-D Boundary Layer Equations

VII methods can employ either differential or integral boundary layer equations. Although less general, the integral boundary layer equations permit the tracking of key integral thicknesses and shape parameters. In addition, the integral boundary layer equations are much quicker to solve than the differential equations because far fewer unknowns are present. Hence, the integral boundary layer equations are solved in this research.

Systems of 3-D integral BL equations in non-orthogonal coordinates have been derived

by Myring [39], and discretized by Smith [49], and Swafford and Whitfield [54]. Their formulations, which are typical of most schemes, contain surface metric terms which fulfill two purposes. The first type of metric takes into account the skewing and stretching of the surface mesh. For a flat sheet BL domain with a distorted mesh, these are the only metric terms that exist. The second type of metric takes into account the curving of the BL surface when the differential boundary layer equations are integrated in the normal direction. For a rectangular grid wrapped around a circular cylinder, these are the metrics that remain. These metrics are undesirable not only because they complicate the equations, (which complicates debugging and solution interpretation) but also because they require smooth finite-difference grids which bring a certain rigidity to the algorithm.

Most BL formulations, including the current one, neglect the second type of metric term and solve the three-dimensional boundary layer equations over an equivalent flat domain: this is known as first-order BL theory. The approximation is valid when $\delta \ll R$ where δ is a measure of the BL thickness, and R is a local streamwise radius of curvature [40]. If one starts out with a flat domain, the integral boundary layer equations may be derived in a Cartesian coordinate system which eliminates these metrics altogether [38].

The equations are derived on a flat domain, but may be applied to a curved surface provided that the two-dimensional derivatives $\frac{\partial}{\partial x}$ and $\frac{\partial}{\partial z}$ can be locally computed on a curved surface. The finite volume discretization of Mughal [38] uses Green's theorem in an integration of the Cartesian BL equations which eliminates the need for computing the derivatives. An alternative is to assume a local $x-z$ coordinate system and compute derivatives using the Finite Element Method (FEM). This research develops a Petrov-Galerkin Finite Element Method for the discretization of the 3-D integral boundary layer equations. The FEM has the added benefits of: unstructured surface meshes, natural boundary conditions, and inherent crossflow stability.

1.4 Contents of Thesis

This thesis presents an algorithm for Fully Simultaneous coupling in three-dimensions. The finite element discretizations of the Full Potential equation and the 3-D integral boundary layer equations are described in Chapters 2 and 3. Viscous/inviscid interaction procedures are discussed in Chapter 4. The Newton method solution is presented in Chapter 5. Finally, results and conclusions are given in Chapters 6 and 7.

Chapter 2

Full Potential Equation

2.1 Definition

The Full Potential equation is the continuity equation

$$\nabla \cdot (\rho \vec{q}) = 0 \quad (2.1)$$

restricted to irrotational and isentropic flow. The irrotational flow assumption leads to a definition for the velocity, \vec{q} :

$$\vec{q} = \vec{q}_\infty + \nabla \phi \quad (2.2)$$

Using the isentropic assumption the density, ρ , and pressure, p may be derived from the energy equation:

$$\rho = \rho_\infty \left[1 + \frac{\gamma - 1}{2} M_\infty^2 \left(1 - \frac{q^2}{q_\infty^2} \right) \right]^{\frac{1}{\gamma-1}} \quad (2.3)$$

$$p = p_\infty \left[1 + \frac{\gamma - 1}{2} M_\infty^2 \left(1 - \frac{q^2}{q_\infty^2} \right) \right]^{\frac{\gamma}{\gamma-1}} \quad (2.4)$$

where \vec{q}_∞ and ϕ are the freestream velocity and perturbation velocity potential, and ρ_∞ , M_∞ , and γ are the freestream density, Mach number, and ratio of specific heats. Equations 2.1, 2.2, and 2.3 form a nonlinear partial differential equation for ϕ which must be solved numerically.

Equations 2.1, 2.3, and 2.4 are the continuity and conservation of energy equations. The momentum equations are then automatically satisfied with the irrotationality condition (for

incompressible flow, see [36]). To prove this, the momentum equations may be expressed as:

$$\rho \vec{q} \cdot \nabla u_i = -\frac{\partial p}{\partial x_i} \quad i = 1, 2, 3 \quad (2.5)$$

where $i = 1, 2, 3$ refers to the 3-D Cartesian components. Using the definition of velocity in the left-hand-side.

$$\begin{aligned} \rho \vec{q} \cdot \nabla u_i &= \rho (\vec{q}_\infty + \nabla \phi) \cdot \nabla \left[(q_\infty)_i + \frac{\partial \phi}{\partial x_i} \right] \\ &= \rho \vec{q}_\infty \cdot \frac{\partial}{\partial x_i} (\nabla \phi) + \rho \nabla \phi \cdot \frac{\partial}{\partial x_i} (\nabla \phi) \\ &= \rho \frac{\partial}{\partial x_i} (\vec{q}_\infty \cdot \nabla \phi) + \frac{1}{2} \rho \frac{\partial}{\partial x_i} (\nabla \phi \cdot \nabla \phi) \end{aligned}$$

Next using the formulae for pressure, density, and velocity in the right-hand-side.

$$\begin{aligned} \frac{\partial p}{\partial x_i} &= p_\infty \frac{\gamma}{\gamma - 1} \left[1 + \frac{\gamma - 1}{2} M_\infty^2 \left(1 - \frac{q^2}{q_\infty^2} \right) \right]^{\frac{1}{\gamma-1}-1} \left(-\frac{\gamma - 1}{2} M_\infty^2 \frac{1}{q_\infty^2} \frac{\partial q^2}{\partial x_i} \right) \\ &= -\frac{1}{2} \rho_\infty \left[1 + \frac{\gamma - 1}{2} M_\infty^2 \left(1 - \frac{q^2}{q_\infty^2} \right) \right]^{\frac{1}{\gamma-1}} \frac{\partial}{\partial x_i} (\vec{q}_\infty \cdot \vec{q}_\infty + 2 \vec{q}_\infty \cdot \nabla \phi + \nabla \phi \cdot \nabla \phi) \\ &= -\rho \frac{\partial}{\partial x_i} (\vec{q}_\infty \cdot \nabla \phi) - \frac{1}{2} \rho \frac{\partial}{\partial x_i} (\nabla \phi \cdot \nabla \phi) \end{aligned}$$

Since the left-hand-side and right-hand-side of equation 2.5 match for any i , the momentum equations are satisfied. Hence, the continuity equation is sufficient to satisfy the Euler equations (inviscid flow mass, momentum, and energy) restricted to irrotational, isentropic flows.

In flows with strong shocks the isentropic assumption of the Full Potential equation is violated and non-unique solutions may appear [46, 45]. But for weak or moderate shocks the Full Potential equation yields solutions in close agreement with the Euler equations, while at a much lower computational expense. And for many three-dimensional wing-body configurations the shocks are weak, and the addition of viscous effects further weakens the

shocks through displacement body effects. Hence, the Full Potential equation is selected as the inviscid flow model over the Euler Equations.

All lifting surfaces in the domain have a trailing vortex sheet which allows for a jump in potential ($\Delta\phi$). This vortex sheet models the actual wing's wake of concentrated vorticity caused by the pressure differential between the upper and lower surfaces [3]. The wake is unstable and rolls up, but in practice the vortex sheet is represented by a flat, non-moving surface to avoid computing the complicated deformation of the wake. A typical domain for the Full Potential equation is illustrated in Figure 2.1.

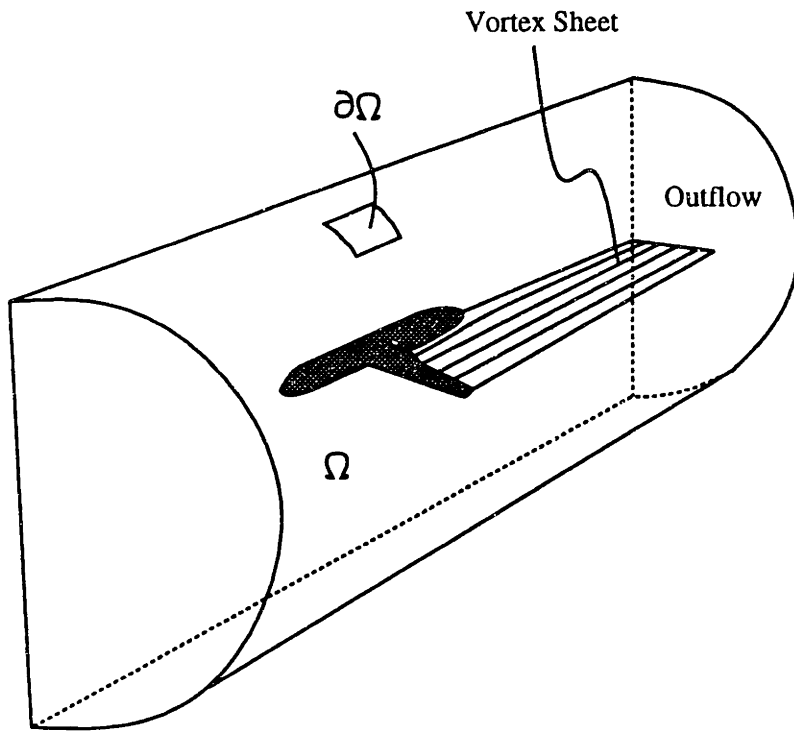


Figure 2.1: Wing/Body with Wake

The boundary conditions of the Full Potential equation are:

1. The velocity potential in the farfield (except at the outflow) is set zero (Dirichlet BC):

$$\phi_{ff} = 0 \quad (2.6)$$

2. The flux through the outflow is set equal to the freestream flux (Neumann BC). This condition allows a jump in ϕ at the outflow on the wake.

$$\vec{q} \cdot \hat{n}|_{outflow} = \vec{q}_\infty \cdot \hat{n}_{outflow} \quad (2.7)$$

3. At any location on the vortex sheet there are two values for ϕ , so two conditions must be imposed. First, the mass flux through the wake is continuous and second, the pressures on the upper and lower wake must match (or the speeds on the upper and lower wake must be equal).

$$\begin{aligned} \rho \vec{q} \cdot \hat{n}|_{upperwake} &= \rho \vec{q} \cdot \hat{n}|_{lowerwake} \\ q_{upper}^2 &= q_{lower}^2 \end{aligned} \quad (2.8)$$

2.2 Finite Element Discretization

The weak form of the Full Potential equation is discretized by the Galerkin Finite Element Method (FEM) [42, 22, 14]. Because this discretization scheme is well known, only the residual equations will be documented in this chapter and the details of the FEM are relegated to Appendix A. The weighted residual form of equation 2.1 is:

$$\iiint_{\Omega} W \{ \nabla \cdot (\rho \vec{q}) \} dV = 0 \quad (2.9)$$

where W is a weighting function and Ω is the volume of the domain. The weak form is derived by integrating 2.9 by parts and applying the Divergence Theorem:

$$\iiint_{\Omega} \nabla W \cdot (\rho \vec{q}) dV - \iint_{\partial\Omega} W (\rho \vec{q}) \cdot \hat{n} dS = 0 \quad (2.10)$$

where $\partial\Omega$ is the surface of the domain with \hat{n} being the unit normal outwards.

2.2.1 Residual Equation

For the discrete form, the flowfield is partitioned into 8-node hexahedral elements, and elements with collapsed edges and faces may be present in the domain. Within each element, the $\phi^e(x, y, z)$ field is represented by

$$\phi^e = \sum_{j=1}^8 N_j^e \phi_j^e$$

where N^e is a trilinear shape function. N^e is also used as the weighting function (i.e. the Galerkin method), and it is given in Appendix A. When ϕ^e is substituted into equation 2.10, discrete equations in terms of the nodal ϕ_j^e values result. For example, at node i , the residual contribution from element e is:

$$\begin{aligned} R_i^e &= \iiint_{V^e} \nabla N_i^e \cdot (\rho^e \vec{q}^e) dV - \iint_{S_{\partial\Omega}^e} N_i^e (\rho^e \vec{q}^e) \cdot \hat{n} dS \\ \vec{q}^e &= \vec{q}_\infty + \sum_{j=1}^8 \nabla N_j^e \phi_j^e \\ \rho^e &= \rho_\infty \left[1 + \frac{\gamma-1}{2} M_\infty^2 \left(1 - \frac{q^{e2}}{q_\infty^2} \right) \right]^{\frac{1}{\gamma-1}} \end{aligned} \quad (2.11)$$

V^e is the volume of the element, and if any of the elemental faces forms part of the domain boundary ($\partial\Omega$) then the $S_{\partial\Omega}^e$ integral makes a contribution to the residual, otherwise the surface integral is zero. These volume and surface integrals are evaluated using $2 \times 2 \times 2$ and 2×2 gauss quadrature [6]. Unless otherwise stated, all residual equations such as Equation 2.11 are *elemental* residual equations and the superscript e will now be dropped for convenience.

The ϕ field which satisfies the non-linear residual equations is computed with the standard Newton Method algorithm (see Chapter 5). The required Jacobian matrix sensitivities for the inviscid equations are also listed in Appendix A.

2.2.2 Artificial Viscosity

Some form of artificial viscosity must be added in supersonic flow regions to capture shocks and to keep the Jacobian matrix non-singular. This research employs the artificial com-

pressibility method [23]: which upwinds the density.

$$\begin{aligned}\tilde{\rho} &= \rho - \mu \left(\frac{\partial \rho}{\partial s} \right) \Delta s \\ &\approx \rho - \mu (\rho - \rho_{up})\end{aligned}\tag{2.12}$$

where ρ_{up} is the density in the element upstream of the current element and μ is defined below.

$$\begin{aligned}\mu &= \mu_c \max(0, \mu, \mu_{up}) \\ \mu &= 1 - \frac{M_{crit}^2}{M^2}\end{aligned}\tag{2.13}$$

Here μ_c is a specified upwinding factor $\sim \mathcal{O}(1)$; M is the local Mach number; and M_{crit} is a user-defined critical Mach number $\sim \mathcal{O}(0.98)$. An upstream element must be specified for every element of a given mesh and it turns out that the nearest element in the upstream x -direction is a good approximation to the streamline upstream element [42]. $\tilde{\rho}$ then replaces the ρ in equation 2.11.

2.3 Boundary Conditions

The algorithm described above is not complete without the boundary conditions. After the entire Jacobian matrix is assembled (see Chapter 5), boundary conditions are applied by modifying the matrix.

2.3.1 Dirichlet Condition

Dirichlet conditions are enforced by adding a large number, $B \sim \mathcal{O}(10^{10})$, to the diagonal of the Jacobian matrix corresponding to Dirichlet ϕ , and $B \cdot const$ is added to the residual vector. After scaling the rows of the Jacobian matrix, the new equation for this ϕ becomes:

$$\phi_i = const\tag{2.14}$$

2.3.2 Neumann Condition

Neumann conditions are enforced by specifying a flux at a face (see equation 2.10). At the outflow, the flux integral is represented by:

$$\iint_{\partial\Omega_{out}} N(\rho \vec{q})_\infty \cdot \hat{n} dS \quad (2.15)$$

This term is added to the residual on outflow elements, and the corresponding sensitivities are added to the Jacobian matrix.

2.3.3 Wake Boundary Conditions

The first boundary condition requires that the flux into the upper element must equal the flux out of the lower element. Using equation 2.10 a lower wake *surface* integral may be expressed in terms of an upper wake *volume* integral:

$$\begin{aligned} -\iint_{\partial\Omega_{lower}} N(\rho \vec{q}) \cdot \hat{n} dS &= \iint_{\partial\Omega_{upper}} N(\rho \vec{q}) \cdot \hat{n} dS \\ &= \iiint_{\Omega_{upper}} \nabla N \cdot (\rho \vec{q}) dV \end{aligned} \quad (2.16)$$

where Ω_{upper} is a volume of fluid on the upper wake. Hence the discrete form of a lower wake node becomes:

$$(R_{lower})_i = \iiint_{V_{lower}} \nabla N_i \cdot (\rho \vec{q}) dV + \iiint_{V_{upper}} \nabla N_i \cdot (\rho \vec{q}) dV \quad (2.17)$$

After the Jacobian matrix has been assembled, the matrix row corresponding to an upper wake node is added to the matrix row of a lower wake node, and the upper node equation is subsequently zeroed out. The replacement upper node equation is a weighted residual speed-matching equation.

$$(R_{upper})_i = \iint_{S_{upper}} W_i (q_{upper}^2 - q_{lower}^2) dS \quad (2.18)$$

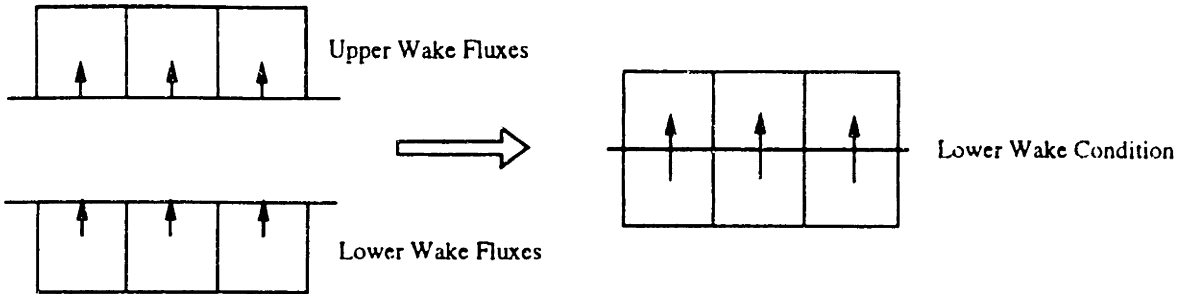


Figure 2.2: Mass Conservation Wake Boundary Condition

To prevent odd-even oscillations in q on the wake, an upwinded weighting function is employed.

$$W_i = N_i + \frac{1}{2} \vec{\Delta} \cdot \nabla N_i$$

$$\vec{\Delta} = \Delta x \hat{i} + \Delta z \hat{k}$$
(2.19)

Δx and Δz are typical length scales for the two-dimensional surface element. This is a Petrov-Galerkin formulation [27], and it removes wiggles while maintaining $h^{\frac{3}{2}}$ accuracy (h is the mesh size).

2.4 Global Variables

A global equation is added to the Newton system (see equation 5.1) to allow the option of lift specified, $C_{L,spec}$, or angle-of-attack specified, α_{spec} . The extra degree of freedom in both cases is freestream angle-of-attack, α , which influences all of the inviscid residual equations through the \vec{q}_∞ -term in Equation 2.11.

2.4.1 α -Specified

The equation for user specified angle-of-attack is simply:

$$R_\alpha = \alpha - \alpha_{spec} \quad (2.20)$$

2.4.2 C_L -Specified

The equation for user specified lift is

$$\begin{aligned} R_\alpha &= C_L - C_{L,spec} \\ C_L &= \frac{1}{\frac{1}{2}\rho_\infty q_\infty^2 S_{ref}} \left\{ \frac{1}{2} \rho_\infty q_\infty \int_b (\phi_{upper} - \phi_{lower}) dl \right\} \end{aligned} \quad (2.21)$$

where the lift is computed from a Trefftz plane integration and b is the span of the vortex sheet. This is valid for compressible, irrotational, isentropic flows [4].

2.5 Vacuum Speed Clamp

Under some compressible conditions, regions exist where the density reaches zero when the flow speed approaches the vacuum speed, q_{vac} .

$$q_{vac}^2 = q_\infty^2 \left(1 + \frac{2}{(\gamma - 1) M_\infty^2} \right) \quad (2.22)$$

This might occur at a wingtip trailing edge where the velocity should theoretically be infinite. Under these conditions, numerical difficulties arise and the density definition must be modified.

To compute in the presence of this singularity, a modified density function is generated. First, the maximum speed for true density calculations (Eqn. 2.3) is determined by setting a maximum local Mach number squared $\sim \mathcal{O}(3.0)$ and computing the corresponding speed from the formula for Mach number (see Appendix A):

$$M_{max}^2 = M_\infty^2 \frac{q^2}{q_\infty^2} \left[1 + \frac{\gamma - 1}{2} M_\infty^2 \left(1 - \frac{q^2}{q_\infty^2} \right) \right]^{-1} \Rightarrow q^2 = q_{max}^2$$

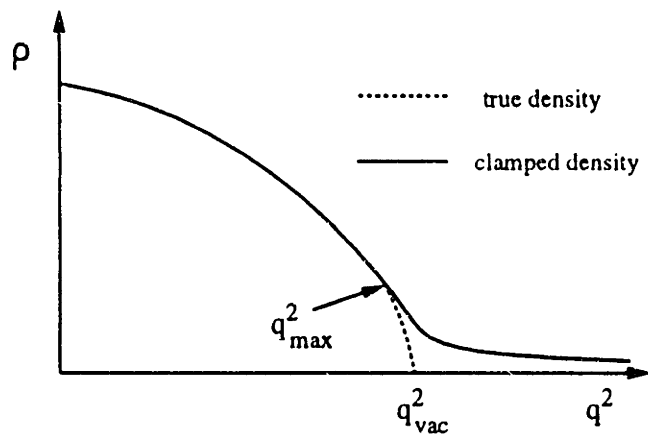


Figure 2.3: Density Function

Then, when the speed squared exceeds q_{max}^2 , the density function is switched over to a modified density that asymptotes with q^2 to prevent zero density. This formulation was constructed by Sorensen [51].

Chapter 3

Integral Boundary Layer Equations for Three-Dimensional Flows

3.1 Definitions

The three-dimensional integral boundary layer equations derived using a Cartesian coordinate system are:

$$\frac{\delta}{C_r} \frac{\partial C_r}{\partial \xi} = K_c (C_{r,eq}^{1/2} - C_r^{1/2}) \quad (3.1)$$

$$\frac{\partial}{\partial x} (\rho_e q_e^3 \theta_x^*) + \frac{\partial}{\partial z} (\rho_e q_e^3 \theta_z^*) + \rho_e q_e^2 \delta_x^{**} \frac{\partial u_e}{\partial x} + \rho_e q_e^2 \delta_z^{**} \frac{\partial w_e}{\partial z} = 2D \quad (3.2)$$

$$\frac{\partial}{\partial x} (\rho_e q_e^2 \theta_{xz}) + \frac{\partial}{\partial z} (\rho_e q_e^2 \theta_{zz}) + \rho_e q_e \delta_x^* \frac{\partial u_e}{\partial x} + \rho_e q_e \delta_z^* \frac{\partial u_e}{\partial z} = \tau_{zw} \quad (3.3)$$

$$\frac{\partial}{\partial x} (\rho_e q_e^2 \theta_{zx}) + \frac{\partial}{\partial z} (\rho_e q_e^2 \theta_{zz}) + \rho_e q_e \delta_z^* \frac{\partial w_e}{\partial z} + \rho_e q_e \delta_x^* \frac{\partial w_e}{\partial z} = \tau_{zw} \quad (3.4)$$

Equation 3.1 is the two-dimensional turbulent shear stress lag equation, 3.2 is the kinetic energy equation, and 3.3 and 3.4 are the x and z momentum equations. The origin of equation 3.1 is given in reference [21] and the derivation of equations 3.2-3.4 may be found in [38]. K_c is an empirical constant set to 5.6. ξ is the lag direction which is taken to be the chordwise direction, and the $x-z$ coordinate system is an arbitrary, local, 2-D surface coordinate system in a plane tangent to the 3-D BL surface. The main assumptions in these equations are that pressure is constant in the normal direction through the thickness of the boundary layer, and that only diffusion normal to the wall is significant.

In Equations 3.1 to 3.4, δ^* 's denote displacement thicknesses, θ 's signify momentum thicknesses, θ^* 's represent energy thicknesses, and δ^{**} 's are density thicknesses. In addition, $C_\tau^{1/2}$ is the shear stress coefficient, $C_{\tau_{eq}}^{1/2}$ is the equilibrium shear stress coefficient, τ 's are wall shear stresses, and D is the turbulent dissipation function. Section §B.1 provides the definitions of the thicknesses for a streamwise-crossflow coordinate system (called the 1-2 coordinate system).

These integral boundary layer equations have a physical interpretation. Equation 3.2 may be thought of as a divergence of kinetic energy deficit (the $\rho_e q_e^3 \theta_z^*$ and $\rho_e q_e^3 \theta_z^*$ terms) balanced by mechanical work deficit ($\rho_e q_e^2 \delta_z^{**} \frac{\partial u_x}{\partial z}$, $\rho_e q_e^2 \delta_z^{**} \frac{\partial w_x}{\partial z}$) and dissipation (D). The mechanical work terms are the products of pressure forces and densities; the pressures may be recognized using Euler's Relation $dp = -\rho q dq$; and the densities may be seen by the definitions of $q_e \delta_x^{**}$, $q_e \delta_z^{**}$. Equation 3.3 contains the x -momentum deficit due to fluxes in the x -direction ($\rho_e q_e^2 \theta_{xx}$) and x -momentum deficit due to fluxes in the z -direction ($\rho_e q_e^2 \theta_{xz}$) balanced by pressure gradient term ($\rho_e q_e \delta_x^* \frac{\partial u_x}{\partial z} + \rho_e q_e \delta_z^* \frac{\partial u_x}{\partial z}$) and wall shear stresses (τ_{zw}). The pressure gradient term is seen once again using Euler's Relation. Equation 3.4 is a similar expression for z -momentum deficit.

3.2 Boundary Layer Domain

The three-dimensional boundary layer equations are a set of hyperbolic partial differential equations [59, 11]. Consequently, these equations require an initial or starting solution, and boundary conditions which depend on the mathematical characteristics entering or leaving the domain. A typical boundary layer domain is depicted in Figure 3.2. The starting solution for Equations 3.2 to 3.4 is specified at the attachment line near the wing leading edge, and the starting solution for Equation 3.1 is specified at the transition line. Boundary conditions are applied along the symmetry line, and the wingtip and waketip boundaries.

The main purpose of this research is to implement Fully Simultaneous coupling in three dimensions which is a difficult problem in itself. Therefore more complicated issues such as corner flows (at wing/body junctures) and three-dimensional free transition will not be

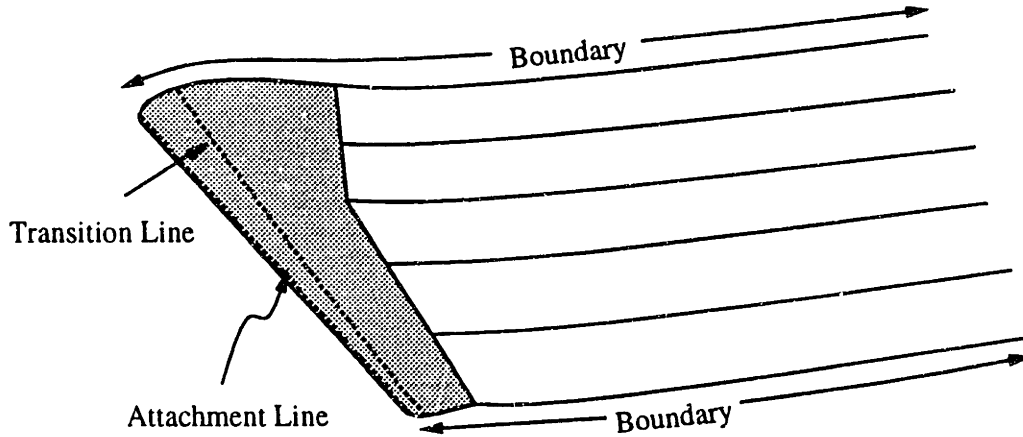


Figure 3.1: Physical Boundary Layer Domain

addressed and initial and boundary conditions are treated in a simple and approximate manner.

3.3 Nodal Variables

Nodal boundary layer variables for the Newton method must be selected from the many $x-z$ variables introduced. In Equations 3.1 to 3.4, the boundary layer variables depend upon an arbitrary, local $x-z$ coordinate system. These $x-z$ variables are not appropriate for nodal variables, because there is no unique $x-z$ coordinate system for a node. Actually, the $x-z$ coordinate system is associated with a given surface element, not a node.

Unknowns in the 1-2 (streamwise-crossflow) coordinate system have unique definitions at any point independent of the $x-z$ coordinate system. Hence, 1-2 variables may be used for the nodal BL unknowns. The $x-z$ quantities in the boundary layer equations are derived from the 1-2 quantities through vector rotation identities. These relations are listed in §B.2 and some of these are derived in reference [49].

3.3.1 Primary Boundary Layer Variables

There are many 1-2 variables, but only four boundary layer equations. Thus only four 1-2 variables may be independent and these are deemed the *primary* BL variables. $C_\tau^{1/2}$, θ_{11} , δ_1^* , and δ_2^* are selected as independent: $C_\tau^{1/2}$ is the square root of the shear stress coefficient, θ_{11} and δ_1^* are the streamwise momentum and displacement thicknesses, and δ_2^* is the crossflow displacement thickness. All other 1-2 boundary layer quantities are computed in terms of these four variables by using two-dimensional closure relations in the streamwise direction and the Johnston triangular crossflow profile [28, 38]. For completeness, these relations are listed in §B.5.

3.3.2 Edge Velocity Definitions

u_e and w_e in the boundary layer equations are the components of velocity in the x - z coordinate system, and because they depend upon orientation of the x - z system they are not suitable for nodal variables. The Cartesian velocity components (u, v, w), on the other hand, are independent of the x - z system. u_e and w_e may easily be expressed in terms of u, v , and w . For example, an x - z coordinate system is defined by:

$$\hat{e}_x = e_{xx}\hat{i} + e_{xy}\hat{j} + e_{xz}\hat{k}$$

$$\hat{e}_z = e_{zx}\hat{i} + e_{zy}\hat{j} + e_{zz}\hat{k}$$

Then u_e and w_e , are computed by dotting the Cartesian velocity, \vec{q} , into \hat{e}_x and \hat{e}_z respectively. i.e.:

$$\begin{aligned} u_e &= \vec{q} \cdot \hat{e}_x = ue_{xx} + ve_{xy} + we_{xz} \\ w_e &= \vec{q} \cdot \hat{e}_z = ue_{zx} + ve_{zy} + we_{zz} \end{aligned} \tag{3.5}$$

This is the projection of the 3-D Cartesian velocity onto the 2-D BL panel.

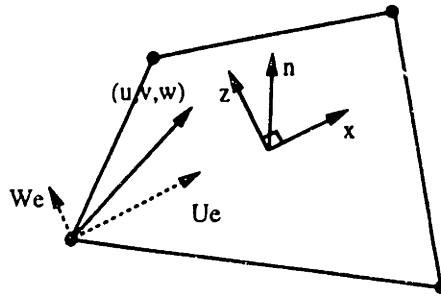


Figure 3.2: 2-D BL coordinate system

The 3-D BL method of Mughal [38] has two nodal velocity components which are rotated through angles on each panel. From past experience, this process is difficult if not impossible over a general surface. Dot products are simple to calculate and can handle any surface that can be paneled. Thus, in spite of the extra velocity component, the Cartesian velocity provides a great simplification to the calculation of edge velocities. The computation of the 3-D Cartesian velocity will be described in Chapter 4.

3.4 Finite Element Discretization

The three-dimensional integral boundary layer equations are discretized with a Petrov-Galerkin Finite Element Method. The Petrov-Galerkin method uses a different weighting function than the shape function, N , in the Galerkin method. The weighted residual forms of equations 3.1-3.4 are:

$$\iint_{\partial\Omega} W \left\{ 2\delta \frac{\partial}{\partial\xi} (\log C_\tau^{1/2}) - K_c (C_\tau^{1/2}_{eq} - C_\tau^{1/2}) \right\} dS = 0 \quad (3.6)$$

$$\begin{aligned} \iint_{\partial\Omega} W \left\{ \frac{\partial}{\partial x} (\rho_e q_e^3 \theta_x^*) + \frac{\partial}{\partial z} (\rho_e q_e^3 \theta_z^*) + \rho_e q_e^2 \delta_x^{**} \frac{\partial u_e}{\partial x} \right. \\ \left. + \rho_e q_e^2 \delta_z^{**} \frac{\partial w_e}{\partial z} - 2D \right\} dS = 0 \end{aligned} \quad (3.7)$$

$$\iint_{\partial\Omega} W \left\{ \frac{\partial}{\partial x} (\rho_e q_e^2 \theta_{xx}) + \frac{\partial}{\partial z} (\rho_e q_e^2 \theta_{xz}) + \rho_e q_e \delta_x^* \frac{\partial u_e}{\partial x} + \rho_e q_e \delta_z^* \frac{\partial u_e}{\partial z} - \tau_{zw} \right\} dS = 0 \quad (3.8)$$

$$\iint_{\partial\Omega} W \left\{ \frac{\partial}{\partial x} (\rho_e q_e^2 \theta_{zx}) + \frac{\partial}{\partial z} (\rho_e q_e^2 \theta_{zz}) + \rho_e q_e \delta_x^* \frac{\partial w_e}{\partial x} + \rho_e q_e \delta_z^* \frac{\partial w_e}{\partial z} - \tau_{zw} \right\} dS = 0 \quad (3.9)$$

Equation 3.6 uses the relation:

$$\frac{1}{C_\tau} \frac{\partial C_\tau}{\partial \xi} = \frac{\partial}{\partial \xi} (\log C_\tau) = 2 \frac{\partial}{\partial \xi} \left(\frac{1}{2} \log C_\tau \right) = 2 \frac{\partial}{\partial \xi} (\log C_\tau^{1/2})$$

The surfaces of a wing and wake are divided into 4-node elements or panels. On each panel a local x - z coordinate system (\hat{e}_x and \hat{e}_z) is set up (see §A.1.3), and at each node x - z BL variables (e.g. $\rho_e q_e^2 \theta_{xx}$, $\rho_e q_e^2 \theta_{xz}$, . . .) are computed using the relations in Appendix B and the independent BL variables ($C_\tau^{1/2}$, θ_{11} , δ_1^* , δ_2^* , u , v , w). Next, standard FEM operations are applied to equations 3.6-3.9 to derive elemental residual equations.

$C_\tau^{1/2}$ Equation

$$\iint_{\partial\Omega} W \left\{ 2 \sum_i N_i(\delta)_i \sum_j \frac{\partial N_j}{\partial \xi} (\log C_\tau^{1/2})_j - K_c \sum_j N_j \left[(C_\tau^{1/2})_{eq} - (C_\tau^{1/2})_j \right] \right\} dS = R_{C_\tau^{1/2}} \quad (3.10)$$

Kinetic Energy Equation

$$\begin{aligned} \iint_{\partial\Omega} W & \left\{ \sum_i \frac{\partial N_i}{\partial x} (\rho_e q_e^3 \theta_x^*)_i + \sum_i \frac{\partial N_i}{\partial z} (\rho_e q_e^3 \theta_z^*)_i \right. \\ & + \sum_i N_i (\rho_e q_e^2 \delta_x^{**})_i \sum_j \frac{\partial N_j}{\partial x} (u_e)_j \\ & \left. + \sum_i N_i (\rho_e q_e^2 \delta_z^{**})_i \sum_j \frac{\partial N_j}{\partial z} (w_e)_j - 2 \sum_i N_i (D)_i \right\} dS = R_{k.e.} \end{aligned} \quad (3.11)$$

X-Momentum Equation

$$\begin{aligned}
& \iint_{\partial\Omega} W \left\{ \sum_i \frac{\partial N_i}{\partial x} (\rho_e q_e^2 \theta_{xx})_i + \sum_i \frac{\partial N_i}{\partial z} (\rho_e q_e^2 \theta_{xz})_i \right. \\
& + \sum_i N_i (\rho_e q_e \delta_x^*)_i \sum_j \frac{\partial N_j}{\partial x} (u_e)_j \\
& \left. + \sum_i N_i (\rho_e q_e \delta_z^*)_i \sum_j \frac{\partial N_j}{\partial z} (u_e)_j - \sum_i N_i (\tau_{xw})_i \right\} dS = R_x
\end{aligned} \tag{3.12}$$

Z-Momentum Equation

$$\begin{aligned}
& \iint_{\partial\Omega} W \left\{ \sum_i \frac{\partial N_i}{\partial x} (\rho_e q_e^2 \theta_{zx})_i + \sum_i \frac{\partial N_i}{\partial z} (\rho_e q_e^2 \theta_{zz})_i \right. \\
& + \sum_i N_i (\rho_e q_e \delta_x^*)_i \sum_j \frac{\partial N_j}{\partial x} (w_e)_j \\
& \left. + \sum_i N_i (\rho_e q_e \delta_z^*)_i \sum_j \frac{\partial N_j}{\partial z} (w_e)_j - \sum_i N_i (\tau_{zw})_i \right\} dS = R_z
\end{aligned} \tag{3.13}$$

where N_i is a 2-D elemental shape functions over the panel, and $(\dots)_i$ are the nodal BL values. These integrals are computed using 2×2 gauss integration.

In equation 3.10, the directional derivative of N in the ξ -direction may be computed from:

$$\frac{\partial N_i}{\partial \xi} = \frac{\partial N_i}{\partial x} (\hat{e}_x \cdot \hat{e}_\xi) + \frac{\partial N_i}{\partial z} (\hat{e}_z \cdot \hat{e}_\xi)$$

The ξ direction is approximated as the chordwise direction.

Because of the hyperbolic nature of the 3-D boundary layer equations, a Galerkin FEM approach ($W = N$) produces an ill-conditioned set of discrete equations [27], and some form of upwinding is required for numerical stability. The 2nd order accurate finite difference scheme of Drela [15] and the 2nd order accurate finite volume scheme of Mughal [38] are essentially box schemes [2] which provide the required upwinding without jeopardizing accuracy. This suggests a finite element scheme using the following elemental weighting functions for upwinding in the ξ -direction:

$$W_1^e = 0 \quad W_2^e = \frac{1}{2}(1 - \eta) \quad W_3^e = \frac{1}{2}(1 + \eta) \quad W_4^e = 0$$

The weighting function over a supercell (shaded) illustrated in Figure 3.3.

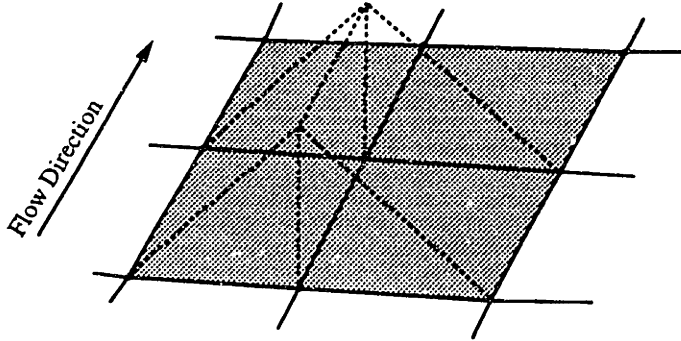


Figure 3.3: BL element weighting function

Thus far, no crosswind dissipation [38] has been required. This scheme is similar to a Crank-Nicholson scheme which is neutrally stable to sawtooth oscillations in the crossflow direction.

3.5 Boundary Conditions

3.5.1 Attachment Line

Nodal boundary layer values at the attachment line are set to the analytic values from (laminar) Falkner-Skan stagnation flow [61].

$$\theta_{11} = 0.29234 \sqrt{\frac{\xi}{Re_\infty u_\xi}}, \quad \delta_1^* = 0.64791 \sqrt{\frac{\xi}{Re_\infty u_\xi}} \quad (3.14)$$

Re_∞ is the freestream Reynolds number, u_ξ is the chordwise velocity component ($u_\xi = \vec{q} \cdot \hat{\xi}$), and ξ is the arc length distance to the attachment point. $C_r^{1/2}$ is zero since this is a laminar flow region, and δ_2^* is set to zero approximating a 2-D flow. This is an adequate

approximation and as mentioned in [38] the solution over the majority of the wing is not sensitive to the initial conditions.

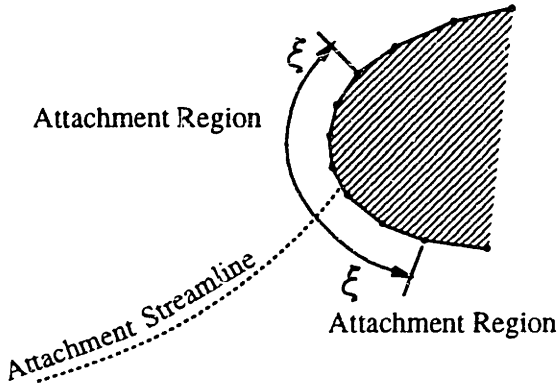


Figure 3.4: Leading Edge Region of an Airfoil

In cases with high Re and large sweep, the attachment line may be turbulent, but this is not treated here. It is examined by Cumpsty and Head [12].

The attachment points are determined by calculating the location of minimum velocity on airfoil sections via linear interpolation. The setup is shown in Figure 3.4. In a straightforward implementation, the two nodes that surround the attachment point are set to stagnation flow conditions. However, this strategy suffered from convergence problems as the attachment point oscillated between two locations. A more robust approach is to set a small group of nodes $\sim \mathcal{O}(3\text{-}6)$ to stagnation flow conditions.

3.5.2 Transition Line

Only fixed transition is simulated in this research. Initial values of $C_\tau^{1/2}$ at the transition line are set by the empirically based formula of Drela for two dimensional flows [16].

$$(C_\tau^{1/2})_{initial} = 1.8 \exp\left(\frac{-3.3}{H - 1}\right) C_\tau^{1/2}_{eq} \quad (3.15)$$

$C_\tau^{1/2}_{eq}$ is computed using the closure relations of Appendix B.

3.5.3 Natural Boundary Conditions

Two natural BC's arise from the FEM discretization of the boundary layer equations. The first is a symmetry condition or $\frac{\partial}{\partial \eta} = 0$ where η is the direction perpendicular to the boundary. This BC results automatically when no flow enters or leaves the domain. If a mirror solution is attached to the domain then the resulting FEM equations for the boundary nodes are merely twice the magnitudes of the equations without the mirror image.

The second natural BC is an infinite-swept-wing-like condition. This BC arises naturally when flow enters or leaves the domain. If an extension of the solution is attached at the boundary, then the boundary node equations will be *approximately* twice the magnitudes of the equations without the extended solution. If this is an infinite swept wing problem, then the boundary node equations will be exactly twice the magnitudes.

3.5.4 A Word on Characteristic Boundary Conditions

The eigensystem decomposition of the 3-D integral BL equations is non-trivial due to the empirical closure formula, and the relations between the x - z and 1-2 coordinate systems. However, using a symbolic manipulation program, Mughal has determined that the eigenvalues of the system are real [37], hence this system of equations is of hyperbolic type. One eigenvalue corresponds roughly to the outer streamline angle, one eigenvalue corresponds to the limiting streamline or wall angle, and the third eigenvalue is an angle between these two.

A methodical way to set the boundary conditions is to use eigensystem information to determine stability for a given BC [20]. This process is difficult for the 3-D BL equations due to the complicated form of the eigenvalues and eigenvectors. As a first cut, the sensitivity of the solution to boundary conditions may be demonstrated by numerical experimentation.

There are several options for boundary conditions: BC type 1 is to set all of the BL variables at the wingtip; BC type 2 is to use natural BC's; and BC type 3 is to set the characteristic variables of the 3-D BL equations corresponding to incoming characteristics.

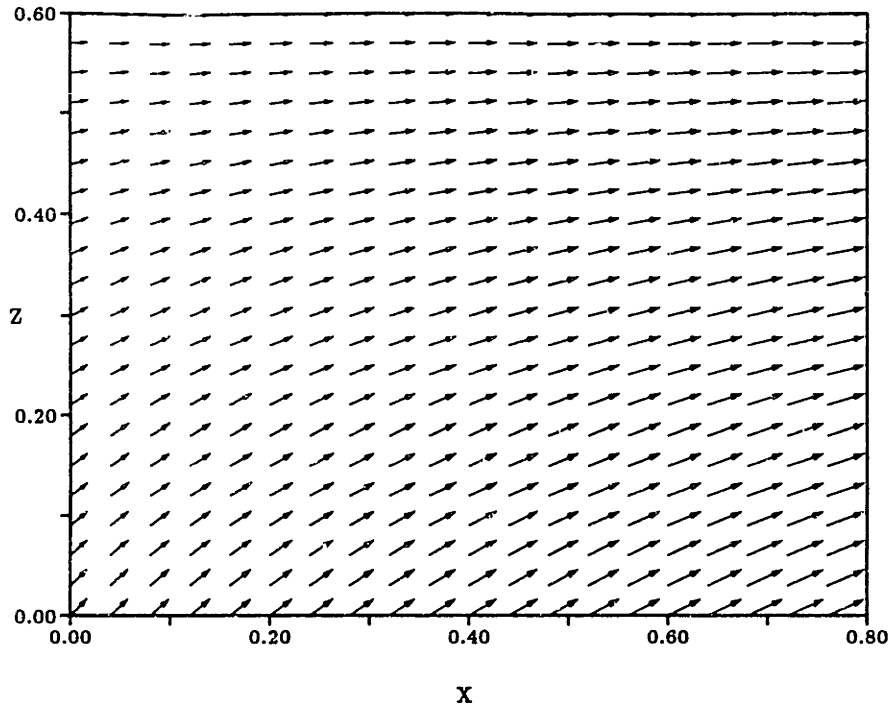


Figure 3.5: External velocity vectors for testing boundary conditions

To illustrate the effects, these BC types were applied to a direct marching, wake calculation. The external flowfield is the irrotational flow near a stagnation point in Figure 3.5 [5, p. 106]. This flow looks similar to that over the trailing wake of a wing.

BC type 1 is the simplest to apply and it is only valid if all of the characteristics of the 3-D BL equations are entering the domain. The results (contours of H_k) are plotted in Figure 3.6. Numerical noise within an envelope of influence appears, indicating that not all of the characteristics are entering the domain. It was later discovered that the pressure gradient points out of the domain which causes the surface shear, $\vec{\tau}_w$ and hence at least one characteristic to point out of the domain. *The hyperbolic equation domain-of-influence also implies a domain-of-error.* When a large separation region is present (starting at a wing/body junction say), an erroneous BC may pollute a sizable portion of the wing.

Several authors have applied BC type 2 in the form of zero-gradient or extrapolation boundary conditions. Strictly speaking this violates the well-posedness of the problem since at least one of the characteristics is entering the domain, but nonetheless, they were able to

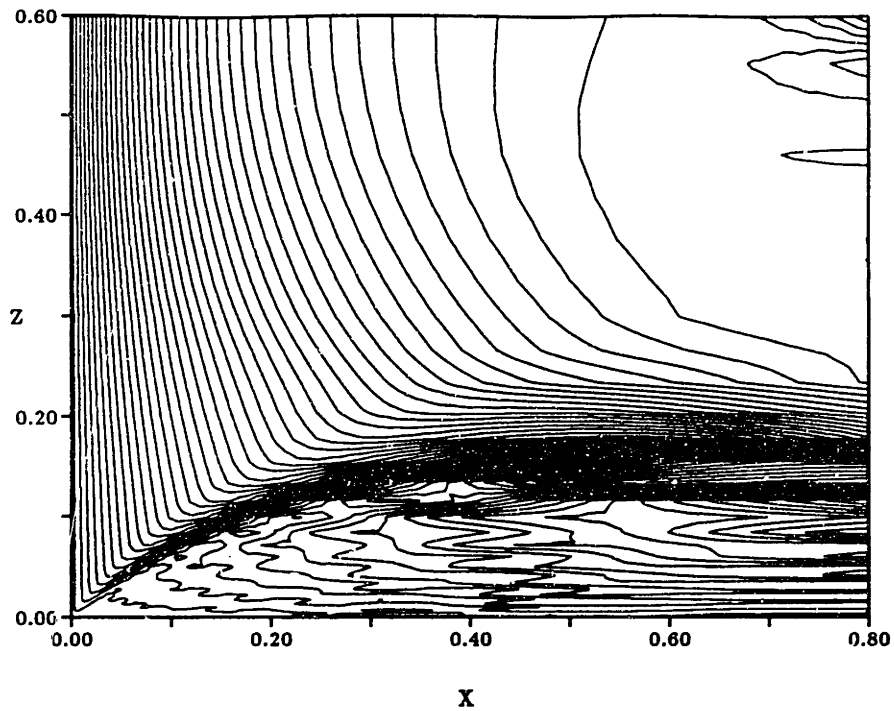


Figure 3.6: Contours of H_k for BC type 1

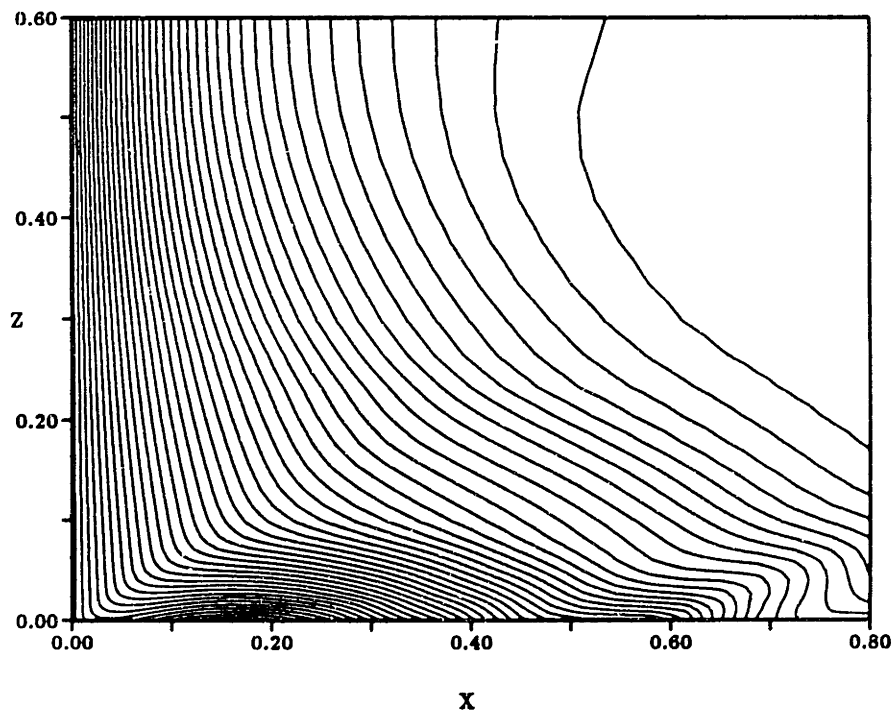


Figure 3.7: Contours of H_k for BC type 2

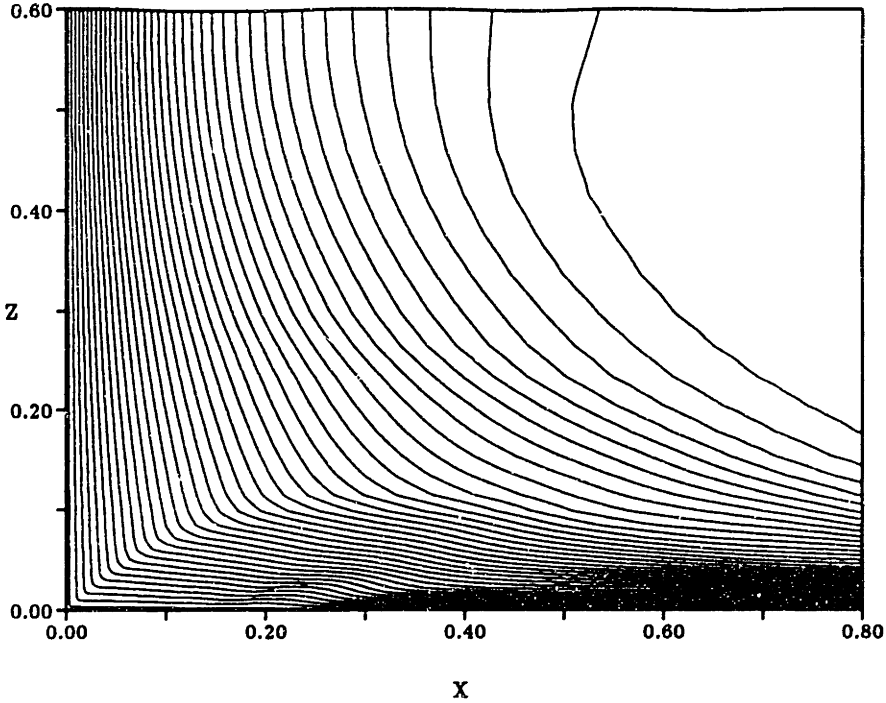


Figure 3.8: Contours of H_k for modified BC type 3

compute solutions [53, 19]. And in Figure 3.7, the results are smoother than those of BC type 1 but there is unusual waviness at $(x, z) = (0.6, 0.0)$ to $(0.8, 0.0)$ which does not look physical.

BC type 3 should be the proper boundary condition, however, it too is difficult to apply. The 3-D BL equations must be cast into characteristic form so that the correct characteristic variables may be set. A modified form of this BC is to assume only one characteristic point out of the domain, and assume that one piece of information must float while the rest of the BL variables must be set. This may or may not work depending upon the results of the eigensystem analysis [20]. Here δ_2^* is allowed to float, while all of the other BL variables are specified. The results are shown in Figure 3.8. It appears to be a reasonable solution to this flowfield, and it is an improvement over BC type 1 and BC type 2.

This study implies that some sort of characteristic information should be incorporated into the boundary conditions. However, determining the characteristic variables is too difficult, and usually can not be constructed from the available data anyway. Hence, in this research, BC type 3 is applied to the suction surface of wings and wakes.

Chapter 4

Fully Simultaneous Coupling

This chapter discusses the link between the inviscid model of chapter 2 and the viscous model of chapter 3 which is known as viscous/inviscid interaction (VII). VII is achieved through a wall transpiration boundary condition and an edge velocities formula. In addition, the Fully Simultaneous (FS) coupling method is described here.

4.1 Wall Transpiration

The displacement effect of the boundary layer on the inviscid outer flow may be simulated by a mass flux on wall and wake surfaces, in both cases called *wall transpiration*. The velocity normal to the wall is matched for the cases of a real, viscous flow and an inviscid flow with wall transpiration at a distance of the boundary layer's edge (see Appendix C). This wall flux is:

$$\rho V_w = \frac{\partial}{\partial x}(\rho_e q_e \delta_x^*) + \frac{\partial}{\partial z}(\rho_e q_e \delta_z^*) \quad (4.1)$$

x and z refer to an arbitrary, local, 2-D surface coordinate system just as in the 3-D boundary layer equations. This wall transpiration formula is applied in the normal velocity condition for the Full Potential equation (equation 2.11):

$$\iint_{\partial\Omega} N_i (\rho \vec{q}) \cdot \hat{n} dS = \iint_{\partial\Omega_{bl}} N_i \left\{ \sum_j \frac{\partial N_j}{\partial x} (\rho_e q_e \delta_x^*)_j + \sum_j \frac{\partial N_j}{\partial z} (\rho_e q_e \delta_z^*)_j \right\} dS \quad (4.2)$$

where $\partial\Omega_{bl}$ are the wall and wake surfaces where the boundary layer is computed. A separate blowing is computed for the upper and lower wakes, and these are combined when

the upper nodal equations are added to the lower nodal equations in the wake boundary condition (see §2.3.3).

4.2 Edge Velocity Components

Viscous/inviscid interaction also requires the edge velocity distribution over the boundary layer. In reference [34], wall curvature effects are taken into account in the edge velocity computations which is known as higher-order boundary layer theory. These corrections are not used here for simplicity, but it is believed that they may be added without affecting the robustness, speed, etc. of the FS coupling procedures.

As discussed in Chapter 3, the edge velocities are computed from the Cartesian velocity components. These velocities are given by:

$$\begin{aligned} u &= \left(u_{\infty} + \frac{\partial \phi}{\partial x} \right)_{bl} \\ v &= \left(v_{\infty} + \frac{\partial \phi}{\partial y} \right)_{bl} \\ w &= \left(w_{\infty} + \frac{\partial \phi}{\partial z} \right)_{bl} \end{aligned} \quad (4.3)$$

Unless otherwise stated (u, v, w) denotes the Cartesian velocity components *on the surfaces* where the boundary layers are computed. And u_e and w_e are the components of these Cartesian edge velocities projected to an arbitrary, 2-D, $x-z$ coordinate system.

These Cartesian velocities are computed with the Galerkin finite element method. The weighted residual equations for the velocity components are:

$$\begin{aligned}
R_u &= \iint_{\partial\Omega_{bl}} N \left\{ u - \left(u_\infty + \frac{\partial\phi}{\partial x} \right)_{bl} \right\} dS \\
R_v &= \iint_{\partial\Omega_{bl}} N \left\{ v - \left(v_\infty + \frac{\partial\phi}{\partial y} \right)_{bl} \right\} dS \\
R_w &= \iint_{\partial\Omega_{bl}} N \left\{ w - \left(w_\infty + \frac{\partial\phi}{\partial z} \right)_{bl} \right\} dS
\end{aligned} \tag{4.4}$$

where N is a 2-D surface shape function and $\partial\Omega_{bl}$ is the boundary layer surfaces. The Galerkin discretization produces the following residuals:

$$\begin{aligned}
(R_u)_i &= \iint_{\partial\Omega_{bl}} N_i \left\{ \sum_j N_j u_j - \left(u_\infty + \sum_j \frac{\partial N_j}{\partial x} \phi_j \right)_{bl} \right\} dS \\
(R_v)_i &= \iint_{\partial\Omega_{bl}} N_i \left\{ \sum_j N_j v_j - \left(v_\infty + \sum_j \frac{\partial N_j}{\partial y} \phi_j \right)_{bl} \right\} dS \\
(R_w)_i &= \iint_{\partial\Omega_{bl}} N_i \left\{ \sum_j N_j w_j - \left(w_\infty + \sum_j \frac{\partial N_j}{\partial z} \phi_j \right)_{bl} \right\} dS
\end{aligned} \tag{4.5}$$

4.3 Source/Sink Subgrid Model

4.3.1 The Problem

The current discretization contains a null space in the viscous/inviscid interaction equations. This can be seen by the example of two dimensional flow over a flat plate with uniform edge velocities. A sawtooth distribution in δ^* produces regions of blowing and suction from $V_w = \frac{\partial}{\partial \xi} (u_e \delta^*)$ and $u_e = \text{constant}$.

These wall transpiration fluxes cancel over a supercell (which consists of two BL panels) producing zero wall flux in the Full Potential equation residuals. Consequently, the edge velocity equations do not detect the sawtooth distribution, and the magnitude of the saw-

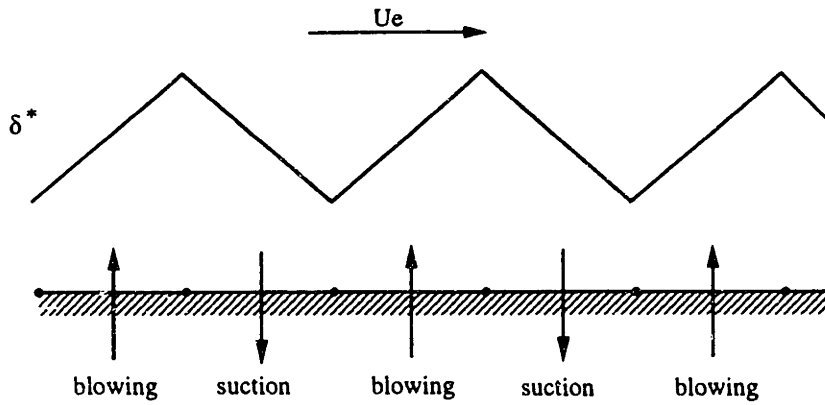


Figure 4.1: Sawtooth in δ^*

tooth distribution can be any value. In three dimensions, the checkerboard mode as well as the sawtooth distributions mode lies in the null space.

This null space of the blowing and FP equations is not an issue in attached flow because the boundary layer equations do not allow δ^* wiggles for a smooth edge velocity distribution, but in separated flow neither the inviscid nor the viscous equations constrain the sawtooth in δ^* . *The result is an ill conditioned Jacobian matrix in separated flows.*

To make this concept concrete, examine the system of coupled equations for a simplified two-dimensional Full Potential and boundary layer VII scheme:

$$\text{Full Potential Equation BC:} \quad \frac{\partial \phi}{\partial n} - \frac{\partial}{\partial s}(u_e \delta^*) = 0$$

$$u_e \text{ Equation:} \quad u_e - \left(u_{\infty,s} + \frac{\partial \phi}{\partial s} \right) = 0$$

$$\text{BL Equation:} \quad \frac{\partial \delta^*}{\partial s} - \left[A + B \frac{\partial u_e}{\partial s} \right] = 0$$

The BL equation is a combination of the von Karman integral momentum equation and the 2-D kinetic energy equation so as to eliminate $\frac{\partial \theta}{\partial s}$. The coefficient $B \rightarrow \infty$ at separation.

Using finite differences, the discretization of these three equations becomes:

$$R_\phi = \frac{(\phi_{i,j+1} - \phi_{i,j})}{\Delta n} - \frac{(u_{e,i+1}\delta_{i+1}^* - u_{e,i-1}\delta_{i-1}^*)}{2\Delta s}$$

$$R_{u_e} = u_{e,i} - \left(u_{\infty,s} + \frac{(\phi_{i+1,j} - \phi_{i-1,j})}{2\Delta s} \right)$$

$$R_{bl} = \frac{\delta_i^* - \delta_{i-1}^*}{\Delta s} - A - B \frac{u_i - u_{i-1}}{\Delta s}$$

The first two residuals use central differences analogous to the Galerkin FEM that is used in the larger three-dimensional problem. The BL residual uses a box scheme. Notice that the ϕ terms have double subscripts because they are two-dimensional field values while the other terms are BL values with only one subscript.

If these equations are solved using a Newton method, the submatrix which lies on the diagonal of the global Jacobian matrix is represented by:

$$\begin{pmatrix} \delta\phi_{i,j} & \delta u_{e,i} & \delta\delta_i^* \\ -\frac{1}{\Delta n} & 0 & 0 \\ 0 & 1 & 0 \\ 0 & \left(\frac{\partial R_{bl}}{\partial u_e}\right)_i & \left(\frac{\partial R_{bl}}{\partial \delta^*}\right)_i \end{pmatrix}$$

where the sensitivities of the BL equation are expressed symbolically because they use rather complicated closure relations.

After row scaling, $\frac{\partial R_{bl}}{\partial \delta^*} \sim \frac{1}{B}$. In attached flow $\left(\frac{\partial R_{bl}}{\partial \delta^*}\right)_i$ is negative, but as the flow separates this sensitivity goes through zero. Since this term is on the diagonal and there is no fill-in for this slot, the global Jacobian matrix becomes ill conditioned in separated flow. Paradoxically, the purpose of the Fully Simultaneous method is to have a numerically stable scheme in separated flow. The present instability is an artifact of the way the VII equations are discretized and any boundary layer coupling method that uses this discretization will be ill conditioned in separated flow.

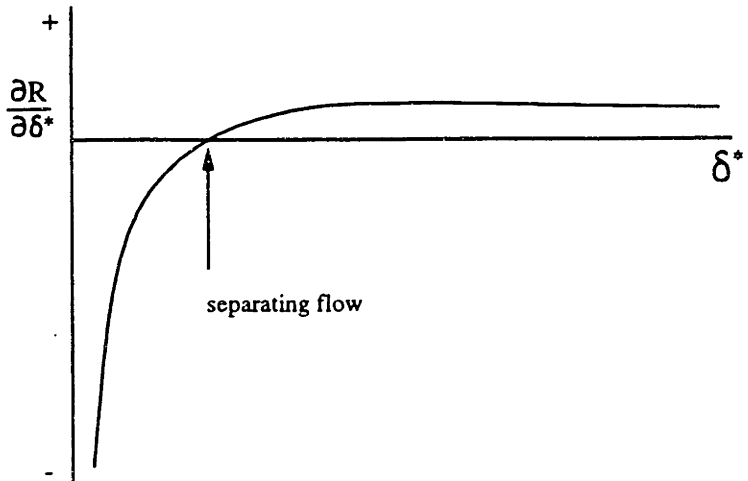


Figure 4.2: BL sensitivity in separating flow

4.3.2 A Remedy

The sawtooth δ^* displacement body of §4.3.1 should produce edge velocities that accelerate over the crests and decelerate over the troughs. This suggests the application of a subgrid model (see for example [15, pp. 101-102]). One subgrid model is to implant local sources and sinks on the BL surfaces. These sources/sinks have strengths equal to the local wall transpiration and they only affect the edge velocities at the given panel's nodes.

The resulting kick in velocity is equal to the velocity perturbation of a 2-D source

$$\Delta u_e = \frac{\sigma}{2\pi r} \quad (4.6)$$

$$\sigma = 2V_w \Delta s$$

σ is the source/sink strength, r is the distance from the source/sink to the node in the direction of the edge velocity, and Δs is the length of the BL panel (see figure 4.4).

The total nodal contribution from two adjacent panel (using $V_w \Delta s = \Delta (u_e \delta^*)$) is given by:

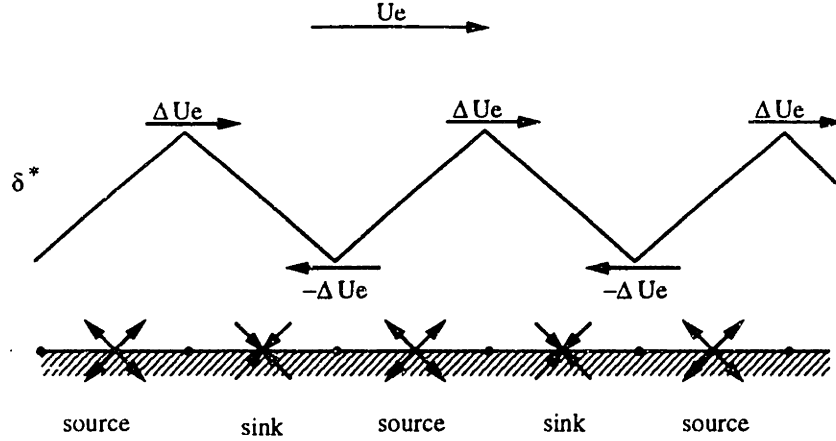


Figure 4.3: Source Sink Subgrid Model

$$\begin{aligned}
 \Delta u_{ei} &= \frac{2(u_{ei+1}\delta_{i+1}^* - u_{ei}\delta_i^*)}{2\pi r} - \frac{2(u_{ei}\delta_i^* - u_{ei-1}\delta_{i-1}^*)}{2\pi r} \\
 &= -\frac{1}{\pi r} (u_{ei+1}\delta_{i+1}^* - 2u_{ei}\delta_i^* + u_{ei-1}\delta_{i-1}^*)
 \end{aligned} \tag{4.7}$$

This provides the necessary velocity perturbation. If the curvature of the δ^* distribution is negative (a crest), Δu_e will be positive. Furthermore, the resulting submatrix is given by:

$$\begin{pmatrix}
 \delta\phi_{i,j} & \delta u_{ei} & \delta\delta_i^* \\
 -\frac{1}{\Delta n} & 0 & 0 \\
 0 & 1 + \frac{2\delta_i^*}{\pi r} & \frac{2u_{ei}}{\pi r} \\
 0 & \left(\frac{\partial R_{bl}}{\partial u_e}\right)_i & \left(\frac{\partial R_{bl}}{\partial \delta^*}\right)_i
 \end{pmatrix}$$

After Gaussian elimination, the lower left term becomes $\left(\frac{\partial R_{bl}}{\partial \delta^*}\right)_i + c \frac{2u_e}{\pi r}$ where $c < 0$. Hence, the source/sink subgrid model keeps the global Jacobian matrix from becoming ill conditioned.

In three dimensions, point sources/sinks placed in the center of BL panels will prevent sawtooth distributions in the displacement body. However, checkerboard modes will be transparent to this source/sink subgrid model. Instead, 2-D source sinks may be placed

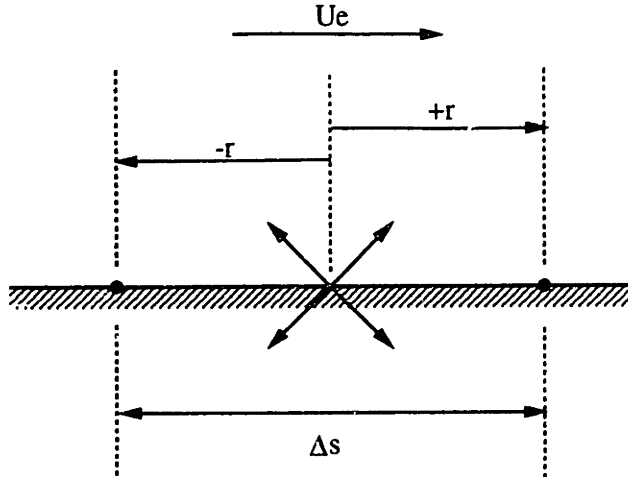


Figure 4.4: Source/Sink Parameters

along panel edges. For a wing with moderate sweep ($< 45^\circ$ say), it has been observed that the outer streamwise flow is primarily in the chordwise direction, except at the very tip. And as a good approximation, the crossflow direction is in the direction of the spanwise generators. Hence, source/sinks based on δ_1^* may be placed on chordwise strips, and source/sinks based on δ_2^* may be positioned on spanwise generators.

For example, the chordwise direction and chordwise velocity are defined by a 3-D unit vector and a dot product:

$$\begin{aligned}\hat{e}_c &= e_{cx}\hat{i} + e_{cy}\hat{j} + e_{cz}\hat{k} \\ u_c &= \vec{q} \cdot \hat{e}_c\end{aligned}\tag{4.8}$$

Then the 2-D source/sink velocity perturbation is given by:

$$\begin{aligned}\Delta u_c &= \frac{2V_{wc}\Delta s}{2\pi r} \\ V_{wc} &= \frac{(u_c\delta_1^*)_i - (u_c\delta_1^*)_{i-1}}{\Delta s}\end{aligned}\tag{4.9}$$

The velocity perturbations in Cartesian coordinates are then:

$$\Delta u = \Delta u_c e_{cx} \quad \Delta v = \Delta u_c e_{cy} \quad \Delta w = \Delta u_c e_{cz} \quad (4.10)$$

A similar expression exists for the spanwise generator direction, except that δ_2^* is used in the source strength. In addition, there is a negative sign because by convention $\delta_2^* \sim \int -u_s d\eta$:

$$\begin{aligned} \Delta u_s &= \frac{2V_{ws}\Delta s}{2\pi r} \\ V_{ws} &= -1 \times \frac{(u_s\delta_2^*)_i - (u_s\delta_2^*)_{i-1}}{\Delta s} \end{aligned} \quad (4.11)$$

The modified velocity formula for stable VII calculations is given by:

$$\begin{aligned} (R_u)_i &= \iint_{\partial\Omega_{bl}} N_i \left\{ \sum_j N_j u_j - \left(u_\infty + \sum_j \frac{\partial N_j}{\partial x} \phi_j + \Delta u \right)_{bl} \right\} dS \\ (R_v)_i &= \iint_{\partial\Omega_{bl}} N_i \left\{ \sum_j N_j v_j - \left(v_\infty + \sum_j \frac{\partial N_j}{\partial y} \phi_j + \Delta v \right)_{bl} \right\} dS \\ (R_w)_i &= \iint_{\partial\Omega_{bl}} N_i \left\{ \sum_j N_j w_j - \left(w_\infty + \sum_j \frac{\partial N_j}{\partial z} \phi_j + \Delta w \right)_{bl} \right\} dS \end{aligned} \quad (4.12)$$

4.4 Coupling Method

All of residual equations have now been described. There is the Full Potential equation residual (2.11) with a wall transpiration BC (4.2); there are the 3-D integral boundary layer equation residuals (3.11–3.13); and lastly there are the Cartesian edge velocity residuals (4.12). The residuals are functions of the nodal unknowns, $U_i^T = (\phi, u, v, w, C_r^{1/2}, \theta_{11}, \delta_1^*, \delta_2^*)^T$.

Nodes in the field possess only the Full Potential equation residual, while nodes on wing and wake surfaces have the Full Potential residual, boundary layer equation residuals, and edge velocity residuals. A final solution must satisfy all of these residual equations. If \mathbf{R}

is the vector of all the residual equations, and \mathbf{U} is the vector of all the nodal unknowns, then we require that:

$$\mathbf{R}(\mathbf{U}) = \mathbf{0} \quad (4.13)$$

This is a nonlinear set of equations. Previous VII coupling methods divided \mathbf{R} into an inviscid equation vector and a viscous equation vector, and performed a complicated iteration process between the pieces (see the flow diagrams of Chapter 1). The Fully Simultaneous coupling method, on the other hand, solves the residual vector as a whole. This is achieved by using the Newton Method described in the next chapter.

Chapter 5

Solution Process

5.1 Newton Method

The equations represented by 4.13 are solved using the standard Newton Method:

1. Initialize \mathbf{U} , the global unknowns vector

2. Compute the residuals vector, \mathbf{R} , and the Jacobian matrix $\left\{ \frac{\partial \mathbf{R}}{\partial \mathbf{U}} \right\}$

3. Find the solution to the linear system

$$\left\{ \frac{\partial \mathbf{R}}{\partial \mathbf{U}} \right\} \delta \mathbf{U} = -\mathbf{R}$$

4. Update the solution $\mathbf{U}^{n+1} = \mathbf{U}^n + \delta \mathbf{U}$, where n is the iteration counter

5. Iterate (steps 2-4) until converged ($\mathbf{R} = \mathbf{0}$ or $\delta \mathbf{U} = \mathbf{0}$)

5.2 Assembling the Jacobian system

The flowfield is divided into 8-node volume elements with 4-node surface elements (or panels). Each node is assigned one or eight degrees-of-freedom (DOF) for its local unknowns vector, \mathbf{U}_i . Inviscid nodes have one DOF, $\mathbf{U}_i^T = \{\phi\}_i^T$, and viscous nodes have eight DOF, $\mathbf{U}_i^T = \{\phi, u, u, w, C_r^{1/2}, \theta_{11}, \delta_1^*, \delta_2^*\}_i^T$. The global unknowns vector, \mathbf{U} , is comprised of the local nodal unknowns vectors:

$$\mathbf{U} = \begin{pmatrix} \vdots \\ \left\{ \phi \right\}_i \\ \phi \\ u \\ v \\ w \\ C_r^{1/2} \\ \theta_{11} \\ \delta_1^* \\ \delta_2^* \\ \vdots \\ \vdots \end{pmatrix}_{i+1} = \begin{pmatrix} \vdots \\ U_i \\ U_{i+1} \\ \vdots \end{pmatrix}$$

In addition, nodes have one or eight equations in their local residual vectors, R_i . Inviscid nodes have the Full Potential equation, while viscous nodes have the Full Potential equation, three velocity definition equations, and four boundary layer equations. The local residual vectors make up the global residual vector, \mathbf{R} .

The Newton system appears as:

$$\begin{pmatrix} \frac{\partial R_1}{\partial U_1} & \frac{\partial R_1}{\partial U_2} & \frac{\partial R_1}{\partial U_{glb}} \\ \frac{\partial R_2}{\partial U_1} & \frac{\partial R_2}{\partial U_2} & \frac{\partial R_2}{\partial U_{glb}} \\ \vdots & & \vdots \\ \frac{\partial R_i}{\partial U_j} & \frac{\partial R_i}{\partial U_{glb}} & \delta U_i \\ \vdots & & \vdots \\ \frac{\partial R_n}{\partial U_n} & \frac{\partial R_n}{\partial U_{glb}} & \delta U_n \\ \frac{\partial R_{glb}}{\partial U_j} & \frac{\partial R_{glb}}{\partial U_{glb}} & \delta U_{glb} \end{pmatrix} = - \begin{pmatrix} R_1 \\ R_2 \\ \vdots \\ R_i \\ \vdots \\ R_n \\ R_{glb} \end{pmatrix} \quad (5.1)$$

where the $\frac{\partial R_i}{\partial U_j}$ matrix elements are 1×1 or 8×8 submatrices. The U_{glb} are global DOF's corresponding to global residual equations R_{glb} (e.g. C_L -specified equation).

5.2.1 Global Equation Numbers

The numbering of nodes has a large effect on the structure of the Jacobian matrix and hence the cost of solving the linear system. For unstructured meshes, algorithms have been written to generate nodal numbers that produce an “optimal” matrix structure. This is beyond the scope of this research, and in the test cases that follow a structured grid is converted into an unstructured mesh and the nodes are numbered such that the bandwidth of the matrix is minimized.

The equation numbers may be determined systematically and accessed cleanly with an identification array, $ID(m, n)$, from reference [6]. m is the local DOF number, which is a number from one to eight and n is the global node number. Initially, the ID array is zeroed out, each node is visited and all active DOF ($m = 1$ for inviscid nodes, $m = 1, \dots, 8$ for viscous nodes) are toggled to a value of one in the ID array. Then, each node is re-visited and a sequential global equation number is assigned to each $ID(m, n)$ member that has a value of one. For example, the equation number for node 5178, degree-of-freedom 3, may be found in $ID(3, 5178)$.

5.2.2 Matrix Mapping

Sparse matrices are usually stored using a set of one-dimensional arrays. One combination is to store the row, column and matrix entries in the arrays $IMAT(n)$, $JMAT(n)$, and $AMAT(n)$; where n goes from 1 to the number of nonzeros, NZ . In this research the row & column indices (i, j) of all non-zeroes, known as the *map* of the matrix, must be constructed before the matrix can be assembled.

The mapping procedure amounts to using the FEM connectivity array and the ID array to determine all of the (i, j) indices for the non-zeroes. An efficient way to build the map is to use a skipping array which stores the number of n indices that must be skipped to find the next occurrence of i . To make this clear take the following matrix to be mapped.

$$\begin{pmatrix} a_{11} & 0 & a_{13} & 0 & 0 \\ 0 & a_{22} & a_{23} & 0 & 0 \\ 0 & 0 & a_{33} & 0 & 0 \\ a_{41} & 0 & 0 & a_{44} & a_{45} \\ 0 & a_{52} & a_{53} & 0 & a_{55} \end{pmatrix}$$

First, the diagonal entries are mapped and stored sequentially in *IMAT*, *JMAT*:

$$IMAT^T = \left\{ 1 \ 2 \ 3 \ 4 \ 5 \ 0 \ 0 \ 0 \ 0 \ 0 \ 0 \right\}^T$$

$$JMAT^T = \left\{ 1 \ 2 \ 3 \ 4 \ 5 \ 0 \ 0 \ 0 \ 0 \ 0 \ 0 \right\}^T$$

$$JSKIP^T = \left\{ 0 \ 0 \ 0 \ 0 \ 0 \ 0 \ 0 \ 0 \ 0 \ 0 \ 0 \right\}^T$$

Now assume that there is a non-zero required in matrix position (4, 5) based on connectivity and *ID* array information. First, the diagonal ($n = 4$) will be checked. Because this is not a diagonal entry and $JSKIP(4) = 0$, this is a new member of the map. So it is appended to the *IMAT*, *JMAT* arrays and *JSKIP*(4) is set to the number of n entries that need to be skipped in order to reach the next $i = 4$ entry: in this case $JSKIP(4) = 2$.

$$IMAT^T = \left\{ 1 \ 2 \ 3 \ 4 \ 5 \ 4 \ 0 \ 0 \ 0 \ 0 \ 0 \right\}^T$$

$$JMAT^T = \left\{ 1 \ 2 \ 3 \ 4 \ 5 \ 5 \ 0 \ 0 \ 0 \ 0 \ 0 \right\}^T$$

$$JSKIP^T = \left\{ 0 \ 0 \ 0 \ 2 \ 0 \ 0 \ 0 \ 0 \ 0 \ 0 \ 0 \right\}^T$$

Now assume that (4, 1) needs to be mapped. Again, the diagonal will be examined. Since there is no match, the algorithm determines that $JSKIP(4) = 2$ and checks the $4 + 2$ entry of *IMAT*, *JMAT*. There is no match and $JSKIP(6) = 0$, so it appends (4, 1) to the *IMAT*, *JMAT* arrays and sets *JSKIP*(6) = 1.

$$IMAT^T = \left\{ 1 \ 2 \ 3 \ 4 \ 5 \ 4 \ 4 \ 0 \ 0 \ 0 \ 0 \ 0 \right\}^T$$

$$JMAT^T = \left\{ 1 \ 2 \ 3 \ 4 \ 5 \ 5 \ 1 \ 0 \ 0 \ 0 \ 0 \ 0 \right\}^T$$

$$JSKIP^T = \left\{ 0 \ 0 \ 0 \ 2 \ 0 \ 1 \ 0 \ 0 \ 0 \ 0 \ 0 \ 0 \right\}^T$$

This process continues until all (i, j) 's are mapped. The *JSKIP* strategy was devised by the author and Darmofal [13]

5.2.3 Column Format

After the matrix is mapped, the (i, j) indices are condensed into an efficient column format [48]. All nonzeros are grouped by columns and re-stored in the one-dimensional arrays of §5.2.2. The first array (*JMAT*) contains the indices pointing to the beginning of matrix columns stored in the other two arrays, the second array (*IMAT*) contains the global row numbers for each matrix non-zero, and the third array (*AMAT*) contains the actual matrix values. For example the matrix:

$$\begin{pmatrix} a_{11} & 0 & a_{13} & 0 & 0 \\ 0 & a_{22} & a_{23} & 0 & 0 \\ 0 & 0 & a_{33} & 0 & 0 \\ a_{41} & 0 & 0 & a_{44} & a_{45} \\ 0 & a_{52} & a_{53} & 0 & a_{55} \end{pmatrix}$$

is stored as follows:

$$JMAT^T = \left\{ 1 \ 3 \ 5 \ 9 \ 10 \ 11 \right\}^T$$

$$IMAT^T = \left\{ 1 \ 4 \ | \ 2 \ 5 \ | \ 3 \ 1 \ 2 \ 5 \ | \ 4 \ | \ 5 \ 4 \right\}^T$$

$$AMAT^T = \left\{ a_{11} \ a_{41} \ | \ a_{22} \ a_{52} \ | \ a_{33} \ a_{13} \ a_{23} \ a_{53} \ | \ a_{44} \ | \ a_{55} \ a_{45} \right\}^T$$

where the `|` symbols demarcate the columns. The last entry of `JMAT` indicates the total number of non-zeros of the matrix. Note that the columns are loaded such that the first column entry is the diagonal followed by the other non-zero column members in ascending row order.

5.2.4 Assembly Process

The Jacobian matrix is assembled in standard FEM fashion. First, volume elements are visited and the Full Potential contributions are added to the residual vector and the Jacobian matrix, and surface elements are visited and the boundary layer equation contributions are added to the system. Next the wall transpiration and edge velocity contributions are added. Lastly the boundary conditions are applied to the system.

The `ID` array and the FEM connectivity array provide the global (i, j) indices associated with the DOF within an element. Given column j , the `IMAT` array is searched for row i within array members $n_{begin} = JMAT(j)$ and $n_{end} = JMAT(j + 1) - 1$. When the i value is matched for $n = n_{match}$, the sensitivity contribution is loaded in `AMAT(nmatch)`. The row search is conducted using a bisection method [43].

As an example, given the previous matrix and a contribution for $(i, j) = (2, 3)$, the `IMAT` array is searched from $n_{begin} = JMAT(3) = 5$ and $n_{end} = JMAT(4) - 1 = 8$ for the value 2. This occurs at $n = 7$ in the `IMAT` array.

5.3 Linear System Solution

For a typical problem, the resulting Jacobian matrix is large ($\sim \mathcal{O}(100,000)$ equations), sparse ($\sim \mathcal{O}(0.05\%)$ non-zero entries), and non-symmetric. There are several iterative techniques designed to solve such matrices [48], and the method used here is the GMRES algorithm of Saad and Schultz [44]. This is one of the Krylov subspace methods which compute a series of orthogonal vectors or search directions using a “Gram-Schmidt”-like

process. A solution to the linear problem

$$\mathbf{A} \mathbf{x} = \mathbf{b}$$

is estimated with a set of search directions ($\mathbf{v}_0, \mathbf{v}_1, \mathbf{v}_2, \dots$) multiplied by scalar weights ($\alpha_1, \alpha_2, \dots$).

$$\mathbf{x} = \mathbf{v}_0 + \alpha_1 \mathbf{v}_1 + \alpha_2 \mathbf{v}_2 + \dots$$

The weights are computed to minimize the error (some vector norm of $\mathbf{b} - \mathbf{A} \mathbf{x}$). Typically, 20-30 search directions are used when the system is preconditioned.

In most cases, GMRES will not converge unless the system is preconditioned. Depending upon the matrix, a poor preconditioner may result in an unstable calculation. Elman [18] demonstrates this for two preconditioners ILU(0) and MILU(0) (Incomplete LU factorization with zero fill-in and Modified Incomplete LU factorization) using recursion formulas for the preconditioned systems. In general, however, it is too difficult to predict whether or not a given preconditioner will work for a given problem, and preconditioners are implemented and discarded if they do not work. The preconditioner used in this research is the Incomplete LU decomposition with drop tolerances [66]. This is a particularly robust preconditioner because it tailors itself to the problem at hand through an appropriate level of fill-in.

5.4 Practical Issues

There are several numerical issues which should be mentioned. First, the Jacobian matrix should be row and column scaled for better conditioning. The BL unknowns ($\theta_{11}, \delta_1^*, \delta_2^*$) vary a great deal in magnitude so it is best to compute a logarithmic correction. After the matrix is fully assembled, the matrix columns corresponding to BL thicknesses are multiplied by the thicknesses. For example

$$\frac{\partial R_{ke}}{\partial \theta_{11}} \delta \theta = \left(\frac{\partial R_{ke}}{\partial \theta_{11}} \theta_{11} \right) \left(\frac{\delta \theta_{11}}{\theta_{11}} \right)$$

$$= \frac{\partial R_{ke}}{\partial \log \theta_{11}} \delta \log \theta_{11}$$

Then it is the log-corrections that are computed in the linear system. The regular corrections are calculated by multiplying once again by the boundary layer thicknesses.

$$\delta\theta_{11} = (\delta \log \theta_{11}) \theta_{11}$$

$$= \left(\frac{\delta\theta_{11}}{\theta_{11}} \right) \theta_{11}$$

After the column scaling, the rows are scaled by the largest row term.

In addition, Newton methods usually need under-relaxation or clamping during the calculation process to prevent over-shooting [24]. Each DOF type is clamped differently. The ϕ corrections are under-relaxed such that the new ϕ does not produce vacuum speeds in the flowfield. The u , v , and w are clamped such that a 50% change is not exceeded. The BL variables are clamped such that a 60% change is not exceeded and such that the shape parameter, H_k does not go below 1.0 .

5.4.1 Debugging the Newton Method

Once the residual formulae are validated, the sensitivity formulae may be verified using two methods. The first is to run in double-precision, have GMRES converge its error to machine zero, and check that the program is achieving quadratic convergence.

Another method for catching bugs is *pinging* the elemental sensitivities. First, a state for U_j is set. Then one DOF in the element is perturbed or pinged. The average of the original and pinged analytic sensitivities is compared to the finite difference estimate of the sensitivity. This is best done in double precision with a pinged value of 0.01% of the original U_j . For example, the pinging of an elemental Full Potential residual amounts to

$$\phi_{j,pinged} = (1 + 0.0001) \times \phi_{j,original}$$

$$\left(\frac{\partial R_i}{\partial \phi_j} \right)_{ave} = \frac{1}{2} \left\{ \left(\frac{\partial R_i}{\partial \phi_j} \right)_{org} + \left(\frac{\partial R_i}{\partial \phi_j} \right)_{pinged} \right\}$$

$$\left(\frac{\partial R_i}{\partial \phi_j} \right)_{f.d.} = \frac{(R_i)_{pinged} - (R_i)_{org}}{(\phi_j)_{pinged} - (\phi_j)_{org}}$$

The average analytic sensitivity and the finite difference sensitivity should have a difference of no more than 0.0001% in double-precision. If the elemental sensitivities pass this test, then the global matrix should be properly linearized since it is composed of these elemental linearizations. Both quadratic convergence checking and pinging were invaluable in the construction of the code.

Chapter 6

Results

6.1 Infinite Swept Wing

The FEM discretization and the closure relations of the three-dimensional boundary layer equations were checked against the infinite swept wing experiment of van den Berg and Elsenaar [56]. The experimental set-up is illustrated in Figure 6.1. It is a swept flat plate with guiding vanes, and a separation inducing body placed above. Various 3-D BL quantities were measured at ten stations along the plate.

In theory, a viscous/inviscid calculation of the entire experiment can be done but some features of the geometry were unknown. Consequently, the boundary layer equations were spatially marched using the experimental edge velocities as inputs. This is a direct viscous solver and the calculation breaks down when separation is encountered, or when one of the characteristics of the boundary layer equations becomes perpendicular to the marching direction. The purpose of this case is *not* to check the algorithm's performance in separation, but rather to examine the accuracy of the finite element discretization and the BL model.

The computation was performed over a 101×5 node mesh of the swept flat plate. Natural BC's were imposed on the side boundaries, experimental data at the first measurement station is used as the initial data, and $Re = 2.42 \times 10^6$ and $M_\infty = 0.01$ are the freestream conditions. The computation was halted at $x = 1.1$ because one of the characteristics (associated with the τ_w -direction) becomes perpendicular to the marching direction, while separation actually occurs at $x = 1.3$.

Plots of 3-D boundary layer data are shown in Figure 6.3. The computed BL thicknesses θ_{11} , δ_1^* , and δ_2^* are in excellent agreement with the experimental measurements. β_w , the angle

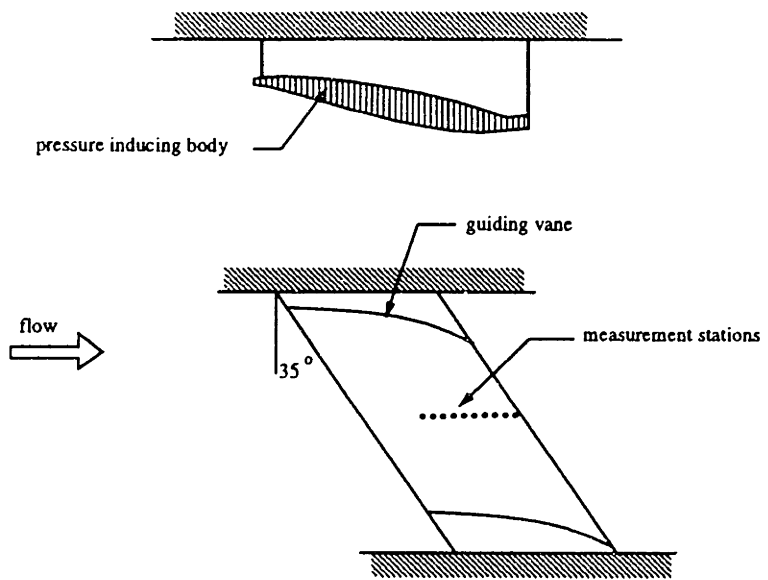


Figure 6.1: van den Berg/Elsenaar Experiment

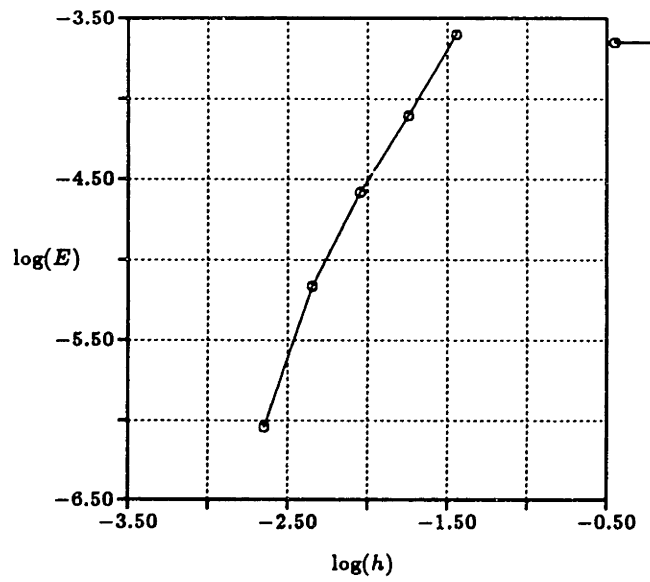


Figure 6.2: Convergence of θ_{11} for Infinite Swept Wing

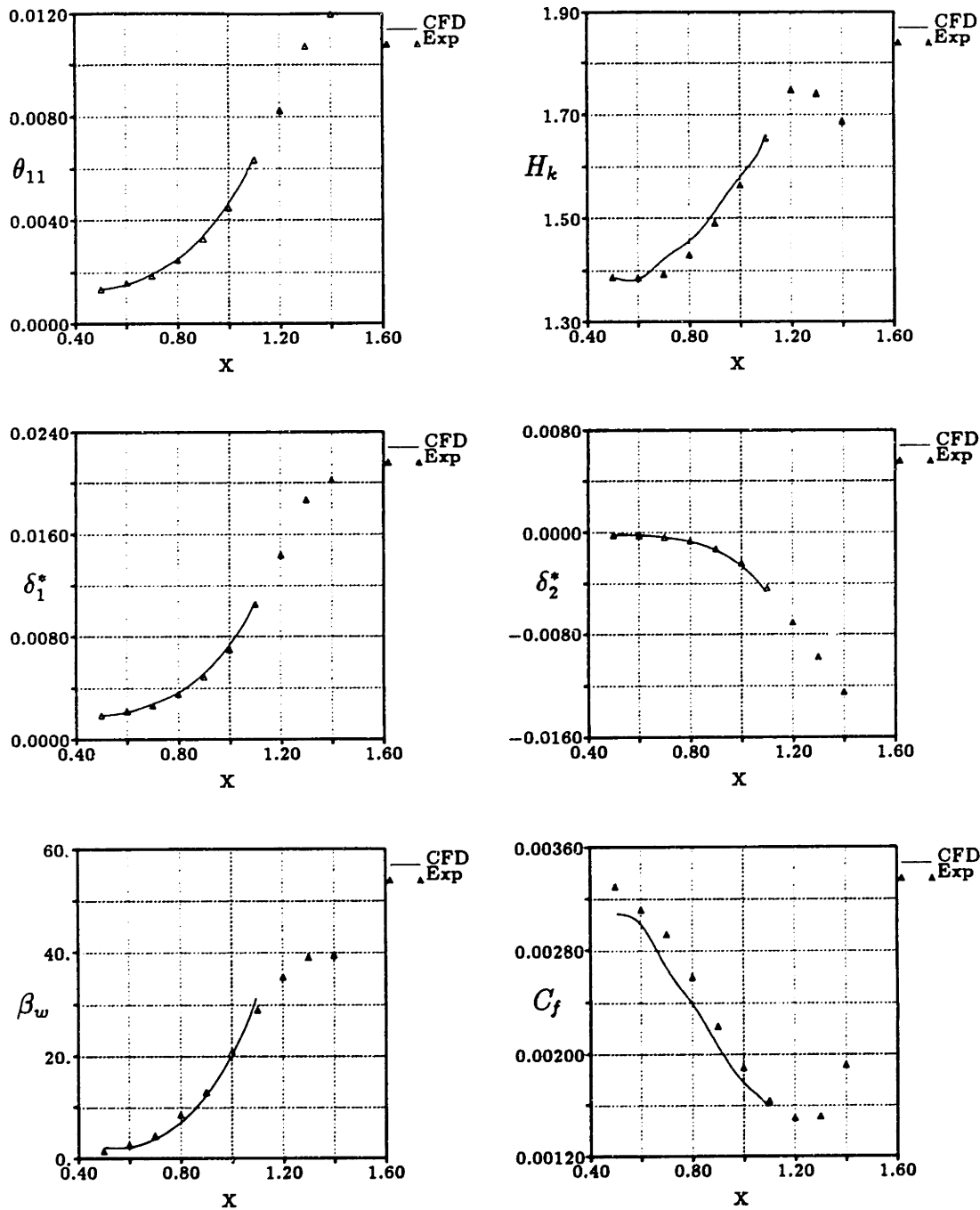


Figure 6.3: Infinite Swept Wing Results

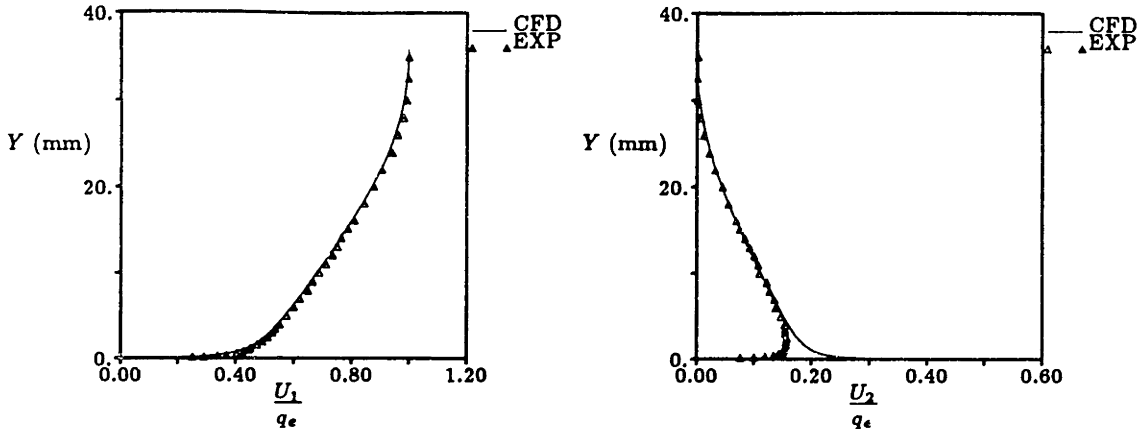


Figure 6.4: Infinite Swept Wing, Velocity Profiles

between the outer flow velocity vector and the limiting streamline, is in close agreement. The skin friction, C_f does not agree as well as the other BL quantities, but it compares as well as, or better than the other 3-D BL codes of Reference [57].

Streamwise and crossflow velocity profiles may be extracted from the integral BL variables [16]. The profiles at $x = 1.00$ (which corresponds to $x = 1020$ mm in the experiment) are plotted in Figure 6.4. The agreement is good, except near the wall layer of the crossflow velocity (U_2) where the limitation of the Johnston triangular crossflow model is evident. The Johnston profile $\frac{u_2}{q_e} = A_c \left(1 - \frac{u_1}{q_e}\right)$ specifies a finite velocity at the wall.

Finally the convergence of the code (based on the convergence of θ_{11} at a particular x -station) was examined using a series of finer meshes. The results are displayed in Figure 6.2, where E is the percent difference between θ_{11} on the current mesh and θ_{11} on the finest mesh: second-order accuracy is exhibited.

6.2 RAE 2822 Airfoil

Next, the viscous/inviscid interaction of the entire code was checked on Case 10 of Cook et. al. [10] which is a commonly used test case for viscous airfoil codes. This case was simulated by a straight wing between two inviscid walls and natural boundary conditions. The Reynolds number, Mach number and lift coefficient were matched ($M_\infty = 0.75$, $C_l =$

0.743 , $Re = 6.2 \times 10^6$), and the flow was tripped at $x/c = 0.05$ on both the upper and lower surfaces. Presented in Figure 6.5 are plots of C_p and H_k vs. experiment for a $129 \times 34 \times 2$ node mesh.

The agreement is reasonable and is on par with other viscous codes for this case [25]. The calculated drag seems extremely accurate, but this is deceptive for as the mesh is refined the computed drag grows larger ($\sim \mathcal{O}(0.0252)$), and further away from the experimental value. Nevertheless, the calculated drag is in good agreement with experiment using this VII method. More importantly, $H_k > 2.9$ behind the shock which indicates turbulent flow separation for typical Re_θ values. This demonstrates the ability of FS coupling to handle separated flows.

Lastly, grid convergence based on C_d was examined. Drag based on farfield (FF) quantities (see Appendix D) and drag based on standard surface integration were calculated, and their convergence as the mesh is refined is shown in Figure 6.6. It shows that the discretization of the entire algorithm is second-order accurate. An interesting point is that the convergence is not too sensitive to the type of drag formula used.

6.3 RAE 101 45-degree Swept Wing

The RAE 101 wing is an untapered wing with a 45-degree sweep and the symmetric RAE 101 airfoil section. In addition to C_p data [60], a small number of 3-D velocity profiles were measured [7] enabling the calculation of experimental BL thicknesses.

Meshes for this wing and the ones that follow were generated by stacking 2-D grids at span stations. Input airfoils were splined in the chordwise direction and linearly interpolated in the spanwise direction. Then 2-D H-H grids were generated using algebraic interpolation formulae [2] and elliptic smoothing [55]. The tip region was constructed by rotating the last H-H grids around the tip creating a rounded tip.

The mesh contained 21,000 nodes with 67 nodes in the chordwise direction and 14

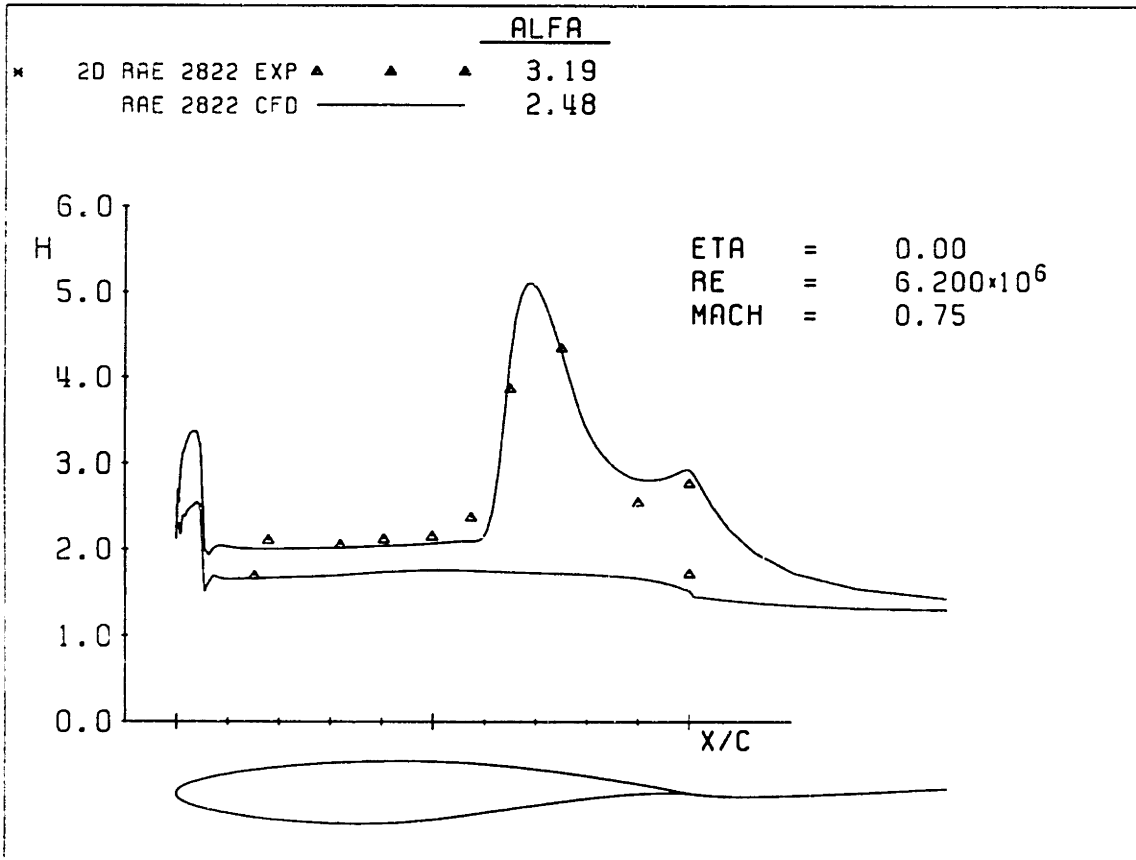
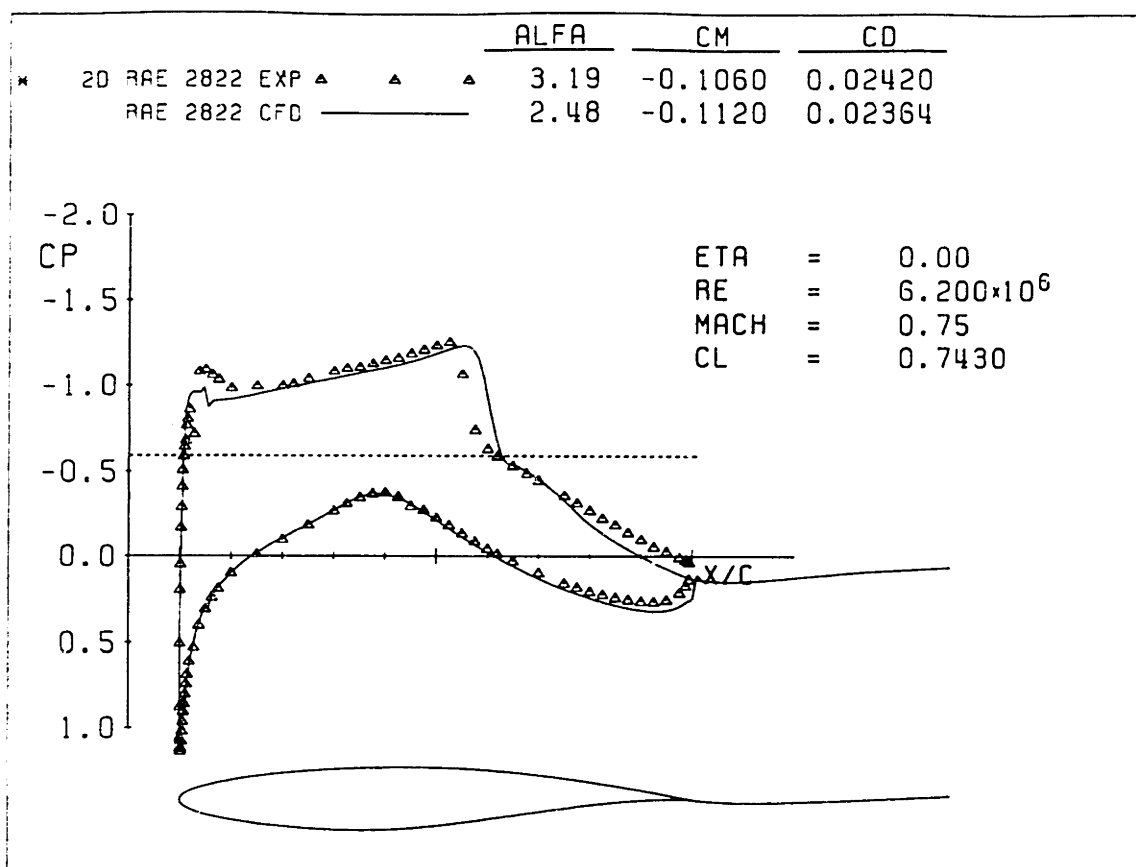


Figure 6.5: Computed C_p and H_k vs. Experiment

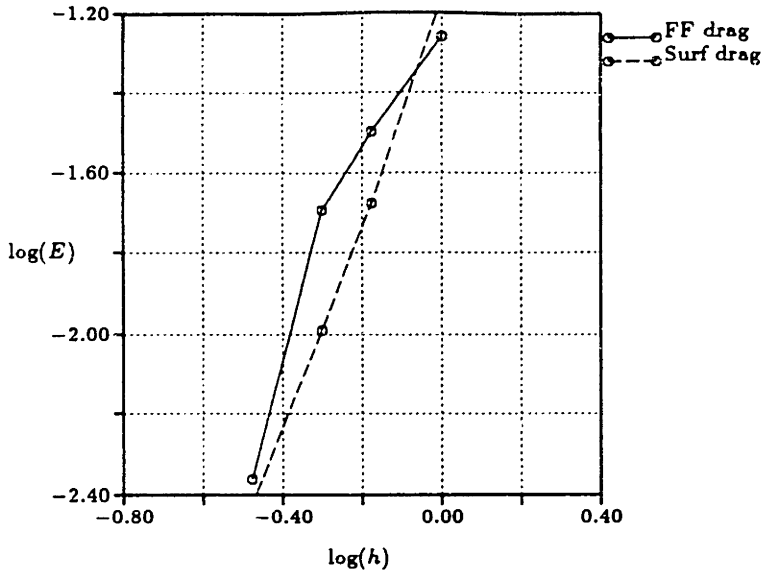


Figure 6.6: Convergence of Drag for RAE 2822

nodes in the spanwise direction. A case which contains noticeable 3-D effects ($M_\infty = 0.179$, $\alpha = 6.3^\circ$, $Re = 2.1 \times 10^6$ based on c_{mac}) is examined in more detail. The transition locations were set to the experimentally observed transition locations [7].

The C_p profiles at four span stations are displayed in Figure 6.7 where the computation is shown as a solid line and the experiment is plotted as symbols. The agreement is good except at tip. This is probably because the tip BC's are very approximate. Upper surface BL thicknesses (θ_{11} , δ_1^* , δ_2^*) for percent span stations $\eta = 0.50$ and $\eta = 0.80$ are displayed in Figure 6.8. The experimental BL data, represented as symbols, was determined by numerically integrating the experimental velocity profiles. The thicknesses are treated as if incompressible ($\rho = \rho_e$) because no density profiles were provided, and because M_∞ is low. The agreement is reasonable, except perhaps the δ_2^* values. Here the correct trends are observed, but the magnitudes are off by 50% to 100%. However, δ_2^* is a very small quantity and small absolute errors become large percentage errors.

Lift and drag computed with a farfield formula and by standard surface integration are displayed in Table 6.1 and Figure 6.9. In the Figure, the farfield formula is represented by the solid line, the surface integration is given by the dashed line, and the experiment is plotted as symbols. The farfield lift formula is Trefftz plane integration of circulation (see

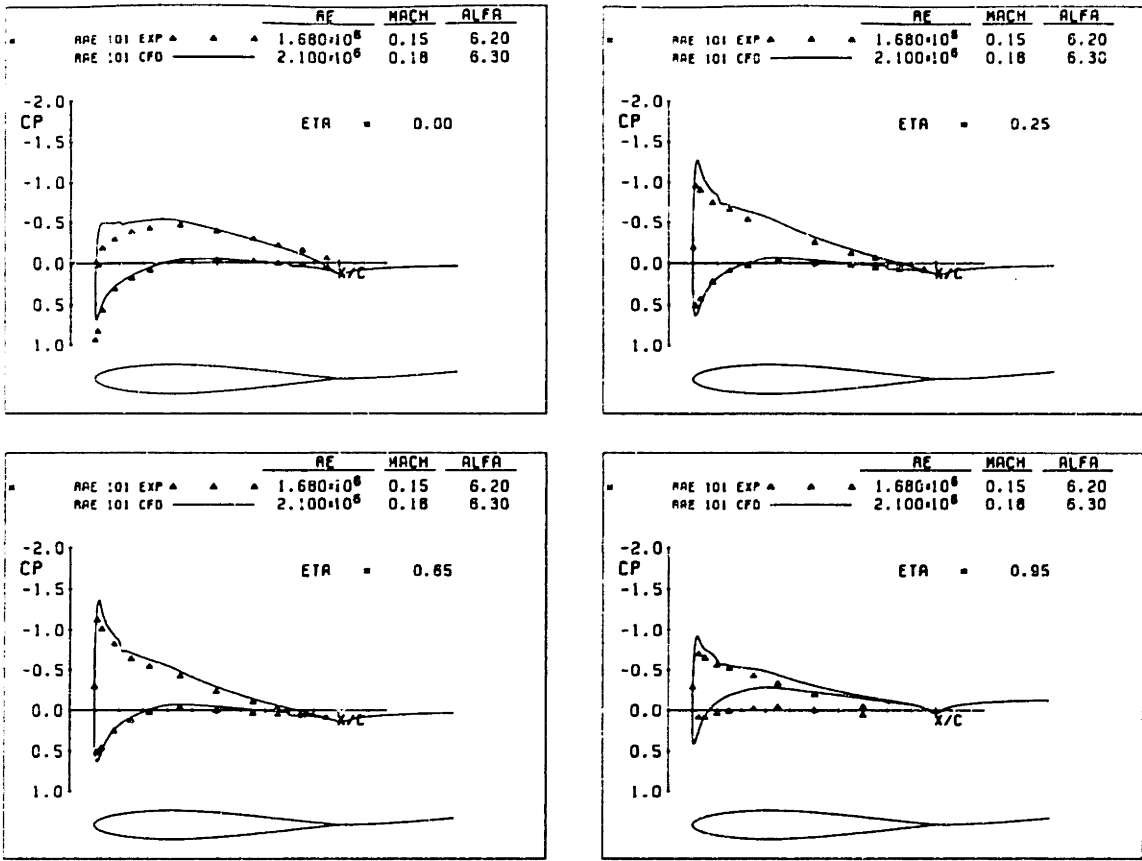


Figure 6.7: RAE 101 Wing, C_p profiles at experimental span stations

Ref. [4]) and the farfield drag formula is derived in Appendix D.

The surface integration is in better agreement with the experiment. However, the farfield formula relies on farfield 3-D momentum integral values (θ_{zz} , θ_{xz} , etc.) and due to numerical difficulties these thicknesses could not be computed (see §6.6). Instead, 2-D thicknesses were used for the drag calculation of Figure 6.9. Hence, this is not a sufficient comparison of the two drag formulae.

Kovalev simulated this experiment (up to $\alpha = 6^\circ$) using a set of 3-D differential boundary layer equations and achieved comparable results in C_L vs. C_D [30].

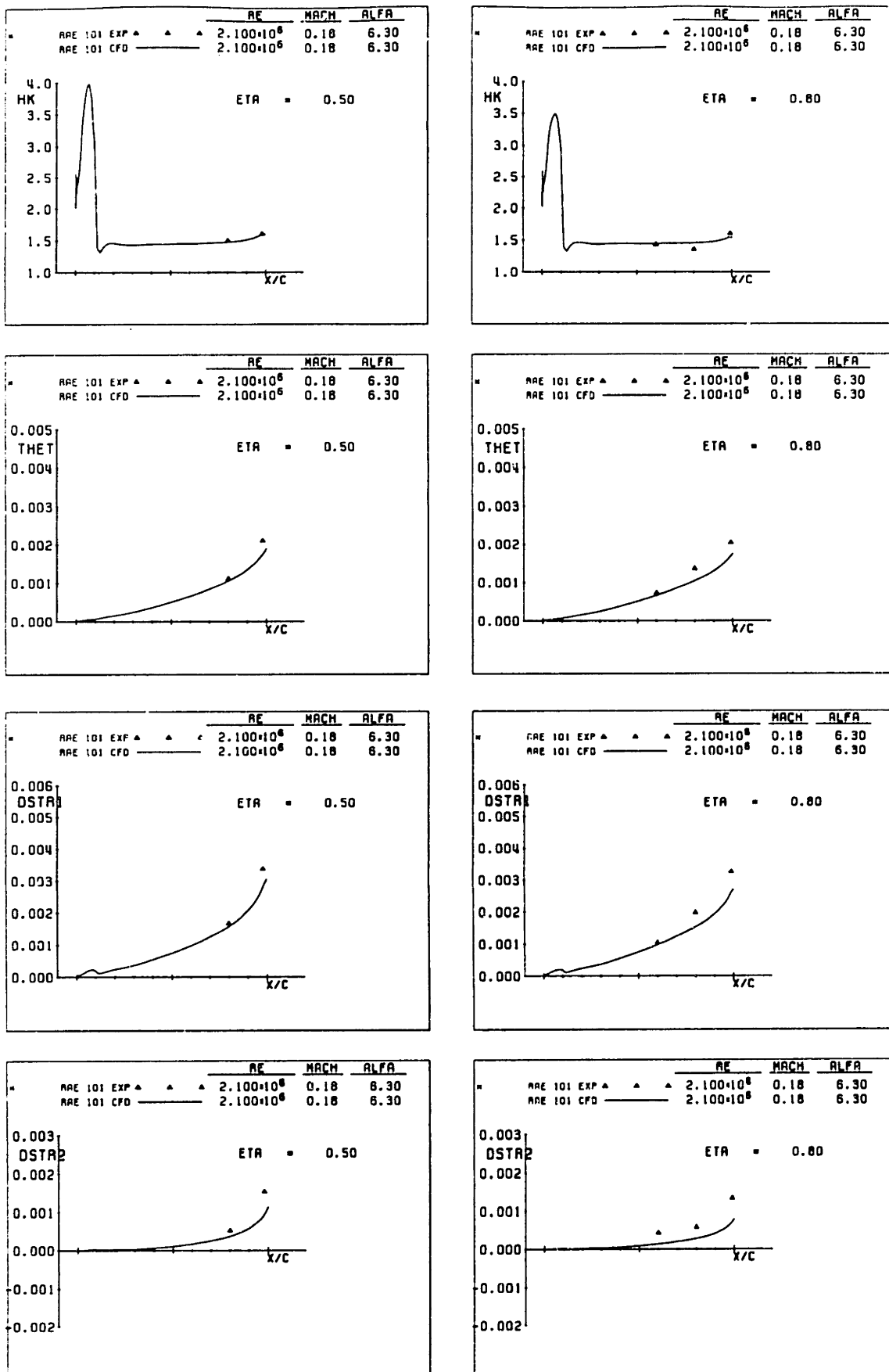


Figure 6.8: RAE 101 Wing, Upper surface BL quantities at $\eta = 0.50$ and $\eta = 0.80$

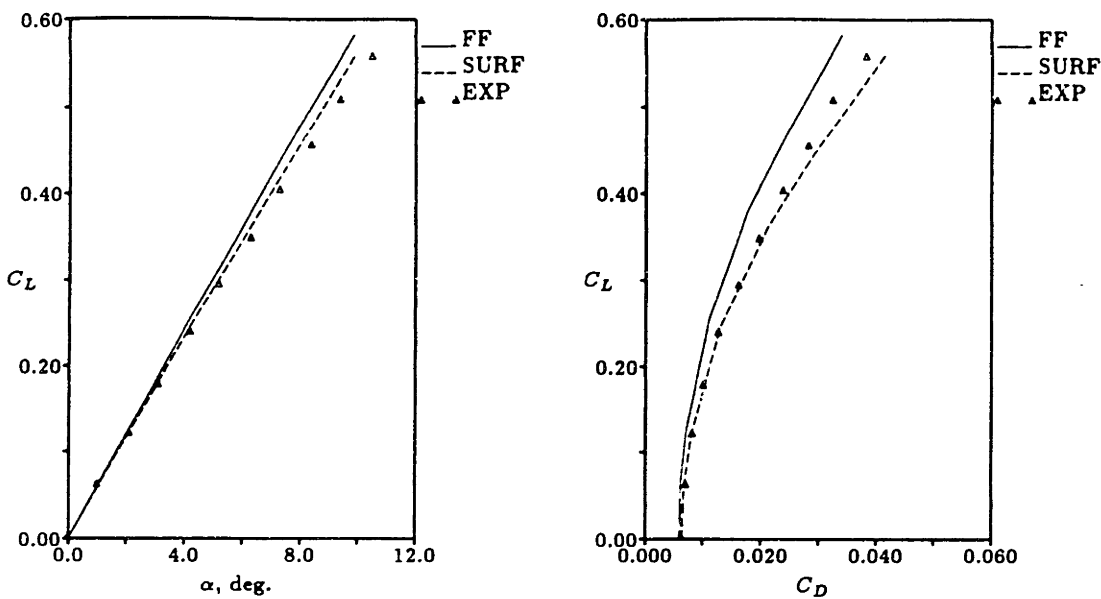


Figure 6.9: RAE 101 45-degree Swept Wing, C_L vs. α and C_L vs. C_D

α	$(C_L)_{\text{EXP}}$	$(C_L)_{\text{FF}}$	$(C_L)_{\text{SURF}}$	$(C_D)_{\text{EXP}}$	$(C_D)_{\text{FF}}$	$(C_D)_{\text{SURF}}$
0.0	0.0040	0.0006	0.0006	0.0064	0.0060	0.0062
1.0	0.0640	0.0604	0.0583	0.0071	0.0062	0.0068
2.1	0.1240	0.1280	0.1237	0.0082	0.0072	0.0081
4.2	0.2410	0.2548	0.2455	0.0127	0.0111	0.0130
6.3	0.3510	0.3789	0.3628	0.0197	0.0176	0.0212
7.9	0.4310	0.4733	0.4507	0.0260	0.0248	0.0297
9.9	0.5350	0.5838	0.5596	0.0354	0.0342	0.0415

Table 6.1: RAE 101 Wing: Force coefficients

6.4 MBB-AVA Wing

The DFVLR MBB-AVA model is a fighter type wing/body configuration with a supercritical wing [29]. Various M_∞ and α combinations were tested, including some cases with extensive rear separation. When separation occurred, it was observed to begin at the trailing edge starting at the tip.

The mesh for this case consisted of 21,000 nodes with 67 nodes in the chordwise direction and 14 span stations. Because of grid generation limitations only the wing was modeled. An attached flow case ($M_\infty = 0.80$, $\alpha = 4.0^\circ$, $Re = 1.26 \times 10^6$ based on c_{mac}) and a separated case ($M_\infty = 0.88$, $\alpha = 2.0^\circ$, $Re = 1.32 \times 10^6$) are presented. The experiment was run with free transition, but because transition is not predicted by the code the flow was tripped near the leading edge—this is a good approximation for high Re , transonic flows over swept wings. At the suggestion of an experienced engineer [17], the flow was tripped at $x/c = 0.05$ and 0.10 on the upper and lower surfaces respectively.

In the sets of C_p plots for both the MBB-AVA wing and Boeing 747 wing, the following conventions should be noted:

- the C_p profiles are at experimental span stations, the CFD data was linearly interpolated to these span stations
- the dotted horizontal lines on the plots indicate C_p^* or where the flow goes supersonic
- the percent span stations (ETA) is printed in the upper-right quadrants of the plots
- the experimental data is represented by the symbols, the VII calculation is given by the solid line and a Full Potential calculation is given by the dashed line

The results for the attached case are shown in Figure 6.10. In the calculation, the small effect of the boundary layer is to push the shock forward which agrees better with experimental data. The experimental data exhibits large separation near the tip ($\eta = 0.92$), but the VII method does not predict this. The discrepancy is probably due to the crudeness of the boundary conditions at the tip.

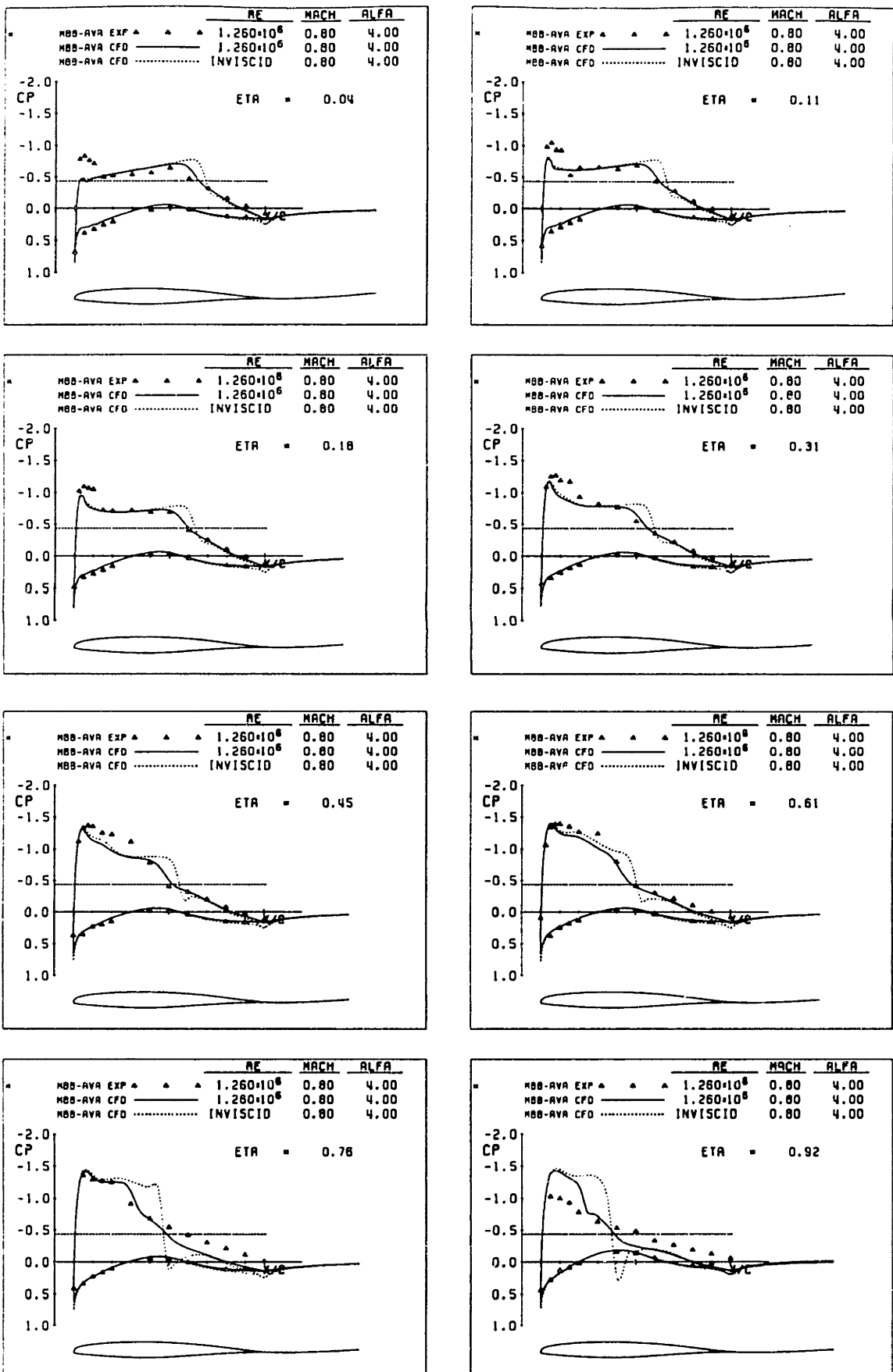


Figure 6.10: MBB-AVA Wing, attached case, C_p at experimental span stations

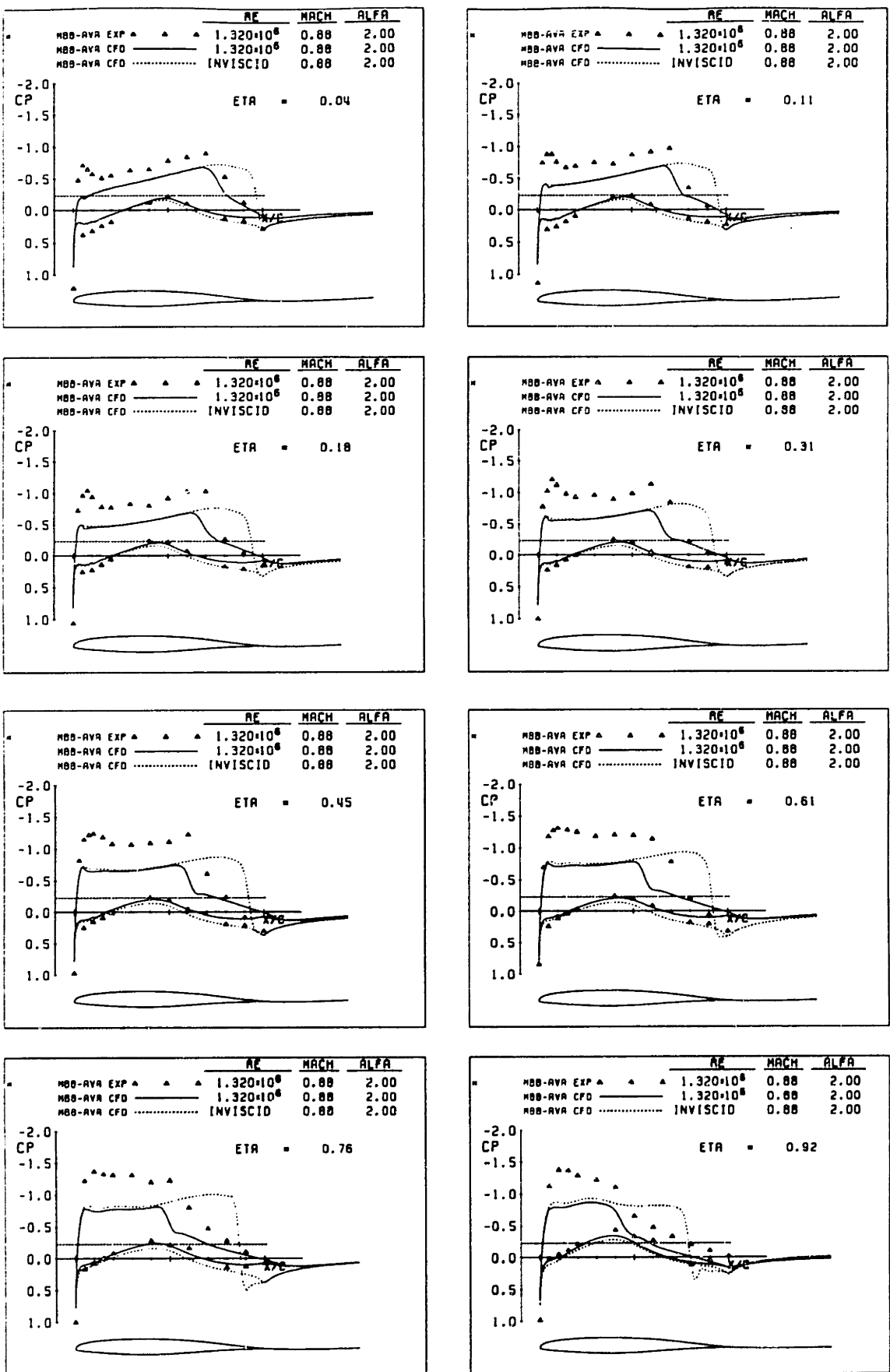


Figure 6.11: MBB-AVA Wing, separated case, C_p at experimental span stations

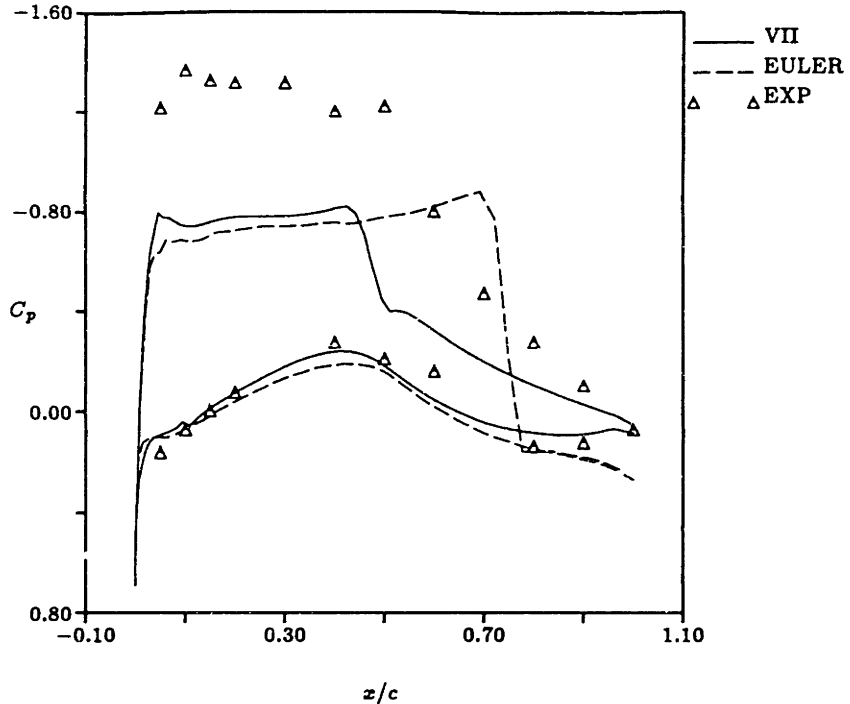


Figure 6.12: C_p distributions at $\eta \approx 0.76$

The results for the separated case are shown in Figures 6.11. The effect of the boundary layer is to move the shocks forward due to the decambering effect of the displacement body. The computed shock locations of the VII method are near the experimental positions, however, the level of the C_p roofs on the upper surface do not match. It is believed that some sort of blockage effects may be responsible since this is a fairly high M_∞ . To lend confidence to this theory, an Euler solution [41] of this case was computed. The C_p profiles for the Euler code, the VII code, and experiment at one span station are displayed in Figure 6.12 and they indicate that the experimental conditions are different than freestream or flight conditions.

The most important feature of this case is the large 3-D separation. A planform view of the upper surface wall shear stress directions is shown in Figure 6.13 and the area where the vectors are pointing upstream and outboard is the separation region. Finally, the total lift and drag coefficients (farfield formula) for $M_\infty = 0.80$ are plotted in Figure 6.14. Viscous effects were small for this range of α so that most of the drag is induced drag. Although the body was not modeled, the lift and drag are in good agreement with experiment.

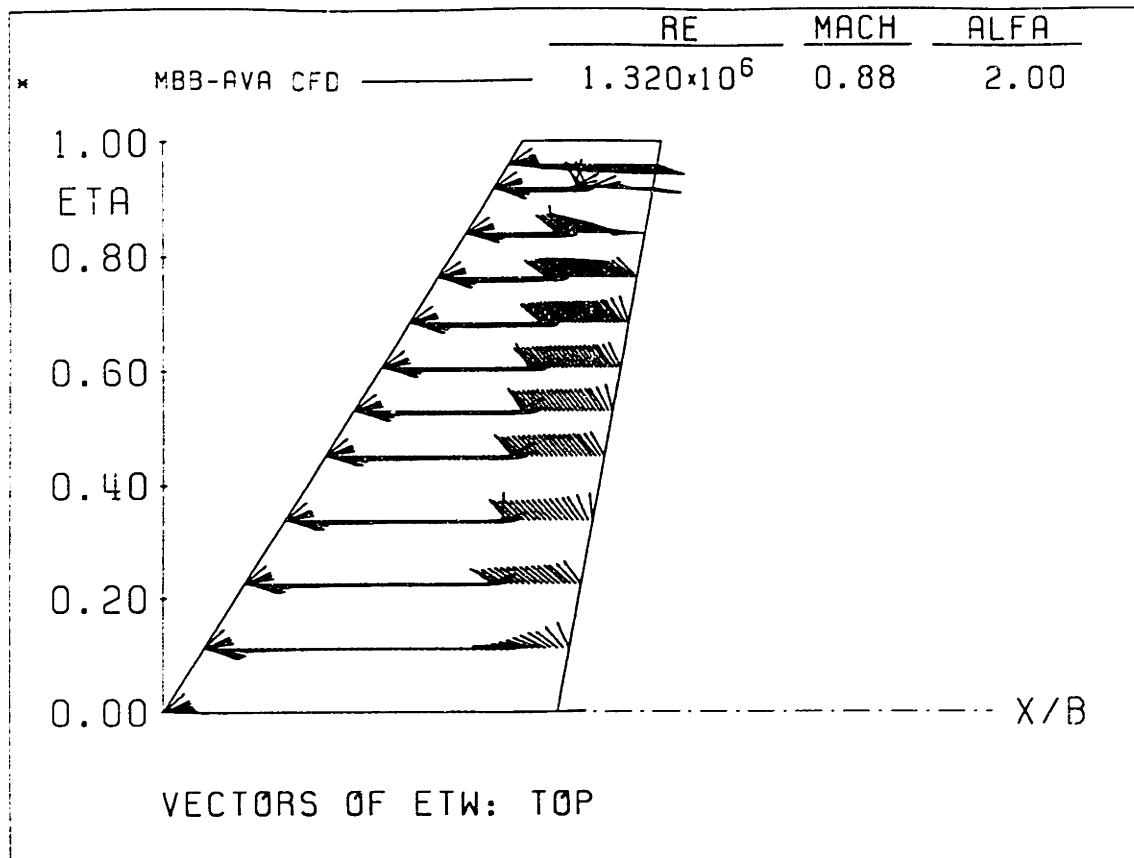


Figure 6.13: MBB-AVA wing, separated case, τ_w direction vectors

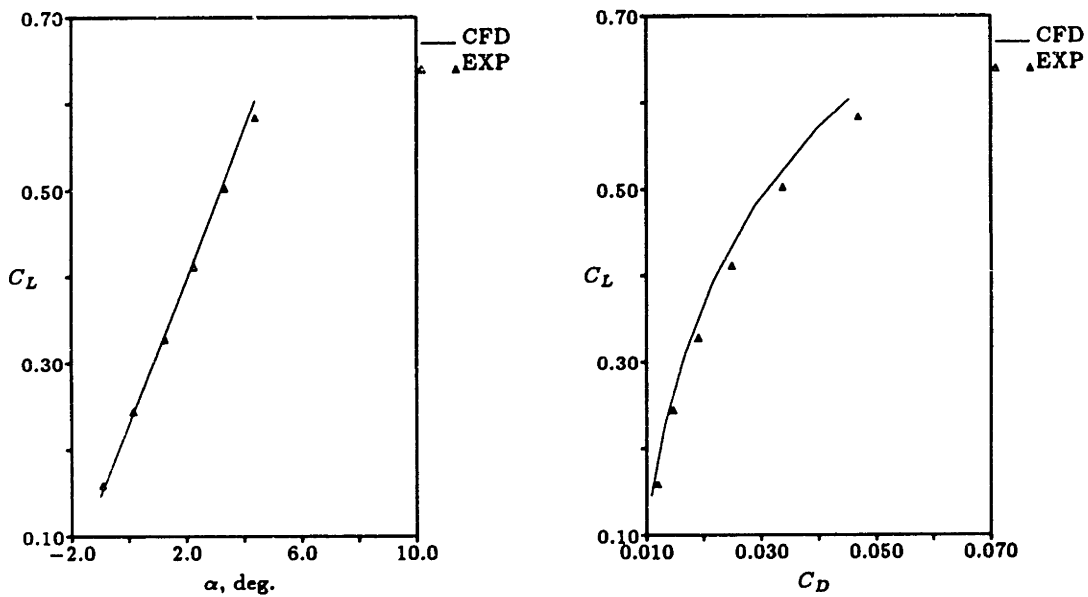


Figure 6.14: MBB-AVA Wing, $M_\infty = 0.80$, C_L vs. α and C_L vs. C_D

6.5 Boeing 747 Wing

The final test case is a Boeing 747 wing from a wing-body experiment for viscous code validation (NASA Ames Transonic Test No. ARC502, 1981). This wing is representative of a commercial transport wing, but it is not the actual production wing.

The mesh possessed 35,000 nodes with 67 nodes in the chordwise direction and 22 nodes in the spanwise direction. Again, only the wing could be gridded. An attached case ($M_\infty = 0.838$, $\alpha = 6.75$, $Re = 7.72 \times 10^6$ per foot) and a separated case ($M_\infty = 0.860$, $\alpha = 6.74$, $Re = 2.12 \times 10^6$ per foot) are presented. The flow was tripped at $x/c = 0.10$ consistent with the experiment. In addition, several corrections were applied to the wing and angle-of-attack:

- The wing possessed 2° incidence relative to the body. [68, 26]
- Twist corrections as a function of α due to aeroelastic effects are applied. This is provided in the test data.
- A -0.35° degree α correction is applied to account for other experimental effects [26]

The pressure distribution for the attached case is displayed in Figure 6.15. The C_p profiles predicted by the VII method are in generally in good agreement with experiment, however at several span stations the shock is somewhat smeared due to lack of grid resolution. The shock locations are also slightly aft of the experimental locations. This may be due to neglecting wake curvature effects in the trailing edge pressures (higher-order boundary layer theory) which ultimately affects the lift. In spite of all its simplifications, the VII method does well.

The pressure distributions for the separated case are shown in Figure 6.16. The shock locations are in generally good agreement with experiment, and separation is evident at $\eta = 0.81$ and $\eta = 0.89$. There is a non-physical C_p gap at the trailing edge, and an improved Kutta condition (incorporating $\frac{\partial p}{\partial n}$ across the BL) may be required.

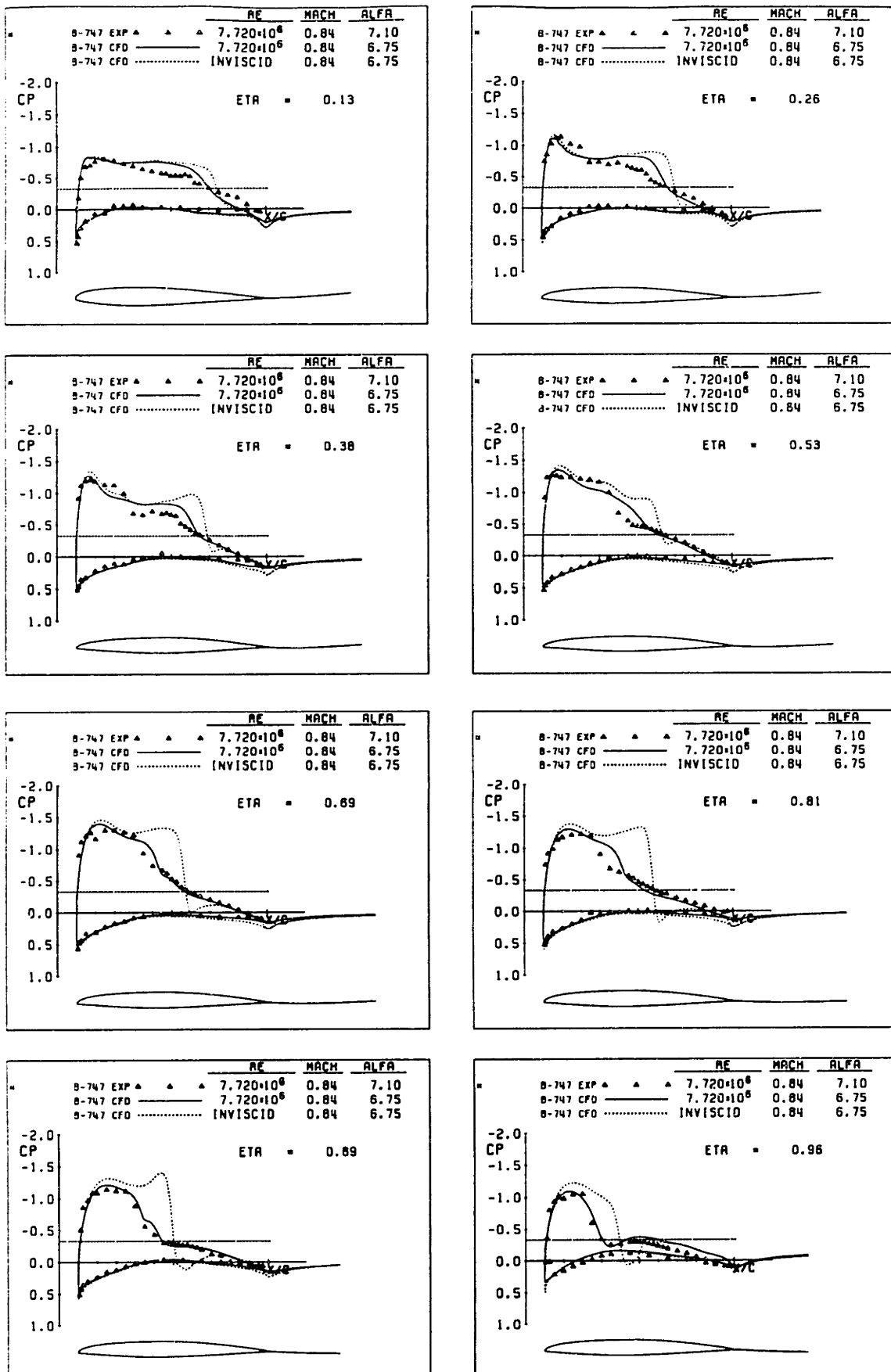


Figure 6.15: B-747 Wing, attached case, C_p at experimental span stations

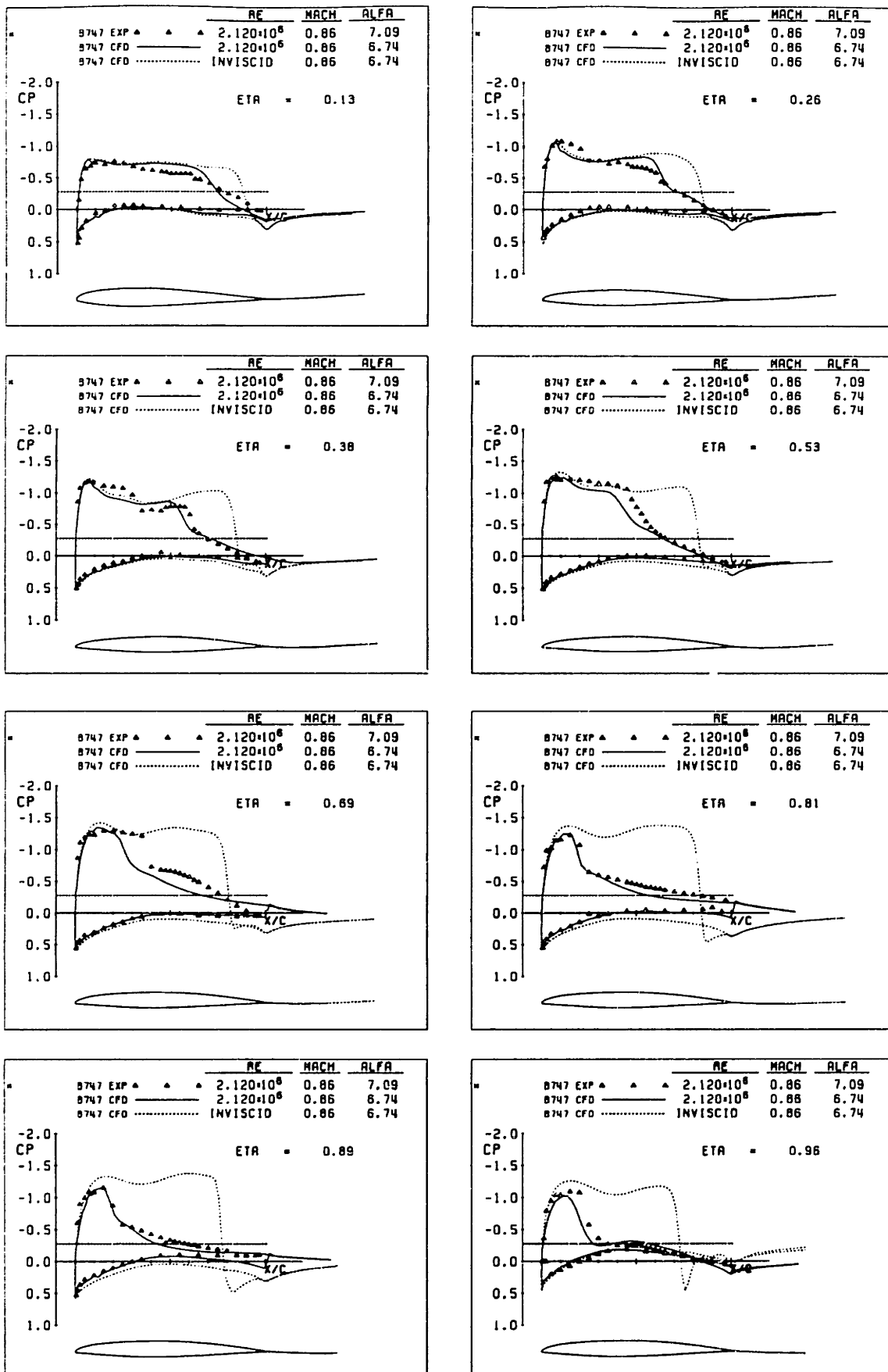


Figure 6.16: B-747 Wing, separated case, C_p at experimental span stations

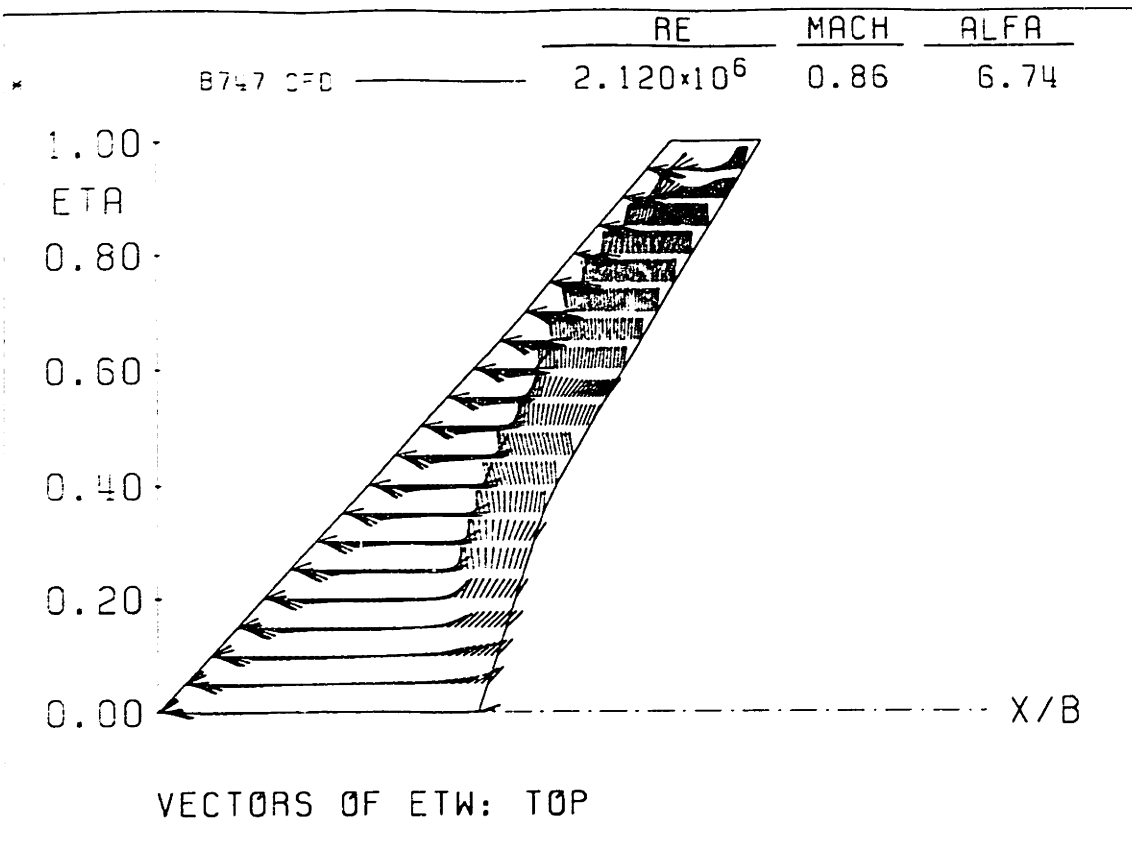


Figure 6.17: B-747 wing, separated case, τ_w direction vectors

The wall shear stress directions are displayed in Figure 6.17. A large portion of the wing is separated demonstrating the ability of FS coupling to handle separated flow.

For $M_\infty = 0.838$, the lift versus angle-of-attack and lift versus viscous and wave drag, C'_D , are presented in Figure 6.18 where $C'_D = C_D - \frac{C_L^2}{\pi AR} - C_{D\alpha=3.69^\circ}$. This modified drag is an attempt to remove the body's drag and the drag due to lift: this reduces the abscissa scale from 1000 drag counts to 500 drag counts for better evaluation. The agreement in drag is not excellent, but it is respectable. However, only a small range of angle-of-attack ($1.69^\circ < \alpha < 5.71^\circ$) could be simulated because the code experienced non-physical behavior ($H_k < 1$) for lower α 's, and non-convergence for higher α 's.

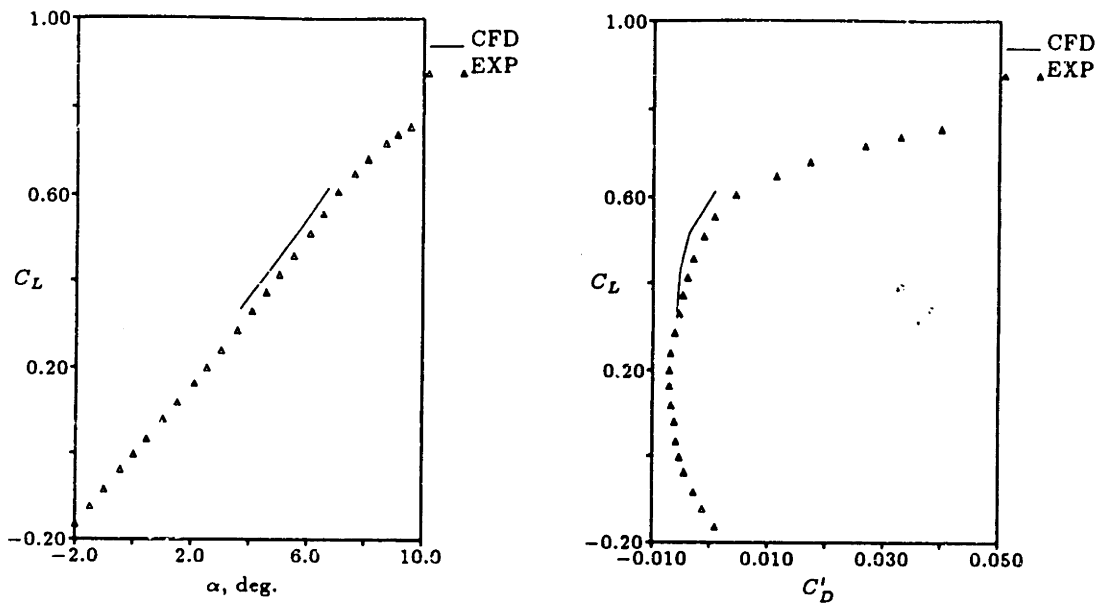


Figure 6.18: B-747 Wing, $M_\infty = 0.838$, C_L vs. α and C_L vs. C_D'

6.6 H_k Difficulties

In lifting cases, the kinematic shape parameter, H_k , on the wake tended to drop below unity. H_k less than unity represents a momentum surplus or jet, and it is entirely non-physical. H_k is controlled by the H^* versus H_k relation (see Equation B.16) where H^* is the streamwise kinetic energy thickness. The problem may be that the crossflow acts like a source of kinetic energy deficit whereby the streamwise k.e. deficit may grow without bound causing H^* to grow larger than 2 and thus H_k to go below 1. These spurious sources may be due to inaccurate 3-D profile correlations, or due to the approximate side boundary conditions.

As a short term fix, the 3-D BL equations are replaced with the 2-D BL equations on the wake several nodes downstream of the trailing edge. Because there is no source of k.e. deficit due to crossflow in the 2-D equations, H_k should not go below 1. It is believed that the solution of the wake has negligible effect on the wing surface solution.

6.7 Performance of the Code

All computations were run on a Silicon Graphics IRIS Indigo 2 with R8800 processor. The vital statistics for the B-747 test case are:

- 35,000 nodes, 57,000 equations, 3 million nonzeros
- 0.001 to 0.0001 drop tolerance, 20 GMRES directions
- Converged solution takes approximately 10 iterations per 2 degree change in angle-of-attack (550 CPU sec per iteration)
- 200 MB of disk space needed to store the ILU preconditioner
- 96 MB of core space needed for program memory

This is a relatively small problem, yet a large amount of memory is required because the Jacobian matrices for 3-D problems tend to be large. In addition, the CPU time for the solution is large compared to other VII methods (in attached or mildly separated flows).

Chapter 7

Conclusions

7.1 FS Coupling for 3-D Flows

This thesis presented a Fully Simultaneous coupling method for three-dimensional flows. FS coupling is based on the premise that the inviscid and viscous equations together form a well-posed problem in attached and separated flows. The concept is straight-forward: define residual equations for the VII problem, and solve the set of non-linear equations simultaneously with a Newton method. The implementation, however, is rather involved.

The Full Potential equation is discretized with the Galerkin finite element method and the 3-D integral boundary layer equations are discretized with a Petrov-Galerkin finite element scheme. The displacement effect of the boundary layer is simulated with a wall transpiration boundary condition on the inviscid equations, and inviscid edge velocities communicate the pressure field to the boundary layer equations. Edge velocity smoothing must be present in separated flow to remove a nullspace which appears due to the discretization. At each iteration the solution to a large, sparse, non-symmetric, linear system is computed with GMRES and a drop-tolerance ILU preconditioner.

The algorithm was tested on the van den Berg/Elsenaar infinite swept wing, the RAE 2822 airfoil, a 45°-swept wing, the MBB-AVA wing, and the Boeing 747 wing. Good agreement between experimental data (C_p 's, BL thicknesses, C_L and C_D) and this VII method is demonstrated. Moreover, the Fully Simultaneous coupling method is able to handle three-dimensional separated flows. The main drawback with the FS coupling method is the large computer resource requirements for the solution of the Newton system.

7.2 FEM Discretization of the 3-D Integral BL Equations

This thesis also presented a second-order accurate finite element discretization of the 3-D integral boundary layer equations. The integral boundary layer equations are first cast in a Cartesian coordinate form and all $x-z$ boundary layer quantities are related to four primary nodal variables and the 3-D surface velocities. $x-z$ -variables are derived from 1-2 variables using vector identities; and 1-2 variables are related to the primary variables using streamwise closure relations and the Johnston triangular crossflow profile. Edge velocities are computed with simple dot product operations between the $x-z$ coordinate system and the 3-D surface velocities.

A weighted residual form of the 3-D BL equations is solved with the Petrov-Galerkin finite element method. Here, an upwinded weighting function is required for the numerical stability of these hyperbolic equations. The finite element method automatically produces natural boundary conditions which satisfy symmetry or infinite swept wing-like BC's, requires no explicit crossflow smoothing, and allows for the unstructured assemblage of the Jacobian matrix. This discretization of the 3-D integral boundary layer equations is independent of the coupling method and may be used in other VII methods.

7.3 Newton Method Solution

This thesis describes efficient bookkeeping processes for the sparse matrix assembly. After an "optimal" node numbering is determined, the equation numbers for each degree-of-freedom are stored in an identification array. Then, the identification array, the finite element connectivity, and a column skipping array are used to map the (i, j) locations of all the non-zeroes in the matrix. Once mapped, the indices are re-stored in a convenient column format and the matrix can be assembled.

The Jacobian matrix may be checked for proper linearization by testing for quadratic convergence and by pinging elemental sensitivities. All of these processes are general and can be used in other finite element Newton methods.

7.4 Recommendations for Future Work

7.4.1 Improvements in 3-D Boundary Layer Modeling

As discussed in Chapter 6, the kinematic shape parameter sometimes goes below unity on the wake. This is entirely non-physical and although a 2-D strip wake calculation may not noticeably affect the pressure field on the wing, it is important to have a full 3-D wake calculation for viscous drag estimation (see Appendix D) and for consistency.

The wingtip side boundary conditions provide another area for improvement. Currently the tip BC's are approximated using the solution to the 2-D boundary layer equations. The solutions near the tip were consistently in poor agreement with experimental data, and perhaps a better tip BC would improve these results. Alternative BC's should be formulated, and their stability should be checked with an eigensystem analysis. In addition, the physically correct BL variable *magnitudes* at the boundaries need to be determined (this is analogous to a farfield model).

7.4.2 Examination of Farfield Drag Formula

The farfield drag formula of Appendix D should provide drag calculations which are more accurate than the standard surface integration. Furthermore it is able to separate the drag into vortex, viscous and wave components. Because of the state of the wake calculation, however, the soundness of the farfield formula could not be determined. With a better wake calculation, a drag study with a series of finer meshes should be conducted.

7.4.3 Newton Method Speedup

The computation times for 3-D problems is large, and any speedup in the Newton method is desirable. One time saving technique is *grid sequencing*. The procedure is to solve the problem on an inexpensive coarse mesh, and then interpolate the solution to a finer mesh. Since this is a better initial solution, fewer Newton steps will be required on the fine mesh.

The process may be extended by using a sequence of meshes. In addition, any advances in the solution of large, sparse, non-symmetric systems would also be beneficial.

7.4.4 Viscous Design Work

The Newton System provides flowfield sensitivities which can be used in an inverse design method (see Poll [42] or Sorensen [52]) where the pressure is specified and the resulting wing shape is computed. The sensitivity of other relevant quantities like C_L , C_D , and C_M can also be determined. This opens up numerous possibilities for use in optimization methods.

Bibliography

- [1] D. J. Acheson. *Elementary Fluid Dynamics*. Oxford University Press, New York, NY, 1990.
- [2] D. A. Anderson, J. C. Tannehill, and R. H. Pletcher. *Computational Fluid Mechanics and Heat Transfer*. Hemisphere Publishing Corp., New York, NY, 1984.
- [3] J. D. Anderson Jr. *Fundamentals of Aerodynamics*. McGraw-Hill, New York, NY, 1984.
- [4] H. Ashley and M. Landahl. *Aerodynamics of Wings and Bodies*. Dover, New York, NY, 1965.
- [5] G. Batchelor. *An Introduction to Fluid Dynamics*. Cambridge University Press, New York, NY, 1980.
- [6] K. J. Bathe. *Finite Element Procedures in Engineering Analysis*. Prentice-Hall, Englewood Cliffs, NJ, 1982.
- [7] G. G. Brebner and L. A. Wyatt. *Boundary Layer Measurements at Low Speed on Two Wings of 45° and 55° Sweep*. CP 554, Aeronautical Research Council, 1961.
- [8] J. E. Bussoletti, F. T. Johnson, et al. “TRANAIR: Solution Adaptive CFD Modeling for Complex 3D Configurations.” In *Proceedings of the 1993 European Forum on Recent Developments and Applications in Aeronautical CFD*, pp. 10.1–10.14, 1994.
- [9] T. Cebeci, L. T. Chen, and K. C. Chang. “An Interactive Scheme for Three-Dimensional Transonic Flows.” In *Numerical and Physical Aspects of Aerodynamic Flows III*, Springer-Verlag, 1986.
- [10] P. H. Cook, M. A. McDonald, and M. C. P. Firmin. *Aerofoil RAE 2822-Pressure Distributions, and Boundary Layer and Wake Measurements*. Advisory Report 138, AGARD, May 1979.
- [11] J. Cousteix. *Three-Dimensional Boundary Layers. Introduction to Calculation Methods*. Advisory Report 741, AGARD, 1986.
- [12] N. A. Cumpsty and M. R. Head. “The Calculation of Three-Dimensional Turbulent Boundary Layers. Part II: Attachment-line Flow on an Infinite Swept Wing.” *The Aeronautical Quarterly*, 28:150–164, 1967.
- [13] D. Darmofal. Personal Communication.
- [14] H. Deconinck and C. Hirsch. “Finite Element Methods for Transonic Blade-to-Blade Calculation in Turbomachines.” *Journal of Engineering for Power*, 103:665–677, 1981.

- [15] M. Drela. *Two-Dimensional Transonic Aerodynamic Design and Analysis Using the Euler Equations*. GTL Report 187, MIT, February 1986.
- [16] M. Drela. Personal Communication.
- [17] J. K. Elliot. Personal Communication.
- [18] H. C. Elman. "A Stability Analysis of Incomplete LU Factorizations." *Mathematics of Computation*, 47(175):191–217, July 1986.
- [19] M. C. P. Firmin. *Applications of RAE Viscous Flow Methods Near Separation for Three-Dimensional Wings in Transonic Flow*. Technical Report CP-412, AGARD, 1986.
- [20] M. Giles. *Eigenmode Analysis of Unsteady One-dimensional Euler Equations*. Contractor Report NAS1-17130, ICASE, August 1983.
- [21] J. Green, D. Weeks, and J. Brooman. *Prediction of Turbulent Boundary Layer and Wakes in Compressible Flow by a Lag-Entrainment Method*. R & M 3791, Aeronautical Research Council, 1977.
- [22] W. G. Habashi and M. M. Hafez. *Finite Element Method for Transonic Cascade Flows*. AIAA-81-1472, 1981.
- [23] M. Hafez, J. South, and E. Murman. "Artificial Compressibility Methods for Numerical Solutions of Transonic Full Potential Equation." *AIAA Journal*, 17:838–844, August 1979.
- [24] W. W. Hager. *Applied Numerical Linear Algebra*. Prentice-Hall, Inc., Englewood Cliffs, NJ, 1988.
- [25] T. L. Holst. *Viscous Transonic Airfoil Workshop Compendium of Results*. AIAA-87-1460, June 1987.
- [26] R. Ito and S. Takanashi. *Validation of 3-D Navier-Stokes Simulations for Transonic Flows about Boeing 747-200 Wing-Fuselage Combination*. AIAA-91-3202, 1991.
- [27] C. Johnson. *Numerical Solutions of Partial Differential Equations by the Finite Element Method*. Cambridge University Press, New York, NY, 1987.
- [28] J. P. Johnston. *Three-dimensional Turbulent Boundary Layers*. PhD thesis, Gas Turbine Laboratory, MIT, 1957.
- [29] H. Körner, W. Lorenz-Meyer, et al. *MRB-AVA Pilot-Model with Supercritical Wing-Surface Pressure and Force Measurements*. Advisory Report 138, AGARD, May 1979.
- [30] V. E. Kovalev and O. V. Karas. "Computation of a Transonic Airfoil Flow Considering Viscous Effects and Thin Separated Regions." *Le Recherche Aérospatiale*, 1991(1):1–15, 1991.
- [31] M. Lazareff and J. C. L. Balleur. "Development of the MZM Numerical Method for 3D Boundary Layer with Interaction on Complex Configurations." In *Proceedings of the Eighth GAMM-Conference on Numerical Methods in Fluid Mechanics*, 1989. Notes on Numerical Fluid Mechanics, vol 29.

- [32] J. C. Le Balleur. "New Possibilities of Viscous-Inviscid Numerical Techniques for Solving Viscous Flow Equations with Massive Separation." In *4th Symposium on Numerical and Physical Aspects of Aerodynamic Flows*, January 1989.
- [33] M. J. Lighthill. "On Displacement Thickness." *Journal of Fluid Mechanics*, 4:383–392, 1958.
- [34] R. C. Lock and B. R. Williams. "Viscous-Inviscid Interactions in External Aerodynamics." *Prog. Aerospace Sci.*, 24:51–171, 1987.
- [35] J. D. McLean and J. L. Randall. *Computer Program to Calculate Three-Dimensional Boundary Layer Flows with Wall Mass Transfer*. CR 3123, NASA, May 1979.
- [36] J. Moran. *An Introduction to Theoretical and Computational Aerodynamics*. John Wiley & Sons, New York, NY, 1984.
- [37] B. Mughal. Personal Communication.
- [38] B. H. Mughal. *A Calculation Method for the Three-Dimensional Boundary-Layer Equations in Integral Form*. Master's thesis, Dept. of Aeronautics and Astronautics, MIT, September 1992.
- [39] D. F. Myring. *An Integral Prediction Method for Three-Dimensional Turbulent Boundary Layers in Incompressible Flow*. Technical Report 32647, Aeronautical Research Council, 1970.
- [40] J. F. Nash and V. C. Patel. *Three-Dimensional Turbulent Boundary Layers*. SBC Technical Books, Atlanta, 1972.
- [41] J. Peraire and J. Peiro. *A 3D Finite Element Multigrid Solver for the Euler Equations*. AIAA Paper 92-0449, January 1992.
- [42] P. B. Poll. *Full Potential Analysis and Design of Transonic Propellers*. Master's thesis, Dept. of Aeronautics and Astronautics, MIT, February 1991.
- [43] W. H. Press, B. P. Flannery, S. A. Teukolsky, and W. T. Vetterling. *Numerical Recipes, The Art of Scientific Computing*. Cambridge University Press, New York, NY, 1986.
- [44] Y. Saad and M. H. Schultz. "GMRES: A Generalized Minimal Residual Algorithm for Solving Nonsymmetric Linear Systems." *SIAM J. Sci. Stat. Comput.*, 7(3):856–869, July 1986.
- [45] M. D. Salas and C. R. Gumbert. *Breakdown of the Conservative Potential Equation*. Technical Paper 2539, NASA, 1986.
- [46] M. D. Salas, A. Jameson, and R. E. Melnik. *A Comparative Study of the Nonuniqueness Problem of the Potential Equation*. Technical Paper 2385, NASA, 1985.
- [47] H. Schlichting. *Boundary Layer Theory*. McGraw-Hill, New York, 7th ed. edition, 1987.
- [48] M. K. Seager. *A SLAP for the Masses*. UCRL 100195, Lawrence Livermore Labs, December 1988.

- [49] P. D. Smith. *An Integral Prediction Method for Three-Dimensional Compressible Turbulent Boundary Layers*. R & M 3739, Aeronautical Research Council, 1972.
- [50] S. C. Smith and I. M. Kroo. "Computation of Induced Drag for Elliptical and Crescent-Shaped Wings." *Journal of Aircraft*, 30:446–452, July/August 1993.
- [51] T. Sorensen. Personal Communication.
- [52] T. Sorensen. *Aeroelastic Analysis and Sensitivity Calculations Using the Newton Method*. PhD thesis, Dept. of Aeronautics and Astronautics, MIT, June 1995.
- [53] T. W. Swafford and D. L. Whitfield. "Time-Dependent Solution of Three-Dimensional Compressible Turbulent Integral Boundary-Layer Equations." *AIAA Journal*, 23(7):1005–1013, July 1985.
- [54] T. Swafford. "Analytical Approximation of Two-Dimensional Separated Turbulent Boundary-Layer Velocity Profiles." *AIAA Journal*, 21(6):923–926, June 1983.
- [55] J. Thompson, F. Thames, and C. Mastin. "Automatic Numerical Generation of Body-Fitted Curvilinear Coordinate System for Field Containing Any Number of Arbitrary Two-Dimensional Bodies." *Journal of Computational Physics*, 15:299–319, 1974.
- [56] B. van den Berg and A. Elsenaar. *Measurements in a Three-Dimensional Incompressible Turbulent Boundary Layer in an Adverse Pressure Gradient Under Infinite Swept Wing Conditions*. Technical Report NLR TR 72092 U, National Aerospace Laboratory NLR, August 1972.
- [57] B. van den Berg, D. A. Humphreys, E. Krause, and J. P. F. Lindhout, editors. *Three-Dimensional Turbulent Boundary Layers—Calculations and Experiments*. Vol. 19 of *Notes on Numerical Fluid Mechanics*, Vieweg, Braunschweig, 1988.
- [58] J. van der Vooren. *Aircraft Drag Prediction for Transonic Potential Flows*. Advisory Report 256, AGARD, 1989.
- [59] K. C. Wang. "On the Determination of the Zones of Influence and Dependence for Three-Dimensional Boundary Layer Equations." *Journal of Fluid Mechanics*, 48:397–404, 1971.
- [60] J. Weber and G. G. Brebner. *Low-Speed Tests on 45-deg Swept-back Wings*. R & M 2822, Aeronautical Research Council, 1958.
- [61] F. M. White. *Viscous Fluid Flow*. McGraw-Hill, New York, NY, 2nd ed. edition, 1991.
- [62] D. Whitfield. *Analytical Description of the Complete Turbulent Boundary Layer Velocity Profile*. AIAA-81-1158, 1978.
- [63] D. Whitfield, T. Swafford, and T. Donnegan. "An Inverse Integral Computational Method for Compressible Turbulent Boundary Layers." In *Recent Contributions to Fluid Mechanics*, Springer-Verlag, 1982.
- [64] L. B. Wigton and M. Holt. *Viscous-Inviscid Interaction in Transonic Flow*. AIAA-81-1003, 1981.

- [65] H. Yoshihara and J. Wai. *Transonic Turbulent Separation on Swept Wings-A Return to the Direct Formulation*. AIAA-84-0265, 1984.
- [66] D. P. Young, R. G. Melvin, F. T. Johnson, et al. "Application of Sparse Matrix Solvers as Effective Preconditioners." *SIAM J. Sci. Stat. Comput.*, 10(6):1186–1199, November 1989.
- [67] N. J. Yu, H. C. Chen, S. S. Samant, and P. E. Rubbert. *Inviscid Drag Calculations for Transonic Flows*. AIAA Paper 83-1928, 1983.
- [68] N. J. Yu, S. R. Allmaras, and K. G. Moschetti. *Navier-Stokes Calculations for Attached and Separated Flows Using Different Turbulence Models*. AIAA-91-1791, 1991.

Appendix A

Finite Element Method for the Full Potential Equation

This appendix gives more details of the Finite Element Method (FEM) applied to the Full Potential equation. A good reference for FEM implementation is [6], and one for FEM theory is [27]. The second part of this appendix provides the sensitivity formulae for the Full Potential equation.

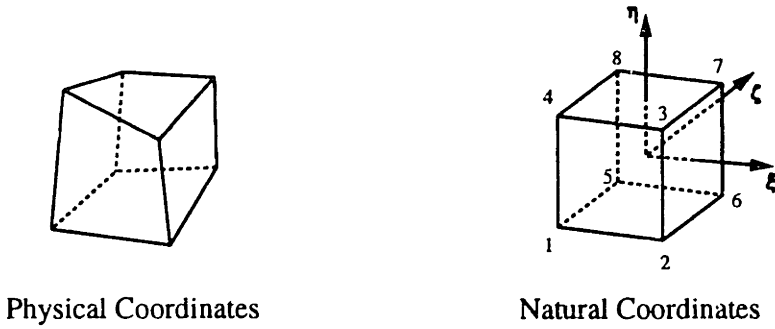


Figure A.1: Hexahedral Elements

A.1 FEM Details

A.1.1 Isoparametric Trilinear Elements

Within an element, the solution ϕ and the geometry (x, y, z) are expressed in terms of local basis or shape functions. For the 8-node trilinear element illustrated in Figure A.1, the eight functions expressed in *natural* coordinates (ξ, η, ζ) are:

$$N_1^e = \frac{1}{8} (1 - \xi) (1 - \eta) (1 - \zeta) \quad N_5^e = \frac{1}{8} (1 - \xi) (1 - \eta) (1 + \zeta)$$

$$N_2^e = \frac{1}{8} (1 + \xi) (1 - \eta) (1 - \zeta) \quad N_6^e = \frac{1}{8} (1 + \xi) (1 - \eta) (1 + \zeta)$$

$$N_3^e = \frac{1}{8} (1 + \xi) (1 + \eta) (1 - \zeta) \quad N_7^e = \frac{1}{8} (1 + \xi) (1 + \eta) (1 + \zeta)$$

$$N_4^e = \frac{1}{8} (1 - \xi) (1 + \eta) (1 - \zeta) \quad N_8^e = \frac{1}{8} (1 - \xi) (1 + \eta) (1 + \zeta)$$

and the solution and geometry within the element are defined as:

$$\phi^e = \sum_{j=1}^8 N_j^e \phi_j^e \quad x^e = \sum_{j=1}^8 N_j^e x_j^e \quad y^e = \sum_{j=1}^8 N_j^e y_j^e \quad z^e = \sum_{j=1}^8 N_j^e z_j^e$$

where $\phi_j^e, x_j^e, y_j^e, z_j^e$ are nodal solution values and coordinates for element e .

A.1.2 Shape Function Gradients

Residuals require the gradient of the shape function, ∇N_i^e . For a given point (ξ, η, ζ) , the gradient in *natural* coordinates is computed via:

$$\begin{aligned} \frac{\partial N_j^e}{\partial \xi} &= \pm \frac{1}{8} (1 \pm \eta) (1 \pm \zeta) \\ \frac{\partial N_j^e}{\partial \eta} &= \pm \frac{1}{8} (1 \pm \xi) (1 \pm \zeta) \\ \frac{\partial N_j^e}{\partial \zeta} &= \pm \frac{1}{8} (1 \pm \xi) (1 \pm \eta) \end{aligned} \tag{A.1}$$

Then, the gradients of x, y, z with respect to ξ, η, ζ may be computed from:

$$\begin{aligned}
\frac{\partial x}{\partial \xi} &= \sum_{j=1}^8 \frac{\partial N_j^\epsilon}{\partial \xi} x_j^\epsilon & \frac{\partial y}{\partial \xi} &= \sum_{j=1}^8 \frac{\partial N_j^\epsilon}{\partial \xi} y_j^\epsilon & \frac{\partial z}{\partial \xi} &= \sum_{j=1}^8 \frac{\partial N_j^\epsilon}{\partial \xi} z_j^\epsilon \\
\frac{\partial x}{\partial \eta} &= \sum_{j=1}^8 \frac{\partial N_j^\epsilon}{\partial \eta} x_j^\epsilon & \frac{\partial y}{\partial \eta} &= \sum_{j=1}^8 \frac{\partial N_j^\epsilon}{\partial \eta} y_j^\epsilon & \frac{\partial z}{\partial \eta} &= \sum_{j=1}^8 \frac{\partial N_j^\epsilon}{\partial \eta} z_j^\epsilon \\
\frac{\partial x}{\partial \zeta} &= \sum_{j=1}^8 \frac{\partial N_j^\epsilon}{\partial \zeta} x_j^\epsilon & \frac{\partial y}{\partial \zeta} &= \sum_{j=1}^8 \frac{\partial N_j^\epsilon}{\partial \zeta} y_j^\epsilon & \frac{\partial z}{\partial \zeta} &= \sum_{j=1}^8 \frac{\partial N_j^\epsilon}{\partial \zeta} z_j^\epsilon
\end{aligned} \tag{A.2}$$

Using the chain rule to define the gradient of the shape function in natural coordinates, one arrives at the following system of equations:

$$\begin{pmatrix} \frac{\partial x}{\partial \xi} & \frac{\partial y}{\partial \xi} & \frac{\partial z}{\partial \xi} \\ \frac{\partial x}{\partial \eta} & \frac{\partial y}{\partial \eta} & \frac{\partial z}{\partial \eta} \\ \frac{\partial x}{\partial \zeta} & \frac{\partial y}{\partial \zeta} & \frac{\partial z}{\partial \zeta} \end{pmatrix} \begin{pmatrix} \frac{\partial N}{\partial x} \\ \frac{\partial N}{\partial y} \\ \frac{\partial N}{\partial z} \end{pmatrix} = \begin{pmatrix} \frac{\partial N}{\partial \xi} \\ \frac{\partial N}{\partial \eta} \\ \frac{\partial N}{\partial \zeta} \end{pmatrix} \tag{A.3}$$

which may be solved for the gradient of the shape function in physical coordinates $\nabla N = \left(\frac{\partial N}{\partial x}, \frac{\partial N}{\partial y}, \frac{\partial N}{\partial z} \right)$. The determinant of the matrix is the so-called metric Jacobian.

A.1.3 Surface Gradients

Gradients at element surfaces are also required. In the case of Equation 2.15, the (ξ, η, ζ) coordinate corresponding to a surface of the element is computed, and then the method of §A.1.2 is employed.

For surface equations such as Equation 3.11, each element is given a local 2-D coordinate system. This is done by computing a surface normal vector (\hat{e}_n) to the element using the cross product of the diagonals:

Then an x - z coordinate system is set up using one diagonal for the x -direction (\hat{e}_x) and

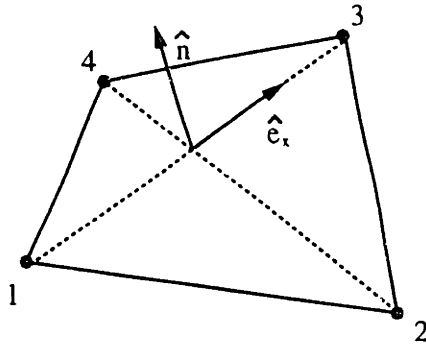


Figure A.2: Construction of 2-D Coordinate System

the normal to \hat{e}_x and \hat{e}_n for the z -direction (\hat{e}_z); where \hat{e}_x , \hat{e}_z , and \hat{e}_n are 3-D vectors. (x, z) coordinates for the four surface nodes may be computed from the $(x, y, z)_{Cartesian}$ coordinates using dot products between the vector distances and \hat{e}_x and \hat{e}_z . For instance, if node 1 is set to $(x, z) = (0, 0)$ in the 2-D coordinate system. Then the coordinates for node 2 may be found by:

$$\Delta x = (x_2)_{Cartesian} - (x_1)_{Cartesian}$$

$$\Delta y = (y_2)_{Cartesian} - (y_1)_{Cartesian}$$

$$\Delta z = (z_2)_{Cartesian} - (z_1)_{Cartesian}$$

$$\vec{\Delta} = \Delta x \hat{i} + \Delta y \hat{j} + \Delta z \hat{k}$$

$$x_2 = x_1 + \vec{\Delta} \cdot \hat{e}_x$$

$$z_2 = z_1 + \vec{\Delta} \cdot \hat{e}_z$$

A 2-D analog of §A.1.2 is employed to compute surface gradients for Equations 3.11, 3.12, and 3.13.

A.2 Full Potential Equation Sensitivities

Flowfield sensitivities for the Full Potential equation were derived by Poll in reference [42]. These sensitivities are listed here for completeness.

A.2.1 Velocity Vector

$$\begin{aligned}\vec{q} &= \left(u_{\infty} + \sum_{j=1}^8 \frac{\partial N_j}{\partial x} \phi_j \right) \hat{i} + \left(v_{\infty} + \sum_{j=1}^8 \frac{\partial N_j}{\partial y} \phi_j \right) \hat{j} + \left(w_{\infty} + \sum_{j=1}^8 \frac{\partial N_j}{\partial z} \phi_j \right) \hat{k} \\ \frac{\partial \vec{q}}{\partial \phi_j} &= \frac{\partial N_j}{\partial x} \hat{i} + \frac{\partial N_j}{\partial y} \hat{j} + \frac{\partial N_j}{\partial z} \hat{k} \\ \frac{\partial \vec{q}}{\partial \alpha} &= \frac{\partial u_{\infty}}{\partial \alpha} \hat{i} + \frac{\partial v_{\infty}}{\partial \alpha} \hat{j} + \frac{\partial w_{\infty}}{\partial \alpha} \hat{k}\end{aligned}$$

A.2.2 Velocity Squared

$$\begin{aligned}q^2 &= u^2 + v^2 + w^2 \\ &= \left(u_{\infty} + \sum_{j=1}^8 \frac{\partial N_j}{\partial x} \phi_j \right)^2 + \left(v_{\infty} + \sum_{j=1}^8 \frac{\partial N_j}{\partial y} \phi_j \right)^2 + \left(w_{\infty} + \sum_{j=1}^8 \frac{\partial N_j}{\partial z} \phi_j \right)^2 \\ \frac{\partial q^2}{\partial \phi_j} &= 2 \left(u \frac{\partial N_j}{\partial x} + v \frac{\partial N_j}{\partial y} + w \frac{\partial N_j}{\partial z} \right) \\ \frac{\partial q^2}{\partial \alpha} &= 2 \left(u \frac{\partial u_{\infty}}{\partial \alpha} + v \frac{\partial v_{\infty}}{\partial \alpha} + w \frac{\partial w_{\infty}}{\partial \alpha} \right)\end{aligned}$$

A.2.3 Mach Number

$$M^2 = M_{\infty}^2 \frac{q^2}{q_{\infty}^2} \left[1 + \frac{\gamma - 1}{2} M_{\infty}^2 \left(1 - \frac{q^2}{q_{\infty}^2} \right) \right]^{-1}$$

$$\frac{\partial M^2}{\partial q^2} = M^2 \left\{ \frac{1}{q^2} + \frac{\gamma - 1}{2} M_\infty^2 \frac{1}{q_\infty^2} \left[1 + \frac{\gamma - 1}{2} M_\infty^2 \left(1 - \frac{q^2}{q_\infty^2} \right) \right]^{-1} \right\}$$

$$\frac{\partial M^2}{\partial \phi} = \frac{\partial M^2}{\partial q^2} \frac{\partial q^2}{\partial \phi} \quad \frac{\partial M^2}{\partial \alpha} = \frac{\partial M^2}{\partial q^2} \frac{\partial q^2}{\partial \alpha}$$

A.2.4 Upwinding Factor

$$\mu_f = \mu_c \max \left\{ 0, \left(1 - \frac{M_{crit}^2}{M^2} \right), \left(1 - \frac{M_{crit}^2}{M_{up}^2} \right) \right\} = \mu_c \max \{ 0, \mu, \mu_{up} \}$$

$$\frac{\partial \mu}{\partial M^2} = -\mu_c \frac{M_{crit}^2}{M^4} \quad \frac{\partial \mu_{up}}{\partial M_{up}^2} = -\mu_c \frac{M_{crit}^2}{M_{up}^4}$$

$$\frac{\partial \mu}{\partial q^2} = \frac{\partial \mu}{\partial M^2} \frac{\partial M^2}{\partial q^2} \quad \frac{\partial \mu_{up}}{\partial q_{up}^2} = \frac{\partial \mu_{up}}{\partial M_{up}^2} \frac{\partial M_{up}^2}{\partial q_{up}^2}$$

$$\frac{\partial \mu}{\partial \alpha} = \frac{\partial \mu}{\partial M^2} \frac{\partial M^2}{\partial \alpha} \quad \frac{\partial \mu_{up}}{\partial \alpha} = \frac{\partial \mu_{up}}{\partial M_{up}^2} \frac{\partial M_{up}^2}{\partial \alpha}$$

A.2.5 Density

$$\rho = \rho_\infty \left[1 + \frac{\gamma - 1}{2} M_\infty^2 \left(1 - \frac{q^2}{q_\infty^2} \right) \right]^{\frac{1}{\gamma - 1}}$$

$$\frac{\partial \rho}{\partial q^2} = -\frac{\rho_\infty M_\infty^2}{2q_\infty^2} \left[1 + \frac{\gamma - 1}{2} M_\infty^2 \left(1 - \frac{q^2}{q_\infty^2} \right) \right]^{\frac{2-\gamma}{\gamma-1}}$$

$$\frac{\partial \rho}{\partial \phi_j} = \frac{\partial \rho}{\partial q^2} \frac{\partial q^2}{\partial \phi_j} \quad \frac{\partial \rho}{\partial \alpha} = \frac{\partial \rho}{\partial q^2} \frac{\partial q^2}{\partial \alpha}$$

A.2.6 Upwinded Density

$$\tilde{\rho} = \rho - \mu_f (\rho - \rho_{up})$$

$\phi_{j_{up}}$ refers to nodal ϕ 's in the upwind element.

Case 1: Flow is subsonic

$$\frac{\partial \tilde{\rho}}{\partial \phi_j} = \frac{\partial \rho}{\partial \phi_j}$$

$$\frac{\partial \tilde{\rho}}{\partial \phi_{j_{up}}} = 0$$

$$\frac{\partial \tilde{\rho}}{\partial \alpha} = \frac{\partial \rho}{\partial \alpha}$$

Case 2: Flow is supersonic and accelerating ($M^2 > M_{up}^2$)

$$\frac{\partial \tilde{\rho}}{\partial \phi_j} = \frac{\partial \rho}{\partial \phi_j} - \left[\frac{\partial \mu}{\partial \phi_j} (\rho - \rho_{up}) + \mu \frac{\partial \rho}{\partial \phi_j} \right]$$

$$\frac{\partial \tilde{\rho}}{\partial \phi_{j_{up}}} = 0 - \left[-\mu \frac{\partial \rho_{up}}{\partial \phi_{j_{up}}} \right]$$

$$\frac{\partial \tilde{\rho}}{\partial \alpha} = \frac{\partial \rho}{\partial \alpha} - \left[\frac{\partial \mu}{\partial \alpha} (\rho - \rho_{up}) - \mu \frac{\partial \rho_{up}}{\partial \alpha} \right]$$

Case 3: Flow is supersonic and decelerating ($M^2 < M_{up}^2$)

$$\frac{\partial \tilde{\rho}}{\partial \phi_j} = \frac{\partial \rho}{\partial \phi_j} - \left[+ \mu_{up} \frac{\partial \rho}{\partial \phi_j} \right]$$

$$\frac{\partial \tilde{\rho}}{\partial \phi_{j_{up}}} = 0 - \left[\frac{\partial \mu_{up}}{\partial \phi_{j_{up}}} (\rho - \rho_{up}) - \mu_{up} \frac{\partial \rho_{up}}{\partial \phi_{j_{up}}} \right]$$

$$\frac{\partial \tilde{\rho}}{\partial \alpha} = \frac{\partial \rho}{\partial \alpha} - \left[\frac{\partial \mu_{up}}{\partial \alpha} (\rho - \rho_{up}) - \mu_{up} \frac{\partial \rho_{up}}{\partial \alpha} \right]$$

A.2.7 Full Potential Residual

With the relations in the previous sections, the Full Potential equation residual sensitivities may be computed. In reference [42], the density was assumed constant in the element and

taken outside of the integrals. This produced erroneous shock positions for coarse grids because it is an inconsistent formulation. In this research, the density is included in the integrals.

$$R_i = \iiint_V \nabla N_i \cdot (\tilde{\rho} \vec{q}) \, dV - \iint_{S_{\partial\Omega}} N_i (\tilde{\rho} \vec{q}) \cdot \hat{n} \, dS$$

$$\frac{\partial R_i}{\partial \phi_j} = \iiint_V \nabla N_i \left(\tilde{\rho} \frac{\partial \vec{q}}{\partial \phi_j} + \vec{q} \frac{\partial \tilde{\rho}}{\partial \phi_j} \right) \, dV - \iint_{S_{\partial\Omega}} N_i \left(\tilde{\rho} \frac{\partial \vec{q}}{\partial \phi_j} + \vec{q} \frac{\partial \tilde{\rho}}{\partial \phi_j} \right) \cdot \hat{n} \, dS$$

$$\frac{\partial R_i}{\partial \alpha} = \iiint_V \nabla N_i \left(\tilde{\rho} \frac{\partial \vec{q}}{\partial \alpha} + \vec{q} \frac{\partial \tilde{\rho}}{\partial \alpha} \right) \, dV - \iint_{S_{\partial\Omega}} N_i \left(\tilde{\rho} \frac{\partial \vec{q}}{\partial \alpha} + \vec{q} \frac{\partial \tilde{\rho}}{\partial \alpha} \right) \cdot \hat{n} \, dS$$

A.2.8 Wake B.C.

The second wake boundary condition (velocity matching on upper and lower surfaces) has the following sensitivities:

$$(R_{wake})_i = \iiint_V W_i (q_{up}^2 - q_{lo}^2) \, dV$$

$$\frac{\partial}{\partial \phi_j} (R_{wake})_i = \iiint_V W_i \left(\frac{\partial q_{up}^2}{\partial \phi_j} - \frac{\partial q_{lo}^2}{\partial \phi_j} \right) \, dV$$

$$\frac{\partial}{\partial \alpha} (R_{wake})_i = \iiint_V W_i \left(\frac{\partial q_{up}^2}{\partial \alpha} - \frac{\partial q_{lo}^2}{\partial \alpha} \right) \, dV$$

Appendix B

Closure for Three-Dimensional Boundary Layer Equations

B.1 1-2 Coordinate Definitions

1 \implies Streamwise Direction

2 \implies Crossflow Direction

$$\theta_{11} = \int \left(1 - \frac{u_1}{q_e}\right) \frac{\rho}{\rho_e} \frac{u_1}{q_e} d\eta \quad \theta_{12} = \int \left(1 - \frac{u_1}{q_e}\right) \frac{\rho}{\rho_e} \frac{u_2}{q_e} d\eta$$

$$\theta_{21} = \int \left(-\frac{u_2}{q_e}\right) \frac{\rho}{\rho_e} \frac{u_1}{q_e} d\eta \quad \theta_{22} = \int \left(-\frac{u_2}{q_e}\right) \frac{\rho}{\rho_e} \frac{u_2}{q_e} d\eta$$

$$\delta_1^* = \int 1 - \frac{\rho}{\rho_e} \frac{u_1}{q_e} d\eta \quad \delta_2^* = \int -\frac{\rho}{\rho_e} \frac{u_2}{q_e} d\eta$$

$$\theta_\rho = \int 1 - \frac{\rho}{\rho_e} d\eta$$

$$\delta_1^{**} = \int \left(1 - \frac{\rho}{\rho_e}\right) \frac{u_1}{q_e} d\eta \quad \delta_2^{**} = \int \left(1 - \frac{\rho}{\rho_e}\right) \frac{u_2}{q_e} d\eta$$

$$E_{11} = \int \left[1 - \left(\frac{u_1}{q_e}\right)^2\right] \frac{\rho}{\rho_e} \frac{u_1}{q_e} d\eta \quad E_{12} = \int \left[1 - \left(\frac{u_1}{q_e}\right)^2\right] \frac{\rho}{\rho_e} \frac{u_2}{q_e} d\eta$$

$$E_{21} = \int -\left(\frac{u_2}{q_e}\right)^2 \frac{\rho}{\rho_e} \frac{u_1}{q_e} d\eta \quad E_{22} = \int -\left(\frac{u_2}{q_e}\right)^2 \frac{\rho}{\rho_e} \frac{u_2}{q_e} d\eta$$

$$\theta_1^* = E_{11} + E_{21}$$

$$\theta_2^* = E_{12} + E_{22}$$

B.2 x - z Coordinate Definitions

Using a rotation matrix, the x - z thicknesses may be determined in terms of the 1-2 thicknesses and the angle between the two coordinate systems ($\cos \alpha = \frac{u_e}{q_e}$, $\sin \alpha = \frac{w_e}{q_e}$) [38, 49].

$$\begin{aligned}\rho_e q_e^2 \theta_{xx} &= \rho_e u_e^2 \theta_{11} + \rho_e w_e^2 \theta_{22} \\ &\quad - \rho_e u_e w_e (\theta_{12} + \theta_{21})\end{aligned}\quad \begin{aligned}\rho_e q_e^2 \theta_{zz} &= \rho_e u_e^2 \theta_{12} - \rho_e w_e^2 \theta_{21} \\ &\quad + \rho_e u_e w_e (\theta_{11} - \theta_{22})\end{aligned}$$

$$\begin{aligned}\rho_e q_e^2 \theta_{zx} &= \rho_e u_e^2 \theta_{21} - \rho_e w_e^2 \theta_{12} \\ &\quad + \rho_e u_e w_e (\theta_{11} - \theta_{22})\end{aligned}\quad \begin{aligned}\rho_e q_e^2 \theta_{xz} &= \rho_e u_e^2 \theta_{22} + \rho_e w_e^2 \theta_{11} \\ &\quad + \rho_e u_e w_e (\theta_{12} + \theta_{21})\end{aligned}$$

$$\begin{aligned}\rho_e q_e \delta_x^* &= \rho_e u_e \delta_1^* - \rho_e w_e \delta_2^* \\ \rho_e q_e^2 \delta_x^{**} &= \rho_e u_e \delta_1^{**} - \rho_e w_e \delta_2^{**}\end{aligned}\quad \begin{aligned}\rho_e q_e \delta_z^* &= \rho_e u_e \delta_2^* + \rho_e w_e \delta_1^* \\ \rho_e q_e^2 \delta_z^{**} &= \rho_e u_e \delta_2^{**} + \rho_e w_e \delta_1^{**}\end{aligned}$$

$$\rho_e q_e^3 \theta_x^* = q_e^2 (\rho_e u_e \theta_1^* - \rho_e w_e \theta_2^*) \quad \rho_e q_e^3 \theta_z^* = q_e^2 (\rho_e u_e \theta_2^* + \rho_e w_e \theta_1^*)$$

$$\tau_{zw} = \frac{u_e}{q_e} \tau_1 - \frac{w_e}{q_e} \tau_2 \quad \tau_{zw} = \frac{u_e}{q_e} \tau_2 + \frac{w_e}{q_e} \tau_1$$

$$D = \int \tau_1 du_1 + \int \tau_2 du_2$$

B.3 Crossflow Model

The crossflow model is Johnston's triangular profile [28]

$$\frac{u_2}{q_e} = A_c \left(1 - \frac{u_1}{q_e} \right) \quad (\text{B.1})$$

where A_c is the crossflow parameter. Streamwise-crossflow thicknesses may now be defined.

B.4 Derived Thicknesses

$$\begin{aligned}
\delta_2^* &= \int -\frac{\rho}{\rho_e} \frac{u_2}{q_e} d\eta \\
&= \int -A_c \left(1 - \frac{u_1}{q_e} \right) \frac{\rho}{\rho_e} d\eta \\
&= \int -A_c \left(1 - \frac{\rho}{\rho_e} \frac{u_1}{q_e} \right) d\eta + \int A_c \left(1 - \frac{\rho}{\rho_e} \right) d\eta \\
&= A_c (\theta_\rho - \delta_1^*)
\end{aligned} \tag{B.2}$$

$$A_c = \frac{\delta_2^*}{\theta_{11}} \frac{1}{H_{\theta_\rho} - H} \tag{B.3}$$

$$\begin{aligned}
\theta_{21} &= \int -\frac{u_2}{q_e} \frac{\rho}{\rho_e} \frac{u_1}{q_e} d\eta \\
&= \int -A_c \left(1 - \frac{u_1}{q_e} \right) \frac{\rho}{\rho_e} \frac{u_1}{q_e} d\eta \\
&= -A_c \theta_{11}
\end{aligned} \tag{B.4}$$

$$\begin{aligned}
\theta_{12} &= \int \left(1 - \frac{u_1}{q_e} \right) \frac{\rho}{\rho_e} \frac{u_2}{q_e} d\eta \\
&= \int -\frac{u_2}{q_e} \frac{\rho}{\rho_e} \frac{u_1}{q_e} d\eta + \int \frac{\rho}{\rho_e} \frac{u_2}{q_e} d\eta \\
&= \theta_{21} - \delta_2^*
\end{aligned} \tag{B.5}$$

$$\begin{aligned}
\theta_{22} &= \int -\frac{u_2}{q_e} \frac{\rho}{\rho_e} \frac{u_2}{q_e} d\eta \\
&= \int -A_c \left(1 - \frac{u_1}{q_e} \right) \frac{\rho}{\rho_e} \frac{u_2}{q_e} d\eta \\
&= -A_c \theta_{12}
\end{aligned} \tag{B.6}$$

$$\begin{aligned}
\delta_2^{**} &= \int \left(1 - \frac{\rho}{\rho_e}\right) \frac{u_2}{q_e} d\eta \\
&= \int \left(1 - \frac{\rho}{\rho_e}\right) A_c \left(1 - \frac{u_1}{q_e}\right) d\eta \\
&= A_c [\theta_\rho - \delta_1^{**}]
\end{aligned} \tag{B.7}$$

$$E_{12} = \theta_{12} + A_c (2\theta_{11} - E_{11}) \tag{B.8}$$

$$E_{21} = -\theta_{22} - A_c E_{12} \tag{B.9}$$

$$E_{22} = -A_c (E_{21} - \theta_{22}) \tag{B.10}$$

B.5 Empirical Closure Relations

The following closure relations are taken from subroutines of Drela. The references for these relations are labeled along with the formula.

Shape Parameters

$$\begin{aligned}
H &\equiv \frac{\delta_1^*}{\theta_{11}} \\
H_{\theta_\rho} &\equiv \frac{\theta_\rho}{\theta_{11}} \\
H_{\delta_{11}^{**}} &\equiv \frac{\delta_{11}^{**}}{\theta_{11}} \\
H^* &\equiv \frac{E_{11}}{\theta_{11}}
\end{aligned} \tag{B.11}$$

Kinematic Shape Parameter [62]

$$H_k = \frac{H - 0.290M^2}{1.0 + 0.113M^2} \quad (\text{B.12})$$

Density Shape Parameter [63]

$$H_{\delta_{11}^{**}} = \left(\frac{0.064}{H_k - 0.8} + 0.251 \right) M^2 \quad (\text{B.13})$$

Auxiliary Density Shape Factor [53]

$$H_{\theta_\rho} = (0.185H_k + 0.150)M^2 \quad (\text{B.14})$$

Streamwise Kinetic Energy Shape Parameter

laminar [16]

$$\begin{aligned} H^* &= 0.0111 \frac{(H_k - 4.35)^2}{H_k + 1.0} - 0.0278 \frac{(H_k - 4.35)^3}{H_k + 1.0} \\ &\quad + 1.528 - 0.0002 [(H_k - 4.35) H_k]^2 \quad H_k < 4.35 \\ H^* &= 0.015 \frac{(H_k - 4.35)^2}{H_k} + 1.528 \quad H_k \geq 4.35 \end{aligned} \quad (\text{B.15})$$

turbulent [15, 16]

$$\begin{aligned}
 H_o &= \min \left(3.0 + \frac{400.0}{Re_\theta}, 4.0 \right) \\
 H_r &= \frac{H_o - H_k}{H_o - 1.0} \\
 H_k^* &= \left(0.5 - \frac{4.0}{Re_\theta} \right) H_r^2 \frac{1.5}{H_k + 0.5} + 1.5 + \frac{4.0}{Re_\theta} & H_k < H_o \\
 H_k^* &= (H_k - H_o)^2 \left[0.007 \frac{\log(Re_\theta)}{(H_k - H_o + \frac{4.0}{\log(Re_\theta)})} + \frac{0.015}{H_k} \right] & (B.16) \\
 &+ 1.5 + \frac{4.0}{Re_\theta} & H_k \geq H_o \\
 H^* &= \frac{H_k^* + 0.028M^2}{1.0 + 0.014M^2}
 \end{aligned}$$

Boundary Layer Thickness Estimate for Lag Equation [16]

$$\delta = \left(3.15 + \frac{1.72}{H_k - 1.0} \right) \theta_{11} + \delta_1^* \quad (B.17)$$

Equilibrium Slip or Stress Coefficient [16]

$$\begin{aligned}
 C_o &= \frac{0.5}{6.7^2 + 0.75} \\
 U_s &= 0.5H^* \left(1.0 - \frac{H_k - 1.0}{0.75H} \right) & \text{streamwise slip velocity} \\
 C_\tau^{1/2}_{eq} &= \sqrt{\frac{C_o H^* (H_k - 1.0)^3}{(1.0 - U_s) (1.0 + A_c^2) H H_k^2}} & (B.18)
 \end{aligned}$$

Streamwise Skin Friction

laminar [15]

$$C_{f_1} = \frac{1}{Re_\theta} \left\{ 0.0727 \frac{(5.5 - H_k)^3}{H_k + 1.0} - 0.07 \right\} \quad H_k < 5.5$$

$$C_{f_1} = \frac{1}{Re_\theta} \left\{ 0.015 \left(1.0 - \frac{1.0}{H_k - 4.5} \right)^2 - 0.07 \right\} \quad H_k \geq 5.5 \quad (\text{B.19})$$

turbulent [54]

$$F_c = \sqrt{1.0 + \frac{\gamma - 1}{2} M^2}$$

$$C_{f_0} = 0.3 \exp(-1.33 H_k) \left(\frac{\log \left(\frac{Re_\theta}{F_c} \right)}{2.3026} \right)^{-1.74 - 0.31 H_k} \quad (\text{B.20})$$

$$C_{f_1} = \frac{1}{F_c} \left\{ C_{f_0} + 1.1 \times 10^{-4} \left[\tanh \left(4.0 - \frac{H_k}{0.875} \right) - 1.0 \right] \right\}$$

Crossflow Skin Friction

laminar [16]

$$C_{f_2} = -0.42 \frac{\delta_2^*}{\theta_{11}} \frac{1}{Re_\theta} \quad (\text{B.21})$$

turbulent [16]

$$\begin{aligned}
 U_s &\equiv \frac{u_s}{q_e}, & \text{streamwise slip velocity} \\
 W_s &\equiv \frac{w_s}{q_e} = A_c(1.0 - U_s) & \text{crossflow slip velocity} \\
 C_f &= \frac{2}{\left(\frac{\pi}{0.18}\right)^2} \tanh^{-1}(Q_s^2) \\
 &= \frac{2}{\left(\frac{\pi}{0.18}\right)^2} \frac{1}{2} \log \left(\frac{1+Q_s^2}{1-Q_s^2} \right) \\
 C_{f1} &= C_f \frac{U_s}{Q_s} \implies U_s = \frac{C_{f1}}{C_f} Q_s \\
 C_{f2} &= C_f \frac{W_s}{Q_s}
 \end{aligned} \tag{B.22}$$

The streamwise slip velocity here is a different approximation than the one used elsewhere. The following nonlinear equation is solved for Q_s ,

$$\begin{aligned}
 Q_s^2 &= U_s^2 + W_s^2 \\
 &= U_s^2 + A_c^2 (1 - U_s)^2 \\
 &= (1 + A_c^2) U_s^2 - 2A_c^2 U_s + A_c^2 \\
 &= (1 + A_c^2) Q_s^2 \left(\frac{C_{f1}}{C_f} \right)^2 - 2A_c^2 Q_s \left(\frac{C_{f1}}{C_f} \right) + A_c^2
 \end{aligned} \tag{B.23}$$

Dissipation [16]

laminar wall layer

$$\begin{aligned}
 D_1 &= \frac{1}{Re_\theta} \left[0.207 + 0.00205 (4.0 - H_k)^{5.5} \right] & H_k < 4.0 \\
 D_1 &= \frac{1}{Re_\theta} \left[0.207 - 0.0016 \frac{(H_k - 4.0)^2}{1.0 + 0.02 (H_k - 4.0)^2} \right] & H_k \geq 4.0
 \end{aligned} \tag{B.24}$$

$$C_{Dw} = \frac{1}{2} H^* D_1 + 0.0455 \left(\frac{\delta_2^*}{\theta_{11}} \right)^2 \frac{1}{Re_\theta}$$

turbulent wall layer

$$C_{Dw} = \frac{1}{2} (C_{f1} U_s + C_{f2} W_s) \tag{B.25}$$

wake layer

$$\begin{aligned}
 \Delta C_D &= \int \tau_x \frac{\partial u}{\partial \eta} d\eta + \int \tau_z \frac{\partial w}{\partial \eta} d\eta \\
 &= \int \tau_x \frac{\partial u}{\partial \eta} d\eta + \int \tau_x \frac{\partial u}{\partial \eta} \left(\frac{\tau_z \frac{\partial w}{\partial \eta}}{\tau_x \frac{\partial u}{\partial \eta}} \right) d\eta \\
 &= \int \tau_x \frac{\partial u}{\partial \eta} d\eta + \int \tau_x \frac{\partial u}{\partial \eta} \left(\frac{\mu_t \frac{\partial w}{\partial \eta} \frac{\partial w}{\partial \eta}}{\mu_t \frac{\partial u}{\partial \eta} \frac{\partial u}{\partial \eta}} \right) d\eta \\
 &= \int \tau_x \frac{\partial u}{\partial \eta} d\eta + \int \tau_x \frac{\partial u}{\partial \eta} \left(\frac{\partial w}{\partial u} \right)^2 d\eta \\
 &= \left(\int \tau_x \frac{\partial u}{\partial \eta} d\eta \right) (1.0 + A_c^2) \\
 &= C_\tau (1.0 - U_s) (1.0 + A_c^2)
 \end{aligned} \tag{B.26}$$

The total dissipation coefficient is given by $C_D = C_{Dw} + \Delta C_D$

Appendix C

Wall Transpiration

This appendix contains the derivation for the wall transpiration flux (ρV_w) formula used in Chapter 4. It is an extension of the results for two-dimensional, incompressible flow from reference [33]. In addition, a useful expression for the wall transpiration's contribution to drag is derived here to be used in Appendix D.

First, define the boundary layer thickness *components*.

$$\rho_e q_e \delta_x^* \equiv \int_0^{y_e} (\rho_e u_e - \rho u) dy \quad (C.1)$$

$$\rho_e q_e \delta_z^* \equiv \int_0^{y_e} (\rho_e w_e - \rho w) dy \quad (C.2)$$

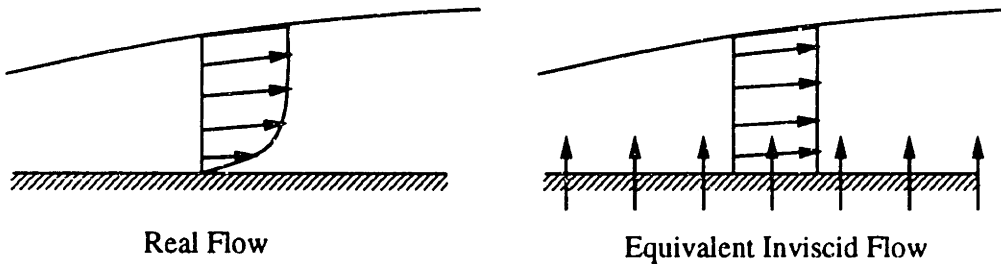


Figure C.1: Equivalent Inviscid Flow Calculation

The goal is simulate the displacement effect of the boundary layer in an inviscid flow. This is achieved by matching the normal velocity at a distance of a boundary layer's edge, y_e , for the case of a real viscous flow and an inviscid flow with wall transpiration.

C.1 Real Viscous Flow

$$\begin{aligned}
\rho_e V_e &= \int_0^{y_e} \frac{\partial}{\partial y} (\rho v) dy \\
&= \int_0^{y_e} - \left[\frac{\partial}{\partial x} (\rho u) + \frac{\partial}{\partial z} (\rho w) \right] dy \\
&= \int_0^{y_e} \frac{\partial}{\partial x} (\rho_e u_e - \rho u) + \frac{\partial}{\partial z} (\rho_e w_e - \rho w) dy \\
&\quad - y_e \left[\frac{\partial}{\partial x} (\rho_e u_e) + \frac{\partial}{\partial z} (\rho_e w_e) \right] \\
&= \frac{\partial}{\partial x} (\rho_e q_e \delta_x^*) + \frac{\partial}{\partial z} (\rho_e q_e \delta_z^*) - y_e \left[\frac{\partial}{\partial x} (\rho_e u_e) + \frac{\partial}{\partial z} (\rho_e w_e) \right]
\end{aligned} \tag{C.3}$$

C.2 Equivalent Inviscid Flow

$$\begin{aligned}
\rho_e V_e &= \rho V_w + \int_0^{y_e} \frac{\partial}{\partial y} (\rho v) dy \\
&= \rho V_w + \int_0^{y_e} - \left[\frac{\partial}{\partial x} (\rho u) + \frac{\partial}{\partial z} (\rho w) \right] dy \\
&= \rho V_w - y_e \left[\frac{\partial}{\partial x} (\rho_e u_e) + \frac{\partial}{\partial z} (\rho_e w_e) \right]
\end{aligned} \tag{C.4}$$

It is assumed that $\rho_e u_e$ and $\rho_e w_e$ are constant in an inviscid flow through the distance y_e in equation C.4—this is a first order boundary layer assumption. In order to match $\rho_e V_e$ for equations C.3 and C.4, the desired expression for ρV_w becomes:

$$\rho V_w = \frac{\partial}{\partial x} (\rho_e q_e \delta_x^*) + \frac{\partial}{\partial z} (\rho_e q_e \delta_z^*)$$

C.3 Wall Transpiration for Drag Calculations

In Appendix D, an expression for $(U \rho \vec{q} \cdot \hat{n})$ will be required for drag calculations. U is the Cartesian velocity component in the freestream direction. On the body and wake surfaces $(\rho \vec{q} \cdot \hat{n})$ would be the negative of the wall transpiration since \hat{n} points out of the fluid. Using a slightly different notation, the wall transpiration is expressed as:

$$\rho \vec{q} \cdot \hat{n}|_w = -\nabla_s \cdot (\rho_e q_e \vec{\delta}^*) \quad (C.5)$$

where

$$\nabla_s \equiv \frac{\partial}{\partial x} \hat{e}_x + \frac{\partial}{\partial z} \hat{e}_z$$

$$\vec{\delta}^* \equiv \delta_x^* \hat{e}_x + \delta_z^* \hat{e}_z$$

\hat{e}_x and \hat{e}_z are a 3-D unit vectors which define a local, 2-D coordinate system that lies in the plane locally tangent to the surface. The ∇_s operator is the gradient operator in this 2-D coordinate system.

C.3.1 3-D Integral Momentum Equations

The 3-D integral momentum equations are:

$$\begin{aligned} \nabla_s \cdot (\rho_e q_e^2 \vec{\theta}_x) + \rho_e q_e \vec{\delta}^* \cdot \nabla_s u_e &= \tau_{zw} \\ \nabla_s \cdot (\rho_e q_e^2 \vec{\theta}_z) + \rho_e q_e \vec{\delta}^* \cdot \nabla_s w_e &= \tau_{zw} \end{aligned} \quad (C.6)$$

where

$$\vec{\theta}_x = \theta_{xx} \hat{e}_x + \theta_{xz} \hat{e}_z$$

$$\vec{\theta}_z = \theta_{zx} \hat{e}_x + \theta_{zz} \hat{e}_z$$

C.3.2 Vector Product Rule and Combining

As an intermediate step, the product rule with the ∇_s operator produces the following expressions:

$$\nabla_s \cdot (\rho_e q_e \vec{\delta}^* u_e) = u_e \nabla_s \cdot (\rho_e q_e \vec{\delta}^*) + \rho_e q_e \vec{\delta}^* \cdot \nabla_s u_e$$

$$\nabla_s \cdot (\rho_e q_e \vec{\delta}^* w_e) = w_e \nabla_s \cdot (\rho_e q_e \vec{\delta}^*) + \rho_e q_e \vec{\delta}^* \cdot \nabla_s w_e$$

Combining these expressions with equation C.6 one arrives at:

$$\begin{aligned} -u_e \nabla_s \cdot (\rho_e q_e \vec{\delta}^*) &= -\nabla_s \cdot (\rho_e q_e^2 \vec{\theta}_x) + \tau_{zw} - \nabla_s \cdot (\rho_e q_e u_e \vec{\delta}^*) \\ -w_e \nabla_s \cdot (\rho_e q_e \vec{\delta}^*) &= -\nabla_s \cdot (\rho_e q_e^2 \vec{\theta}_z) + \tau_{zw} - \nabla_s \cdot (\rho_e q_e w_e \vec{\delta}^*) \end{aligned} \quad (C.7)$$

Since $U = \vec{q}_e \cdot \hat{i} = u_e (\hat{e}_x \cdot \hat{i}) + w_e (\hat{e}_z \cdot \hat{i})$, and using equations C.5 and C.7 :

$$\begin{aligned} U (\rho_e \vec{q} \cdot \hat{n}) &= [u_e (\hat{e}_x \cdot \hat{i}) + w_e (\hat{e}_z \cdot \hat{i})] \left[-\nabla_s \cdot (\rho_e q_e \vec{\delta}^*) \right] \\ &= [\tau_{zw} - \nabla_s \cdot (\rho_e q_e u_e \vec{\delta}^*) - \nabla_s \cdot (\rho_e q_e^2 \vec{\theta}_x)] (\hat{e}_x \cdot \hat{i}) \\ &\quad + [\tau_{zw} - \nabla_s \cdot (\rho_e q_e w_e \vec{\delta}^*) - \nabla_s \cdot (\rho_e q_e^2 \vec{\theta}_z)] (\hat{e}_z \cdot \hat{i}) \end{aligned} \quad (C.8)$$

C.3.3 Differencing Coordinate Vectors

Another application of the product rule yields

$$\begin{aligned}
\nabla_s \cdot [(\hat{e}_x \cdot \hat{i}) \rho_e q_e u_e \vec{\delta}^*] &= (\hat{e}_x \cdot \hat{i}) \nabla_s \cdot (\rho_e q_e u_e \vec{\delta}^*) + \rho_e q_e u_e \vec{\delta}^* \cdot \nabla_s (\hat{e}_x \cdot \hat{i}) \\
\nabla_s \cdot [(\hat{e}_z \cdot \hat{i}) \rho_e q_e w_e \vec{\delta}^*] &= (\hat{e}_z \cdot \hat{i}) \nabla_s \cdot (\rho_e q_e w_e \vec{\delta}^*) + \rho_e q_e w_e \vec{\delta}^* \cdot \nabla_s (\hat{e}_z \cdot \hat{i}) \\
\nabla_s \cdot [(\hat{e}_x \cdot \hat{i}) \rho_e q_e^2 \vec{\theta}_x] &= (\hat{e}_x \cdot \hat{i}) \nabla_s \cdot (\rho_e q_e^2 \vec{\theta}_x) + \rho_e q_e^2 \vec{\theta}_x \cdot \nabla_s (\hat{e}_x \cdot \hat{i}) \\
\nabla_s \cdot [(\hat{e}_z \cdot \hat{i}) \rho_e q_e^2 \vec{\theta}_z] &= (\hat{e}_z \cdot \hat{i}) \nabla_s \cdot (\rho_e q_e^2 \vec{\theta}_z) + \rho_e q_e^2 \vec{\theta}_z \cdot \nabla_s (\hat{e}_z \cdot \hat{i})
\end{aligned} \tag{C.9}$$

The third term on each of the relations in equation C.9 may be collected and rewritten as:

$$\hat{i} \cdot \left\{ \left[(\rho_e q_e u_e \vec{\delta}^* + \rho_e q_e^2 \vec{\theta}_x) \cdot \nabla_s \right] \hat{e}_x + \left[(\rho_e q_e w_e \vec{\delta}^* + \rho_e q_e^2 \vec{\theta}_z) \cdot \nabla_s \right] \hat{e}_z \right\}$$

In the discrete case, \hat{e}_x and \hat{e}_z are constant over each panel. Hence the above term is zero, and equation C.8 becomes:

$$\begin{aligned}
U (\rho \vec{q} \cdot \hat{n})|_w &= \tau_{zw} (\hat{e}_x \cdot \hat{i}) + \tau_{zw} (\hat{e}_z \cdot \hat{i}) \\
&- \nabla_s \cdot [(\hat{e}_x \cdot \hat{i}) \rho_e q_e u_e \vec{\delta}^*] - \nabla_s \cdot [(\hat{e}_z \cdot \hat{i}) \rho_e q_e w_e \vec{\delta}^*] \\
&- \nabla_s \cdot [(\hat{e}_x \cdot \hat{i}) \rho_e q_e^2 \vec{\theta}_x] - \nabla_s \cdot [(\hat{e}_z \cdot \hat{i}) \rho_e q_e^2 \vec{\theta}_z]
\end{aligned} \tag{C.10}$$

Appendix D

Drag Calculation

This appendix contains the derivation of a drag formula for a 3-D Full Potential and boundary layer simulation. The most direct method of computing drag is by the integration of shear stress and pressure over the body surface. However, this method is prone to numerical error as shown by Smith and Kroo [50]. Drag for aerodynamic shapes is typically a small quantity and subtracting nearly equal pressures from the front and rear of the body is inaccurate.

An alternative to surface integration is to compute drag using only farfield quantities and body force-like terms. The goal is to sum small positive quantities which leads to a more accurate drag calculation. In addition, the farfield drag formula may be separated into vortex, wave, and viscous drag components, which is of much use to the aircraft designer.

There are two ways to approach the farfield calculation, and both use the integral momentum theorem. The first is to assume a real viscous flow (RVF) and include viscous terms in the integral momentum theorem. The difficulty with using the RVF is in the computation of vortex drag. Vortex drag is derived with a Trefftz plane analysis which assumes that at a farfield plane there is no streamwise velocity perturbation along the vortex sheet and the flow is irrotational [4]. These assumptions are violated because of the velocity defect in the viscous wake (see Fig. D.1), and therefore, the viscous wake region must be neglected.

Another farfield approach is to use the *inviscid* integral momentum theorem and to model the problem as an equivalent inviscid flow (EIF) with the wall transpiration BC. The benefit of this approach is that the vortex drag may be computed without neglecting the farfield wake region since there is no velocity defect at the Trefftz plane (Fig. D.1). The drag component corresponding to the viscous drag appears through the wall transpiration:

a mass source in an inviscid flow will experience drag, the source strength is related to the calculated displacement thickness (δ^*), and the displacement thickness is related to the momentum thickness (θ) via the boundary layer equations. This derivation is slightly involved, but (as will be shown) it is feasible and the wake need not be neglected. Hence the EIF model will be used to derive the farfield drag formula.

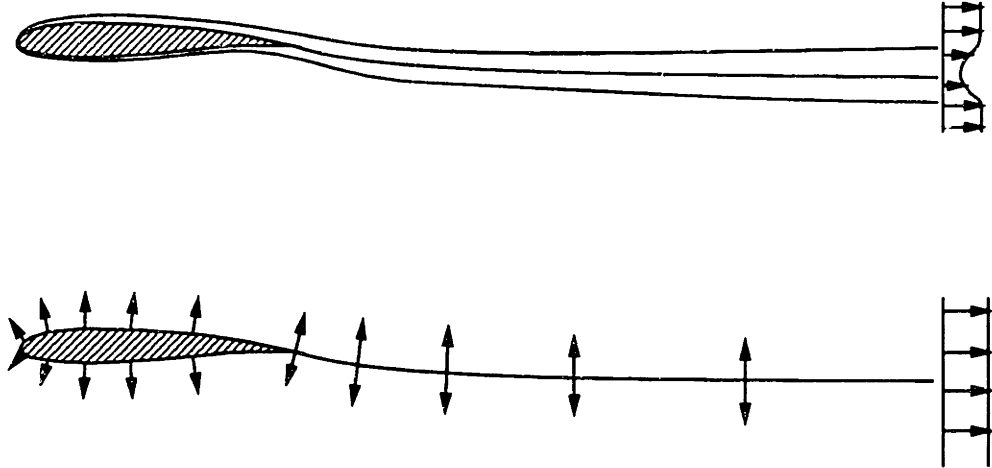


Figure D.1: Velocity Defect in RVF vs. EIF

It is first necessary to address whether the drag from the inviscid integral momentum theorem (using EIF) matches that of the viscous integral momentum theorem. If the surface pressure distribution in the inviscid integral is the same as that in the viscous integral, then the pressure drag will be equal. And indeed, the surface pressure distribution from an EIF matches that of the RVF within the order of the BL theory that is used. Furthermore, because an inviscid flow has no shear stress, the shear stress distribution from the boundary layer calculation needs to be added to the EIF drag. Hence the drag estimate from the inviscid integral momentum theorem (using EIF) will match that from the viscous integral momentum theorem: the drag being defined as

$$D \equiv \iint_{\partial\Omega_w} \tau_{zw} (\hat{e}_x \cdot \hat{i}) + \tau_{zw} (\hat{e}_z \cdot \hat{i}) dS + \iint_{\partial\Omega_w} p \hat{n} \cdot \hat{i} dS$$

D.1 Preliminaries

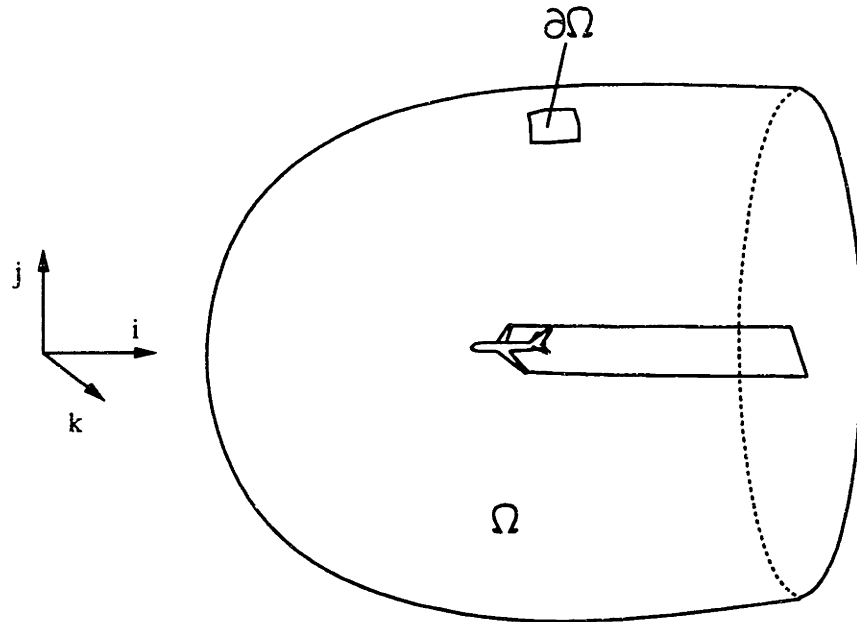


Figure D.2: Control Volume for Integral Momentum Theorem

First, an eclectic set of preliminary relations are derived which will be used later in the integral momentum theorem (§D.2). The coordinate system for this analysis is aligned such that the x -direction is the direction of freestream flow and drag forces.

D.1.1 Small Perturbation Pressure and Density

$$u = u_{\infty} + u', \quad v = v', \quad w = w', \quad q_{\infty} = u_{\infty}$$

$$q^2 = u_{\infty}^2 + 2u_{\infty}u' + (u'^2 + v'^2 + w'^2) \quad (\text{D.1})$$

Using the above perturbation velocities, and with $\frac{\gamma-1}{2}M_{\infty}^2 \left(1 - \frac{q^2}{q_{\infty}^2} \right) \ll 1$ the pressure may be approximated using the binomial expansion:

$$\begin{aligned}
p &= p_\infty \left[1 + \frac{\gamma - 1}{2} M_\infty^2 \left(1 - \frac{q^2}{q_\infty^2} \right) \right]^{\frac{\gamma}{\gamma-1}} \\
&\approx p_\infty \left[1 + \frac{\gamma}{\gamma-1} \frac{\gamma-1}{2} M_\infty^2 \left(1 - \frac{q^2}{q_\infty^2} \right) \right] \quad (\text{D.2}) \\
&\approx p_\infty - \frac{1}{2} \rho_\infty \left[2u_\infty u' + (u'^2 + v'^2 + w'^2) \right]
\end{aligned}$$

Similarly, the density is given by:

$$\begin{aligned}
\rho &= \rho_\infty \left[1 + \frac{\gamma - 1}{2} M_\infty^2 \left(1 - \frac{q^2}{q_\infty^2} \right) \right]^{\frac{1}{\gamma-1}} \\
&\approx \rho_\infty \left[1 + \frac{1}{\gamma-1} \frac{\gamma-1}{2} M_\infty^2 \left(1 - \frac{q^2}{q_\infty^2} \right) \right] \quad (\text{D.3}) \\
&\approx \rho_\infty - \frac{1}{2} \frac{\rho_\infty}{a_\infty^2} \left[2u_\infty u' + (u'^2 + v'^2 + w'^2) \right]
\end{aligned}$$

D.1.2 ∇_s Operator

Although not proven here, the surface gradient operator of Appendix C obeys a Divergence Theorem.

$$\iint_{\partial\Omega} \nabla_s \cdot \vec{F} dS = \oint \vec{F} \cdot \hat{n} dl \quad (\text{D.4})$$

Typically, the boundary layer quantities represented by \vec{F} (e.g. $\rho_e q_e \vec{\delta}^*$) disappear everywhere along the line integral path except along the span line in the exit plane.

D.1.3 Continuity Result

The continuity equation, assuming that all inter-volume mass sources sum to zero, becomes:

$$\iint_{\partial\Omega} \rho \vec{q} \cdot \hat{n} dS = 0 \quad (\text{D.5})$$

After splitting this into integrals over the farfield surface, $\partial\Omega_{ff}$, and over the wing/wake, $\partial\Omega_w$, the following relation is derived:

$$\begin{aligned} \iint_{\partial\Omega} \rho \vec{q} \cdot \hat{n} dS &= \iint_{\partial\Omega_w} \rho \vec{q} \cdot \hat{n} dS \\ &+ \iint_{\partial\Omega_{ff}} \rho_\infty [(u_\infty + u') \hat{i} \cdot \hat{n} + v' \hat{j} \cdot \hat{n} + w' \hat{k} \cdot \hat{n}] dS \\ &= - \iint_{\partial\Omega_w} \nabla_s \cdot \rho_e q_e \vec{\delta}^* dS \\ &+ \iint_{\partial\Omega_{ff}} \rho_\infty (u' \hat{i} \cdot \hat{n} + v' \hat{j} \cdot \hat{n} + w' \hat{k} \cdot \hat{n}) dS \\ &= - \oint_{\partial\Omega_w} \rho_e q_e \vec{\delta}^* \cdot \hat{n} dl + \iint_{\partial\Omega_{ff}} \rho_\infty (u' \hat{i} \cdot \hat{n} + v' \hat{j} \cdot \hat{n} + w' \hat{k} \cdot \hat{n}) dS \end{aligned}$$

The $\rho_\infty u_\infty$ constant integrated over a closed boundary is zero. The mass transpiration on wing and wake surfaces is defined by equation C.5 and manipulated by relation D.4. The final, useful relation is given by:

$$\iint_{\partial\Omega_{ff}} \rho_\infty (u' \hat{i} \cdot \hat{n} + v' \hat{j} \cdot \hat{n} + w' \hat{k} \cdot \hat{n}) dS = \int_{b_\infty} \rho_e q_e \vec{\delta}^* \cdot \hat{n} dl \quad (\text{D.6})$$

The $\rho_e q_e \vec{\delta}^*$ term at the attachment line contributes nothing because the upper and lower surface line integrations cancel. This term is zero on the wingtip side boundaries because the boundary layer ends in space and $\vec{\delta}^*$ is zero there. The only place it is not zero is at the along the exit span line (b_∞).

D.2 Integral Momentum Theorem

Now the drag is computed from the integral momentum theorem. The steady flow, inviscid integral momentum theorem is given by:

$$\iint_{\partial\Omega} \rho \vec{q}(\vec{q} \cdot \hat{n}) dS = - \iint_{\partial\Omega} (p - p_\infty) \hat{n} dS + \iiint_{\Omega} \vec{g} dV \quad (\text{D.7})$$

p_∞ integrated over a closed surface adds zero to the equation, but this form of the pressure integral will be useful. \vec{g} is a body force term. The only restriction is that we chose our outflow control surface to be normal to the wake some distance away from the body (see figure D.2). Now the momentum flux and pressure terms may be divided into those on the farfield surfaces and those on the solid surfaces.

D.3 Farfield Fluxes and Pressure

The farfield flux and pressure integrals in equation D.7 may be computed using small perturbation velocities. Away from the outflow-plane vortex sheet, all of the velocity perturbations are small, so that equations may be linearized. Near the sheet, u' is small, but v' and w' are not. If the exit plane is positioned normal to the x -axis, the x -component of the farfield flux term is given by:

$$\begin{aligned} \iint_{\partial\Omega_{ff}} \rho u (\vec{q} \cdot \hat{n}) dS &= \iint_{\partial\Omega_{ff}} \rho_\infty (u_\infty + u') [(u_\infty + u') \hat{i} \cdot \hat{n} + v' \hat{j} \cdot \hat{n} + w' \hat{k} \cdot \hat{n}] dS \\ &= \iint_{\partial\Omega_{ff}} \rho_\infty [(u_\infty^2 + 2u_\infty u') \hat{i} \cdot \hat{n} + u_\infty v' \hat{j} \cdot \hat{n} + u_\infty w' \hat{k} \cdot \hat{n}] dS \\ &= \iint_{\partial\Omega_{ff}} \rho_\infty u_\infty u' \hat{i} \cdot \hat{n} dS \\ &\quad + \iint_{\partial\Omega_{ff}} \rho_\infty [u_\infty u' \hat{i} \cdot \hat{n} + u_\infty v' \hat{j} \cdot \hat{n} + u_\infty w' \hat{k} \cdot \hat{n}] dS \\ &= \iint_{\partial\Omega_{ff}} \rho_\infty u_\infty u' \hat{i} \cdot \hat{n} dS + \int_{b_\infty} u_\infty \rho_e q_e \vec{\delta}^* \cdot \hat{n} dl \end{aligned} \quad (\text{D.8})$$

u'^2 terms are neglected in favor of other terms. $u'v'$ and $u'w'$ are not necessarily small at the exit plane, but $\hat{j} \cdot \hat{n}$ and $\hat{k} \cdot \hat{n}$ are zero there since we selected the exit plane such that $\hat{n} = \hat{i}$. Also equation D.6 has been used to replace the last group of flux terms. Now, the farfield pressure term is given by:

$$\begin{aligned} - \iint_{\partial\Omega_{ff}} (p - p_\infty) \hat{n} \cdot \hat{i} \, dS &= \iint_{\partial\Omega_{ff}} \frac{1}{2} \rho_\infty [2u_\infty u' + (u'^2 + v'^2 + w'^2)] \hat{i} \cdot \hat{n} \, dS \\ &= \iint_{\partial\Omega_{ff}} \rho_\infty u_\infty u' \hat{n} \cdot \hat{i} \, dS \\ &\quad + \frac{1}{2} \iint_{\partial\Omega_{exit}} \rho_\infty (v'^2 + w'^2) \, dS \end{aligned} \quad (\text{D.9})$$

Again, u'^2 terms have been neglected.

D.4 Surface Fluxes and Pressure

Using the integral momentum BL equations in the form of equation C.10, the wall momentum flux becomes:

$$\begin{aligned} \iint_{\partial\Omega_w} u (\rho \vec{q} \cdot \hat{n}) \, dS &= \iint_{\partial\Omega_w} \tau_{zw} (\hat{e}_x \cdot \hat{i}) + \tau_{zw} (\hat{e}_z \cdot \hat{i}) \, dS \\ &\quad - \int_{b_\infty} [(\hat{e}_x \cdot \hat{i}) \rho_e q_e u_e \vec{\delta}^* + (\hat{e}_z \cdot \hat{i}) \rho_e q_e w_e \vec{\delta}^*] \cdot \hat{n} \, dl \\ &\quad - \int_{b_\infty} [(\hat{e}_x \cdot \hat{i}) \rho_e q_e^2 \vec{\theta}_x + (\hat{e}_z \cdot \hat{i}) \rho_e q_e^2 \vec{\theta}_z] \cdot \hat{n} \, dl \end{aligned} \quad (\text{D.10})$$

where $\partial\Omega_w$ is over solid surfaces. The middle term on the right-hand-side becomes

$$- \int_{b_\infty} [(\hat{e}_x \cdot \hat{i}) \rho_e q_e u_e \vec{\delta}^* + (\hat{e}_z \cdot \hat{i}) \rho_e q_e w_e \vec{\delta}^*] \cdot \hat{n} \, dl = - \int_{b_\infty} u (\rho_e q_e \vec{\delta}^*) \cdot \hat{n} \, dl \quad (\text{D.11})$$

since $u = u_e (\hat{e}_x \cdot \hat{i}) + w_e (\hat{e}_z \cdot \hat{i})$. The surface pressure integral is simply

$$-\iint_{\partial\Omega_w} (p - p_\infty) \hat{n} \cdot \hat{i} dS = -\iint_{\partial\Omega_w} p \hat{n} \cdot \hat{i} dS \quad (\text{D.12})$$

D.5 Interior Momentum Sources

The artificial viscosity terms may be viewed as producing momentum sources [58]. The equation that is being solved is the continuity equation with a modified density, $\tilde{\rho} = \rho + \delta\rho$. Hence the actual Full Potential equation is:

$$\nabla \cdot [(\rho + \delta\rho) \vec{q}] = 0$$

or $\nabla \cdot (\rho \vec{q}) = -\nabla \cdot (\delta\rho \vec{q})$ (D.13)

Now, using a vector identity,

$$\nabla \cdot (\rho u \vec{q}) - \rho (\vec{q} \cdot \nabla) u = u \nabla \cdot (\rho \vec{q})$$

and combining this with Euler's equation in the x -direction,

$$\begin{aligned} \rho (\vec{q} \cdot \nabla) u &= -\frac{\partial p}{\partial x} \\ &= -\nabla p \cdot \hat{i} \end{aligned}$$

we arrive at:

$$\nabla \cdot (\rho u \vec{q}) = -\nabla \cdot (p \hat{i}) + u \nabla \cdot (\rho \vec{q}) \quad (\text{D.14})$$

Finally, taking the integral of D.14, combining with equation D.13, and employing the Divergence Theorem, we have:

$$\iint_{\partial\Omega} u (\rho \vec{q} \cdot \hat{n}) dS = -\iint_{\partial\Omega} p \hat{n} \cdot \hat{i} dS + \iiint_{\Omega} -u \nabla \cdot (\delta\rho \vec{q}) dV \quad (\text{D.15})$$

This is the steady, inviscid, integral momentum equation with artificial viscosity induced momentum sources, therefore

$$\iiint_{\Omega} \vec{g} \, dV = \iiint_{\Omega} -u \nabla \cdot (\delta \rho \vec{q}) \, dV \quad (D.16)$$

In the case of a wing with shocks, a surface pressure integration will indicate wave drag. However, a momentum integral evaluation in the farfield would yield *no* wave drag because the Full Potential equation is isentropic [67]. In this case, the surface pressure integral and momentum source integrals cancel in equation D.15 to yield no momentum loss in a farfield integration ($\iint_{\partial\Omega_{ff}} \rho u (\vec{q} \cdot \hat{n}) \, dS = 0$).

D.6 Total Drag

Starting with the integral momentum theorem (Eqn. D.7), the farfield and body surface contributions (D.8, D.11, D.9, D.12) and the interior momentum sources (D.16) are expressed as:

$$\begin{aligned} & \iint_{\partial\Omega_w} \tau_{zw} (\hat{e}_z \cdot \hat{i}) + \tau_{zw} (\hat{e}_z \cdot \hat{i}) \, dS - \int_{b_\infty} \left[(\hat{e}_z \cdot \hat{i}) \rho_e q_e^2 \vec{\theta}_z + (\hat{e}_z \cdot \hat{i}) \rho_e q_e^2 \vec{\theta}_z \right] \, dl \\ & + \iint_{\partial\Omega_{ff}} \rho_\infty u_\infty u' \hat{i} \cdot \hat{n} \, dS = - \iint_{\partial\Omega_w} p \hat{n} \cdot \hat{i} \, dS \\ & + \iint_{\partial\Omega_{ff}} \rho_\infty u_\infty u' \hat{n} \cdot \hat{i} \, dS + \frac{1}{2} \iint_{\partial\Omega_{exit}} \rho_\infty (v'^2 + w'^2) \, dS - \iiint_{\Omega} u \nabla \cdot (\delta \rho \vec{q}) \, dV \end{aligned} \quad (D.17)$$

Two of the terms cancel, and the term containing kinetic energy at the exit plane ($v'^2 + w'^2$) becomes:

$$\begin{aligned} \frac{1}{2} \iint_{\partial\Omega_{exit}} \rho_\infty (v'^2 + w'^2) \, dS &= \frac{1}{2} \rho_\infty \iint_{\partial\Omega_{exit}} (\nabla \phi \cdot \nabla \phi) \, dS \\ &= \frac{1}{2} \rho_\infty \iint_{\partial\Omega_{exit}} \{ \nabla \cdot (\phi \nabla \phi) - \nabla^2 \phi \} \, dS \\ &= \frac{1}{2} \rho_\infty \int_{b_\infty} (\phi_{upper} - \phi_{lower}) \frac{\partial \phi}{\partial n} \, dl = \frac{1}{2} \int_{b_\infty} \Delta \phi \frac{\partial \phi}{\partial n} \, dl \end{aligned}$$

where the 2-D Divergence theorem and the continuity equation ($\nabla^2 \phi = 0$) have been used.

Two of the terms in Eqn. D 17 constitute the definition of drag, hence:

$$\begin{aligned}
D &= \iint_{\partial\Omega_w} \tau_{zw} (\hat{e}_x \cdot i) + \tau_{zw} (\hat{e}_z \cdot i) dS + \iint_{\partial\Omega_w} p \hat{n} \cdot i dS \\
&= \frac{1}{2} \rho_\infty \int_{b_\infty} \Delta \phi \frac{\partial \phi}{\partial n} dl \\
&\quad + \int_{b_\infty} \left[(\hat{e}_x \cdot i) \rho_e q_e^2 \vec{\theta}_x + (\hat{e}_z \cdot i) \rho_e q_e^2 \vec{\theta}_z \right] dl \\
&\quad - \iiint_{\Omega} u \nabla \cdot (\delta \rho \vec{q}) dV
\end{aligned} \tag{D.18}$$

The $\Delta \phi \frac{\partial \phi}{\partial n}$ term is due to kinetic energy losses associated with vortex drag, the $\vec{\theta}_x$ and $\vec{\theta}_z$ terms represent the viscous momentum defect, and the body force term represents the wave drag. The induced and viscous drag components are summations of small positive terms. And the wave drag is the sum of positive and negative terms that are *not* nearly equal. So it is expected that the drag calculation based on this formula will be less prone to numerical noise.